

**DAHLGREN DIVISION  
NAVAL SURFACE WARFARE CENTER**

Dahlgren, Virginia 22448-5100

---



**NSWCDD/TR-95/222**

**AN EXPERIMENTAL INVESTIGATION OF  
ORGANIZED TURBULENT MOTIONS AND  
WALL-PRESSURE FLUCTUATIONS  
IN COMPLEX FLOWS**

**MARK KAMMEYER**

**STRATEGIC AND SPACE SYSTEMS DEPARTMENT**

**DECEMBER 1995**

Approved for public release; distribution is unlimited.

**19960430 096**

**DTIC QUALITY INSPECTED 1**

REPORT DOCUMENTATION PAGE			Form Approved OBM No. 0704-0188	
Public reporting burden for this collection of information is estimated to average 1 hour per response, including the time for reviewing instructions, search existing data sources, gathering and maintaining the data needed, and completing and reviewing the collection of information. Send comments regarding this burden or any other aspect of this collection of information, including suggestions for reducing this burden, to Washington Headquarters Services, Directorate for Information Operations and Reports, 1215 Jefferson Davis Highway, Suite 1204, Arlington, VA 22202-4302, and to the Office of Management and Budget, Paperwork Reduction Project (0704-0188), Washington, DC 20503.				
1. AGENCY USE ONLY (Leave blank)		2. REPORT DATE December 1995		3. REPORT TYPE AND DATES COVERED
4. TITLE AND SUBTITLE An Experimental Investigation of Organized Turbulent Motions and Wall-Pressure Fluctuations in Complex Flows			5. FUNDING NUMBERS	
6. AUTHOR(s) Mark Kammeyer				
7. PERFORMING ORGANIZATION NAME(S) AND ADDRESS(ES) Commander Naval Surface Warfare Center, Dahlgren Division (Code K24) 17320 Dahlgren Road Dahlgren, VA 22448-5100			8. PERFORMING ORGANIZATION REPORT NUMBER NSWCDD/TR-95/222	
9. SPONSORING/MONITORING AGENCY NAME(S) AND ADDRESS(ES)			10. SPONSORING/MONITORING AGENCY REPORT NUMBER	
11. SUPPLEMENTARY NOTES				
12a. DISTRIBUTION/AVAILABILITY STATEMENT Authorized for public release; distribution is unlimited.			12b. DISTRIBUTION CODE	
13. ABSTRACT (Maximum 200 words) <p>The relationship between high-amplitude wall-pressure peaks and near-wall flow structures has been studied for both equilibrium and disturbed turbulent boundary layers. The disturbed flow was that formed downstream of reattachment of the flow over an aft-facing step. In this case, the disturbances were primarily confined to the outer regions of the boundary layer. Simultaneous measurements of the fluctuating wall-pressure and the streamwise and wall-normal velocity were obtained. These measurements were acquired at numerous locations across the boundary layers. A filtering technique based on the wavelet transform was developed to isolate the near-wall motions from the outer-layer disturbances. Correlation and conditional sampling were performed based on the detection of cluster patterns of wall-pressure and turbulence-producing flow events. The results confirm that patterns of large-amplitude wall-pressure events are footprints of the active (turbulence-producing) motions. The results of flowfield mappings show two vortices, one ahead and above the other, that induce the ejection/sweep pattern and concomitant wall-pressure peak aligned to the log-law region. The same generic features were observed for both the equilibrium and disturbed flows, leading to the conclusion that the near-wall motions are weakly coupled to the outer-layer dynamics. The picture is consistent with models proposed by several investigators.</p>				
14. SUBJECT TERMS wavelets, wavelet transforms			15. NUMBER OF PAGES 140	
			16. PRICE CODE	
17. SECURITY CLASSIFICATION OF REPORT UNCLASSIFIED	18. SECURITY CLASSIFICATION OF THIS PAGE UNCLASSIFIED	19. SECURITY CLASSIFICATION OF ABSTRACT UNCLASSIFIED	20. LIMITATION OF ABSTRACT SAR	

## Foreword

This report was prepared as a dissertation for the degree Doctor of Philosophy in Mechanical Engineering, completed in November 1995 at The Catholic University of America. The author was supported by the Academic Fellowship Program of the Naval Surface Warfare Center, Dahlgren Division. Additional funding was provided by the Office of Naval Research under grant number N00014-94-1-0011, Dr. L. Patrick Purtell, scientific officer. In addition, Dr. Ted Farabee and Mr. Steven Russell of the Naval Surface Warfare Center, Carderock Division, provided the microphone systems for the wall-pressure measurements.

Approved by:



D. B. Colby, Head  
Strategic and Space Systems Department

## Contents

<b>1</b>	<b>Introduction</b>	<b>1</b>
1.1	Motivation . . . . .	1
1.2	Background . . . . .	2
1.2.1	Physical features of turbulent boundary layers . . . . .	2
1.2.2	Wall-pressure fluctuations . . . . .	6
1.2.3	Conditional sampling . . . . .	8
1.3	Research objectives and experimental approach . . . . .	9
1.3.1	Equilibrium turbulent boundary layer . . . . .	10
1.3.2	Disturbed turbulent boundary layer . . . . .	11
1.4	Outline of dissertation . . . . .	12
	References . . . . .	12
<b>2</b>	<b>Experimental setup and methods</b>	<b>16</b>
2.1	Introduction . . . . .	16
2.2	Facility . . . . .	16
2.3	Facility instrumentation . . . . .	17
2.4	Wall pressure sensors . . . . .	18
2.4.1	Microphone calibration . . . . .	18
2.4.2	Microphone resolution . . . . .	20
2.5	Hot-wire anemometers . . . . .	20
2.5.1	Hot-wire calibration . . . . .	21
2.5.2	Hot-wire resolution . . . . .	24
2.5.3	Probe displacement measurements . . . . .	24
2.6	Data acquisition and processing systems . . . . .	25
2.6.1	Digital data system . . . . .	25
2.6.2	Spectral data system . . . . .	26
2.7	Test conduct and data processing . . . . .	26
2.7.1	Test conduct . . . . .	27
2.7.2	Data reduction and filtering . . . . .	29
	References . . . . .	29



<b>3</b>	<b>Properties of equilibrium and disturbed flows</b>	<b>31</b>
3.1	Introduction . . . . .	31
3.2	Mean features . . . . .	31
3.3	Single-point statistics and spectra . . . . .	34
3.3.1	Velocity statistics . . . . .	36
3.3.2	Velocity power spectra . . . . .	40
3.3.3	Wall-pressure statistics . . . . .	44
3.3.4	Wall-pressure power spectra . . . . .	48
3.4	Peak-event detection . . . . .	49
3.4.1	Wall-pressure peak events . . . . .	51
3.4.2	Reynolds stress peak events . . . . .	54
3.5	Discussion . . . . .	57
	References . . . . .	63
<b>4</b>	<b>Application of wavelet filtering</b>	<b>66</b>
4.1	Introduction . . . . .	66
4.2	Wavelet transforms . . . . .	67
4.3	Scale-frequency relations and wavelet power . . . . .	70
4.4	Wavelet filtering . . . . .	71
4.4.1	Conventional wavelet filtering . . . . .	73
4.4.2	Weighted wavelet filtering . . . . .	75
4.5	Comparison of results . . . . .	77
4.5.1	Peak and quadrant event detection . . . . .	78
4.5.2	Conditional sampling . . . . .	82
4.6	Summary . . . . .	89
	References . . . . .	90
<b>5</b>	<b>Detection of event cluster patterns</b>	<b>92</b>
5.1	Introduction . . . . .	92
5.2	Detection techniques . . . . .	93
5.2.1	Localized variance technique . . . . .	93
5.2.2	Localized windowed peak-detection technique . . . . .	94
5.3	Correlation of clusters . . . . .	98
5.3.1	Estimation of convection velocity . . . . .	99
5.3.2	Correlations between turbulence and wall pressure . . . . .	101
5.4	Conditional sampling on event clusters . . . . .	102
5.4.1	Quadrant cluster detection . . . . .	103
5.4.2	Peak wall-pressure cluster detection . . . . .	104
5.5	Summary . . . . .	105
	References . . . . .	108

<b>6 Interpretations and conclusions</b>	<b>109</b>
6.1 Physical features of near-wall flow structures . . . . .	109
6.2 Effects of outer-layer disturbances . . . . .	113
6.3 Accomplishments . . . . .	116
6.4 Future work . . . . .	117
References . . . . .	118

## **Appendixes**

**A Hot-wire and wall-pressure surveys**

**B Measurement uncertainty**

**C Localized windowed peak detection algorithm**

**Distribution**

## Illustrations

1.1	Large-scale structure associated with the burst-sweep cycle. . . . .	5
1.2	Vortical structures and ejection/sweep motions in the turbulent boundary layer. . . . .	5
1.3	Schematic of near-wall turbulent motion and associated wall pressure. . . . .	7
1.4	Features of the flow over a backward-facing step. . . . .	11
2.1	The Catholic University Low Noise Flow Facility. . . . .	17
2.2	Schematic of instrumentation and data acquisition systems. . . . .	19
2.3	Sample hot wire calibration. . . . .	22
2.4	Sample X-wire U-velocity calibration. . . . .	22
2.5	Sample X-wire V-velocity calibration. . . . .	23
2.6	Pressure measurement locations relative to the aft-facing step. . . . .	28
3.1	Mean streamwise velocity profiles from single wire surveys. . . . .	33
3.2	Mean streamwise velocity profiles normalized by wall variables. . . . .	33
3.3	Mean wall-normal velocity profiles. . . . .	34
3.4	Streamwise turbulence intensity profiles. . . . .	36
3.5	Wall-normal turbulence intensity profiles. . . . .	37
3.6	Profiles of the skewness factor of the streamwise velocity fluctuations. . . . .	37
3.7	Profiles of the skewness factor of the wall-normal velocity fluctuations. . . . .	38
3.8	Profiles of the kurtosis factor of the streamwise velocity fluctuations. . . . .	39
3.9	Profiles of the kurtosis factor of the wall-normal velocity fluctuations. . . . .	39
3.10	Reynolds stress profiles. . . . .	40
3.11	Profiles of turbulence stress correlation coefficient. . . . .	41
3.12	Streamwise velocity spectra inside of the location of peak equilibrium $u_{rms}$ . . . . .	41
3.13	Streamwise velocity spectra outside of the location of peak equilibrium $u_{rms}$ . . . . .	42
3.14	Selected wall-normal velocity spectra inside of the location of peak disturbed $v_{rms}$ . . . . .	43
3.15	Selected wall-normal velocity spectra outside of the location of peak disturbed $v_{rms}$ . . . . .	44
3.16	Effect of the hot wire traverse assembly on the equilibrium flow wall pressure. . . . .	46

3.17	Effect of the hot wire traverse assembly on the disturbed flow wall pressure. . . . .	47
3.18	Equilibrium and disturbed TBL wall pressure spectra. . . . .	48
3.19	Sample time record of the equilibrium flow fluctuating wall pressure. .	50
3.20	Consecutive positive wall-pressure peak events for threshold $\kappa = 2$ . . .	51
3.21	Average positive wall-pressure peak-event shapes, $\kappa = 2$ . . . . .	53
3.22	Average negative wall-pressure peak-event shapes, $\kappa = 2$ . . . . .	54
3.23	Distribution of the time between equilibrium-flow positive wall-pressure peak events, $\kappa = 1$ . . . . .	55
3.24	Distribution of the time between disturbed-flow positive wall-pressure peak events, $\kappa = 1$ . . . . .	56
3.25	Average $uv$ peak-event shapes at $y/\delta = 0.02$ , $\kappa = -2$ . . . . .	58
3.26	Average $uv$ peak-event shapes at $y/\delta = 0.08$ , $\kappa = -2$ . . . . .	58
3.27	Average $uv$ peak-event shapes at $y/\delta = 0.25$ , $\kappa = -2$ . . . . .	59
3.28	Average $uv$ peak-event shapes at $y/\delta = 0.65$ , $\kappa = -2$ . . . . .	59
3.29	Equilibrium flow quadrant-event frequency, $\kappa = 2$ . . . . .	61
3.30	Disturbed flow quadrant-event frequency, $\kappa = 2$ . . . . .	61
3.31	Peak values of the equilibrium flow Reynolds stress quadrant events at $y/\delta = 0.02$ , $\kappa = 1$ . . . . .	62
3.32	Peak value of the disturbed flow Reynolds stress quadrant events at $y/\delta = 0.02$ , $\kappa = 1$ . . . . .	63
4.1	Dyadic arrangement of wavelet coefficients, $N = 5$ . . . . .	69
4.2	Four different scales of the Daubechies extremal phase wavelet with 8 coefficients. . . . .	70
4.3	Power spectrum magnitude of the D8 wavelets at several scales for a sampling rate of 32768 Sa/s ( $\Delta t_s = 30.5 \mu s$ ). . . . .	71
4.4	D8 power scalar densities of the equilibrium flow $u$ , $v$ , and $p$ time records at $y/\delta = 0.02$ . . . . .	72
4.5	Normalized D8 FWT magnitude of a segment of the equilibrium flow $u$ velocity at $y/\delta = 0.02$ . . . . .	73
4.6	Segment of equilibrium $u$ velocity before and after conventional wavelet filtering with $k_f = 0.99$ and $0.90$ . . . . .	74
4.7	Power spectra of the equilibrium flow $u$ velocity before and after F2 wavelet filtering. . . . .	76
4.8	Power spectra of the equilibrium flow wall pressure before and after F2 wavelet filtering. . . . .	77
4.9	Effects of F2 wavelet filtering on equilibrium flow $u$ , $v$ , and $p_1$ at $y/\delta = 0.02$ . . . . .	78
4.10	Effects of F2 wavelet filtering on disturbed flow $u$ , $v$ , and $p_1$ at $y/\delta = 0.02$ . . . . .	79

4.11	Distribution of the time between equilibrium flow $p_{wf}$ peak events, $\kappa = 1$ .	80
4.12	Distribution of the time between disturbed flow $p_{wf}$ peak events, $\kappa = 1$ .	81
4.13	Equilibrium flow quadrant-event frequency after F2 wavelet filtering, $\kappa = 2$ .	81
4.14	Disturbed flow quadrant-event frequency after F2 wavelet filtering, $\kappa = 2$ .	83
4.15	Equilibrium ensemble averages conditioned on peak wall pressure events before filtering.	84
4.16	Equilibrium ensemble averages conditioned on peak wall pressure events after filtering.	84
4.17	Disturbed ensemble averages conditioned on peak wall-pressure events before filtering.	85
4.18	Disturbed ensemble averages conditioned on peak wall-pressure events after filtering.	85
4.19	Equilibrium ensemble averages conditioned on peak Q2 events before filtering.	87
4.20	Equilibrium ensemble averages conditioned on peak Q2 events after filtering.	87
4.21	Disturbed ensemble averages conditioned on peak Q2 events before filtering.	88
4.22	Disturbed ensemble averages conditioned on peak Q2 events after filtering.	88
5.1	Equilibrium wall pressure and localized variance with $T_v^+ = 9.6$ .	94
5.2	Disturbed wall pressure and localized variance with $T_v^+ = 4.8$ .	95
5.3	Localized windowed peak detection with $T_w = 50$ samples.	96
5.4	LWPD cluster detection on equilibrium $p_{F2}$ and $uv_{F2}$ with $T_w^+ = 60$ .	98
5.5	LWPD cluster detection on disturbed $p_{F2}$ and $uv_{F2}$ with $T_w^+ = 30$ .	99
5.6	Normalized correlation between $\mathcal{V}_{p_1}$ and $\mathcal{V}_{uv}$ across the equilibrium TBL.	101
5.7	Normalized correlation between $\mathcal{V}_{p_1}$ and $\mathcal{V}_{uv}$ across the disturbed TBL.	102
5.8	Normalized correlation between $\mathcal{V}_{p_1}$ and $\mathcal{V}_{uv}$ at two locations in the equilibrium and disturbed flows.	103
5.9	Time delays for maximum correlation between wall pressure and Reynolds stress.	104
5.10	Ensemble averages conditioned on equilibrium flow Q2 LWPD clusters at $y/\delta = 0.02$ .	105
5.11	Ensemble averages conditioned on disturbed flow Q2 LWPD clusters at $y/\delta = 0.02$ .	106
5.12	Ensemble averages conditioned on equilibrium flow wall pressure LWPD clusters at $y/\delta = 0.02$ .	107

5.13	Ensemble averages conditioned on disturbed flow wall pressure LWPD clusters at $y/\delta = 0.02$ . . . . .	107
6.1	Ensemble-averaged equilibrium perturbation flow field conditioned on wall-pressure LWPD clusters prior to F2 filtering. . . . .	111
6.2	Ensemble-averaged equilibrium perturbation flow field conditioned on wall pressure LWPD clusters after F2 filtering. . . . .	112
6.3	The mechanics of streak breakup after Kline, et al. 1967. . . . .	113
6.4	Ensemble-averaged disturbed perturbation flow field conditioned on wall-pressure LWPD clusters prior to F2 filtering. . . . .	114
6.5	Ensemble-averaged disturbed perturbation flow field conditioned on wall pressure LWPD clusters after F2 filtering. . . . .	115
A.1	Wall-pressure spectra downstream of the disturbed flow ramp. . . . .	124
A.2	Distribution of rms wall pressure downstream of the disturbed flow ramp. . . . .	124

## Tables

3.1	Nominal boundary-layer properties and measurement resolutions. . .	32
3.2	Wall pressure statistics, averaged over the X-wire surveys. . . . .	45
3.3	Effects of high-pass filtering on equilibrium TBL wall pressure skewness. . .	47
3.4	Wall pressure peak-event detection statistics for transducer $p_1$ . . . . .	52
3.5	Reynolds stress peak-event detection statistics. . . . .	57
3.6	Reynolds stress quadrant-event detection statistics, $\kappa = -2$ . . . . .	60
4.1	D8 wavelet scales and approximate center frequencies for a sampling rate of 32768 Sa/s ( $\Delta t_s = 30.5 \mu s$ ). . . . .	72
4.2	The F2 wavelet filter. . . . .	76
4.3	Wall pressure peak-event statistics for transducer $p_1$ after F2 wavelet filtering. . . . .	80
4.4	Reynolds stress quadrant-event detection statistics after F2 wavelet filtering, $\kappa = -2$ . . . . .	82
5.1	LWPD statistics for positive wall pressure peaks. . . . .	97
5.2	Convection velocity of organized structures for equilibrium data. . . .	100
5.3	Convection velocity of organized structures for disturbed data. . . .	100
B.1	Instrumentation specifications and estimated uncertainties. . . . .	126

## Nomenclature

$a$	Wavelet transform scale parameter
$b$	Wavelet transform shift parameter
$a_{ij}, b_{ij}$	X-wire calibration coefficients
$A, B$	King's law constants
$C_f$	Coefficient of skin friction
$C_\ell, C_{m,n}$	Wavelet transform coefficients
$d$	Diameter
$E$	Voltage
$f$	Function or frequency, Hz
$\mathcal{F}$	Fourier transform
$G$	Clauser shape factor, $U_e(H - 1)/(u_\tau H)$
$h$	Step height
$H$	Conventional shape factor, $\delta^*/\theta$
$I$	Indicator function for conditional sampling
$k_f$	Wavelet filter energy fraction
$k_1$	Streamwise component of the wavenumber vector
$K_T$	Turbulence kinetic energy, $(u_1^2 + u_2^2 + u_3^2)/2$
$l$	Hot wire/X-wire sensing length
$l_\nu$	Viscous or wall length scale, $\nu/u_\tau$
$\ell$	Wavelet transform coefficient index
$m$	Wavelet transform scale index
$M$	Number of event realizations
$n$	King's law exponent or wavelet transform time index
$N$	Number of samples
$NC$	Normalized correlation function
$p$	Fluctuating pressure
$Q$	Calibration velocity
$R$	Correlation function
$Re_\theta$	Reynolds number based on momentum thickness
$s$	Microphone sensitivity
$t$	Time
$t_s$	Digital sampling interval
$t_\nu$	Viscous or wall time scale, $\nu/u_\tau^2$
$T$	Averaging time or temperature



$T_{ref}$	Calibration reference temperature
$T_w$	Hot wire operating temperature, LWPD detection time window
$\Delta t$	Event duration
$\Delta t_s$	Sampling interval
$\Delta T$	Time between events
$u$	Fluctuating streamwise velocity
$u_i$	Fluctuating velocity component in the $i$ th direction
$u_\tau$	Shear velocity, $(\tau_w/\rho)^{1/2}$
$U$	Mean streamwise velocity
$U_c$	Streamwise convection velocity
$U_e$	Streamwise velocity at boundary-layer edge
$U_i$	Mean velocity component in the $i$ th direction
$v$	Fluctuating wall-normal velocity
$V$	Mean wall-normal velocity
$\mathcal{V}$	Localized variance function
$w$	Wavelet filter weighting function
$\mathcal{W}$	wavelet transform
$x, y, z$	Cartesian coordinates in the streamwise, outward wall-normal, and transverse directions, respectively
$\delta$	Boundary-layer thickness, where $U = 0.99U_e$
$\delta_d$	Location of disturbance layer
$\delta^*$	Boundary-layer displacement thickness
$\theta$	Boundary-layer momentum thickness
$\kappa$	Peak-event detection threshold
$\nu$	Kinematic viscosity
$\rho$	Density
$\tau_w$	Wall shear stress
$\phi$	X-probe orientation angle
$\Phi$	Auto or cross spectral density
$\Phi^w$	Wavelet power scalar density
$\psi$	wavelet function
$\omega$	Frequency, rad/s
$\overline{(\quad)}$	Mean value or time average
$D/Dt$	Substantial derivative, $\frac{\partial}{\partial t} + U_i \frac{\partial}{\partial x_i}$
$(\quad)^+$	Quantity scaled on wall variables $l_\nu$ or $t_\nu$
$(\quad)_{cl}$	LWPD clusters
$(\quad)_{F2}$	Quantity after F2 wavelet filtering
$(\quad)_{wf}$	Quantity after conventional wavelet filtering
$\langle \quad \rangle$	Mean value or ensemble average

## Abbreviations

D8	Daubechies 8-coefficient extremal-phase wavelets
DTBL	Disturbed turbulent boundary layer
ETBL	Equilibrium turbulent boundary layer
FFT	Fast Fourier transform
FWT	Fast wavelet transform
GPIB, HP-IB	General Purpose/Hewlett Packard Interface Bus
IEEE	Institute of Electrical and Electronics Engineers
LNFF	Low Noise Flow Facility
LVAR	Localized variance event-detection technique
LWPD	Localized windowed peak-detection technique
PSD	Power spectral density
PScD	Wavelet power scalar density
rms	Root-mean-square
SPL	Sound pressure level
TBL	Turbulent boundary layer

## Chapter 1

### Introduction

#### 1.1 Motivation

There are times when it is desirable to have a fluid flow in a highly agitated, turbulent state. In such cases, the early transition of flow from laminar to turbulent is actively sought. Dimples on a golf ball and mixing vanes in jet engine combustors and industrial furnaces are examples. In the first case, the turbulence delays boundary-layer separation, thus lowering the pressure drag and allowing the ball to fly farther. In the second case, the turbulence enhances the mixing of oxidizer and fuel, increasing the combustion efficiency. On the other hand, turbulence can also be a hindrance. Examples here include the boundary layers on aircraft wings and ship hulls, where the turbulence increases the skin friction drag and lowers fuel efficiency. The actions of the turbulent motions are also transmitted as forces on the constraining surfaces, which can couple with the vibrational modes of the structure [1.1]. The result can be accelerated structural fatigue and increased radiated noise, both inside and outside of the structure. These examples on the negative effects provide the motivation to control the turbulence to mitigate or eliminate the undesirable effects.

Efforts to control turbulent flows have focused primarily on the manipulation of quasi-periodic, coherent flow structures [1.2], since it is generally accepted that such structures are responsible for the production and maintenance of boundary-layer turbulence [1.3]. Most of the work to date has been in the area of passive control, where the inputs to the flow boundary conditions are static. In contrast, active control involves dynamic inputs to the flow. The topic has been recently reviewed by Bushnell and McGinley [1.4], who point out that

The probable key to increasing the effectiveness of dynamic inputs ... is correct *phasing*. The turbulence dynamics, due to phase jitter and variability in size/strength of the various motions, occurs randomly in both space and time. ... sensor-feedback control loops are evidently required for treating the random-phase problem in the turbulence dynamics.

For a feedback control system, it is desirable that the sensor be nonintrusive.

This naturally leads one to consider flow variables at the wall, of which the fluctuating wall pressure is the most readily measured. If the turbulence is to be controlled through the sensing of the wall pressure, it is imperative that the relationship between the two be thoroughly understood. Numerous investigations have established a link between near-wall shear layers associated with turbulence production and wall-pressure peak events; the so-called bidirectional relationship (cf. Section 1.2.2). However, these studies were for fully developed turbulent boundary layers flowing over smooth flat plates with zero pressure gradient, or for fully developed turbulent flow through smooth pipes. Real-world applications will rarely involve such a flow. A host of disturbances to the ideal case are possible, indeed, probable. The present research, therefore, has two broad aims: to clarify the causal relationship between the organized structures and the wall-pressure events for equilibrium flows, and to examine this relationship in a *disturbed* flow.

## 1.2 Background

### 1.2.1 Physical features of turbulent boundary layers

The following overview of the structural features of the turbulent boundary layer (TBL) is based primarily on the summary work of Robinson [1.3] and Kline and Robinson [1.5]. *Organized motions* or *coherent structures* are defined as spatial regions of the flow over which at least one fundamental flow variable exhibits significant correlation with itself or with another variable. The *inner layer* or *near-wall region* refers to the region  $y^+ = yu_\tau/\nu \leq 100$ , where  $y$  is the distance from the wall in the wall-normal direction,  $u_\tau$  is the shear velocity, and  $\nu$  is the kinematic viscosity. It includes the sublayer, the buffer region, and at least part of the logarithmic region. The rest of the boundary layer is called the *outer layer*.

To understand the mechanisms of turbulence production and dissipation, one must examine the governing equations. The total velocity in the  $i$ th direction is represented as a mean and a fluctuation,  $U_i + u_i$ . If this representation is substituted into the Navier-Stokes equations for incompressible flow, the equation for the turbulence kinetic energy  $K_T = (u_1^2 + u_2^2 + u_3^2)/2 = u_i u_i / 2$  can be obtained as:

$$\frac{DK_T}{Dt} = -\overline{u_i u_j} \frac{\partial U_i}{\partial x_j} - \nu \overline{\frac{\partial u_i}{\partial x_j} \frac{\partial u_i}{\partial x_j}} - \frac{\partial}{\partial x_j} \left[ \overline{K_T u_j} + \frac{\overline{p u_j}}{\rho} - \nu \frac{\partial K_T}{\partial x_j} \right] \quad (1.1)$$

where  $D/Dt$  is the substantial derivative,  $\rho$  is the density, and  $p$  is the fluctuating pressure. Overbars represent time averages. In this expression, the first term on the right-hand side represents turbulence production driven by the mean shear and the second term represents dissipation through viscosity. The third term in brackets denotes three forms of turbulence transport. The goal of active control is to inhibit the production term.

For positive production to occur, the Reynolds stresses  $-\overline{u_i u_j}$  must be positive, which means that the fluctuating components must be of opposite sign. In wall-bounded flows, the mean shear is  $\partial U/\partial y$ , where  $U_1 = U$  is the mean streamwise velocity and  $x_2 = y$ . Production, then, occurs if  $u_1 = u < 0, u_2 = v > 0$  or  $u > 0, v < 0$ , which correspond to the second and fourth quadrants of the  $u$ - $v$  plane. The first case is referred to as a Q2,  $uv_2$ , or *ejection* motion. The second case is referred to as a Q4,  $uv_4$ , or *sweep* motion.

The production and dissipation of turbulence in wall-bounded flows is carried out predominantly through quasi-periodic, organized motions. Across the boundary layer, these coherent motions exhibit a broad range of spatial and temporal scales. In general, they consist of both inner-layer motions and outer-layer structures that act across the complete boundary layer. The following (unsorted) classification, taken directly from Robinson [1.3, pp. 606–607], summarizes the experimentally observed forms of coherent motions:

1. Low-speed streaks in the viscous sublayer
2. Ejections of low-speed fluid outward from the wall, including lifting low-speed streaks
3. Sweeps of high-speed fluid inward toward the wall, including intrushes from the outer region
4. Vortical structures of various forms
5. Sloping near-wall shear layers, exhibiting local concentrations of spanwise vorticity and  $\partial u/\partial x$
6. Near-wall “pockets” visible in the laboratory as regions swept clean of marked near-wall fluid
7. Large ( $\delta$ -scale) motions capped by three-dimensional bulges in the outer turbulent/potential interface
8. Shear-layer “backs” of large-scale outer-region motions, consisting of sloping ( $\delta$ -scale) discontinuities in the streamwise velocity

The inner-layer motions, items 1–6, are responsible for the majority of the turbulence production. They are termed *active motions*, and occur intermittently over relatively small time and space scales. In contrast, the temporal and spatial scales of the organized structures in the outer region of the TBL are much larger and roughly scale on the freestream velocity and boundary-layer thickness. These structures are termed *passive* because they are not directly linked to turbulence production.

The first three items of the classification are related to what has been historically called the bursting process. The term “bursting” originally described the oscillation

and violent breakup of a low-speed streak after lifting, followed by an inrush of fluid, or sweep. The emphasis was on a process that is highly intermittent in time. An alternative viewpoint has evolved in which the burst is an ejection caused by the passage of a tilted vortex, which is localized in space but persists for long times. Such a region passing a stationary probe would produce sudden velocity excursions at the measurement location without making clear the passage of an associated flow structure. The disparate meanings of "bursting" throughout the literature prompted Kline and Robinson to exclude the term from the above classification [1.3].

Vortices and vortex dynamics (item 4) play a central role in the description of turbulent flows. At a fundamental level, the transfer of turbulent energy from large to small scales occurs through vortex stretching [1.6]. In this process, vortices are elongated by the mean shear. As the cross-sectional area of the vortex decreases, conservation of angular momentum leads to an increase in vorticity and kinetic energy. The stretched vortex induces a strain-rate field, which stretches vortices of different orientation. As the process continues, kinetic energy is redistributed among the coordinate directions, leading to local isotropy at the smallest scales.

Vortical structures have been identified by numerous investigations, and are the basis for most conceptual models of the turbulence production dynamics. Head and Bandyopadhyay [1.7], using motion-picture flow visualization and hot-wire measurements, documented the existence of large numbers of vortex structures in the TBL. The vortices originate at the wall and extend through a large part of the boundary layer or beyond. At low Reynolds numbers, these vortices form horseshoe or loop shapes. At high Reynolds numbers, they become elongated into hairpin vortices or vortex pairs.

Thomas and Bull [1.8] synthesized a model for the large-scale motions associated with the burst-sweep cycle from simultaneous measurements of velocity, wall shear stress, and wall pressure. Figure 1.1 shows plan and side views of their model. The most prominent features are a  $\delta$ -scale horseshoe vortex and an inclined shear layer. Recently, Snarski and Lueptow [1.9] inferred a similar structure from detailed correlations between the wall pressure and streamwise velocity. Their model includes secondary, counter-rotating vortices between the fronts and backs of the primary large-scale structures.

Robinson [1.3, 1.10] constructed a model for low-Reynolds number TBLs, which was deduced from a review of both experimental and direct numerical simulation data. Inclined quasi-streamwise and spanwise vortices, sometimes forming horseshoe or hairpin shapes, form the core structures. Quasi-streamwise vortices dominate the inner layer, while archlike vortices are the most common structure in the outer layer. In the logarithmic, or overlap, region, both types of vortex exist together, often as elements of the same structure. The two types of structure and the kinematical relationships between ejection/sweep motions are illustrated in Figure 1.2.

Even with a wide consensus on the above boundary-layer structures, there are still open questions. In particular, the coupling between the inner and outer flow

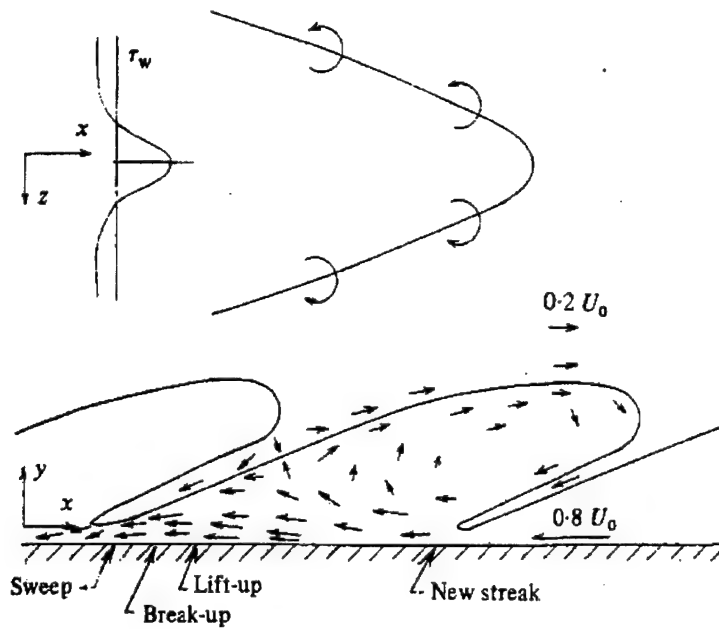


Figure 1.1: Plan and side views of the large-scale structure associated with the burst-sweep cycle in a frame of reference moving with the structure. From Thomas and Bull [1.8].

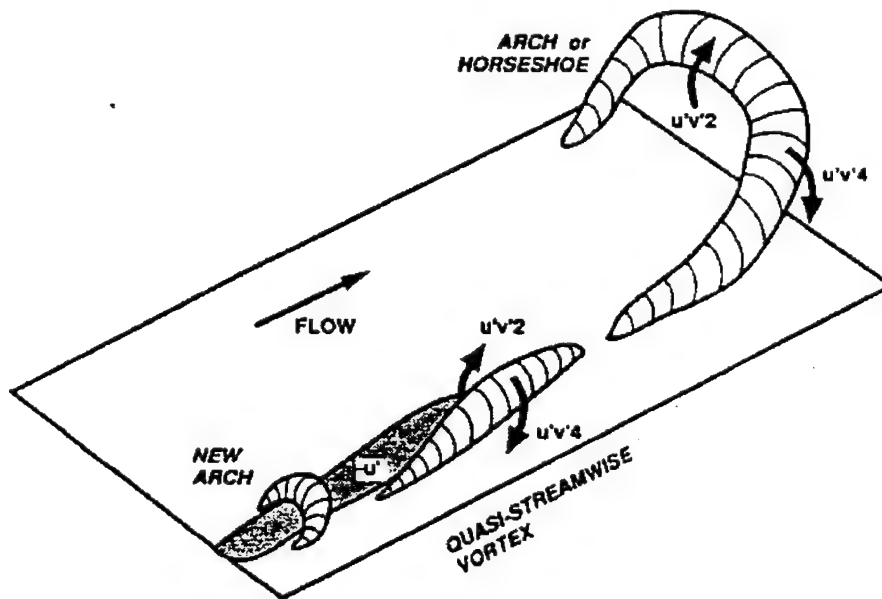


Figure 1.2: Vortical structures and ejection/sweep motions in the turbulent boundary layer. From Robinson [1.3].

motions is not completely understood. On the one hand, the inner-region production should intuitively scale on the wall variables  $u_\tau$  and  $\nu$ . Indeed, some researchers have found that the rate of bursting near the wall, usually deduced by the passage of streamwise shear layers, is constant when scaled on wall variables [1.11]. However, others have concluded that the burst rate is linked to the outer flow [1.9, 1.12]. Addressing this inner/outer controversy, Kline and Robinson [1.5] conclude that while the majority (70 percent or more) of the turbulence production in the inner layer is self-maintaining by events in the inner layer itself, it can be significantly affected by outer-layer or freestream motions. This raises the following question: Are some flow structures unaffected by outer-layer motions, and hence, universal to turbulent boundary layers, or are all motions modified in some way? The answer has implications for the application of turbulence control in the presence of real-world disturbances, since the control strategy may have to change with the flow situation.

### 1.2.2 Wall-pressure fluctuations

Wall-pressure fluctuations beneath turbulent boundary layers have been extensively studied. Eckelmann [1.13] provides a recent review of the subject. For an incompressible flow, the fluctuating pressure is related to the fluctuating velocity through the Poisson equation:

$$\frac{\partial^2 p}{\partial x_i^2} = -\rho \left[ 2 \frac{\partial U_i}{\partial x_j} \frac{\partial u_j}{\partial x_i} + \frac{\partial^2}{\partial x_i \partial x_j} (u_i u_j - \overline{u_i u_j}) \right] \quad (1.2)$$

The right-hand side of this equation represents two sources of wall-pressure fluctuations. The first term is linear, and is due to interaction of the mean shear with the turbulence. The second term is nonlinear and represents the interactions of the velocity fluctuations with themselves. The fluctuating pressure at the wall is obtained as an integration of the Poisson equation over the entire upper half-plane. Since the totality of fluid motions within the boundary layer are reflected onto the surface, the wall-pressure fluctuations contain a broad range of temporal and spatial scales.

The statistical and spectral properties of the fluctuating wall pressure have been addressed in detail by Schewe [1.14] and Karangelen [1.15]. They found that, compared to a random signal with Gaussian probability density function, the wall pressure contains many more large-amplitude excursions from the mean, and that negative large-amplitude events occur more often than positive events. This latter finding is not supported in the work of Wilczynski [1.16] or in the present research, where positive and negative events were found to be equally likely (cf. section 3.3.3). Schewe also investigated the effects of transducer size on the measured statistics. He showed that the probability density function approaches a Gaussian distribution as the transducer size increases. This is because an increasing number of independent stochastic processes occur over the active sensing area.



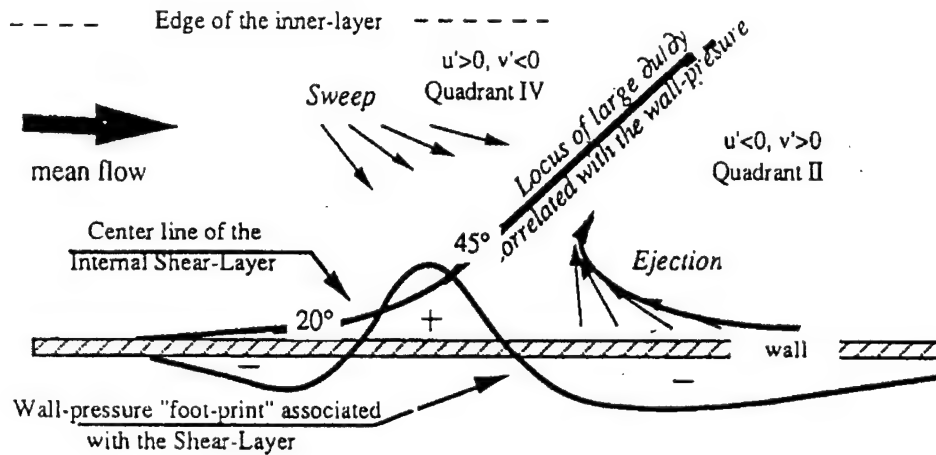


Figure 1.3: Schematic of near-wall turbulent motion and associated wall pressure. From Astolfi and Forestier [1.21].

Many researchers have investigated the relationship between the wall pressure and coherent flow structures. The measurements suggest at least two groups of pressure fluctuations stemming from the inner- and outer-flow structures. Kobashi and Ichijo [1.17] separated the two signatures by performing correlations between velocity and high- and low-pass filtered pressure data. The low-pass filtered pressure exhibited high correlation with the velocity across the boundary layer. The high-pass filtered data was correlated with the velocity only in the near-wall regions. Thomas and Bull [1.8] performed similar filtering and found that the high-frequency pressure fluctuations were associated with the burst-sweep cycle of near-wall events. The above results are consistent with the findings of Farabee and Casarella [1.18], who showed that the high-frequency part of the wall-pressure spectrum scales on wall variables, while the low frequency part scales on outer-flow variables.

Conditional sampling based on large-amplitude wall-pressure peaks and near-wall flow structures has confirmed a bidirectional relationship between the two. Johansson, Her, and Haritonidis [1.19], conditioning on near-wall shear layers, found that negative wall-pressure peaks were associated primarily with sweep-type motions. Haritonidis, Gresko, and Breuer [1.20] reached a similar conclusion and also state that the primary connection between the wall pressure and the flow field is through the normal component of velocity,  $v$ . Wilczynski [1.16] performed conditional sampling on the Reynolds stress and found that large-amplitude wall-pressure peaks are related to Q2 and Q4 motions. The sequence has been clarified by Astolfi and Forestier [1.21] who performed conditional sampling and correlation on the wall pressure and flow regions of large  $\partial u / \partial y$ . Their schematic view of the near-wall turbulence and associated wall pressure is shown in Figure 1.3. The results of this dissertation are, to a large extent, consistent with this model.

Though the link between the wall pressure and near-wall motions is established,

the causal relationship between them is not understood. In a study of data obtained from a large-eddy simulation of turbulent channel flow, Kim [1.22] found that the ejection process at the end of a sweeping motion was associated with a localized adverse pressure gradient. This is in contrast with Thomas and Bull [1.8], who concluded that the adverse pressure gradients associated with characteristic pressure patterns are not the direct cause of the bursting process. Furthermore, Haritonidis, et al. [1.20] state that "Positive pressures, in general, appear to be the result of wallward moving fluid being retarded by the presence of the wall." This issue needs to be resolved before proper strategies for active turbulence control can be implemented.

### 1.2.3 Conditional sampling

In outlining the history of research into turbulent boundary-layer structure, Robinson identified the period 1972–1979 as the conditional sampling era [1.3, p. 611]. Conditional sampling has played a central role in confirming and establishing relationships among the various types of TBL structure. As pointed out in the review by Antonia [1.23], it has helped to close the gap between data collected in an Eulerian frame of reference and information in a Lagrangian frame, as provided by flow-visualization experiments. It continues to figure prominently in the analysis of virtually all digital experimental data, including the present investigation. Therefore, a brief review is in order.

Conditional sampling is generally performed by first identifying those periods of a signal that are "interesting;" i.e., some event detection criteria. These periods define an indicator function,

$$I(t) = \begin{cases} 1, & t = t_I \\ 0, & \text{otherwise} \end{cases} \quad (1.3)$$

The times  $t_I$  are those for which the event criteria is satisfied. By identifying alignment points  $t_m$  within the contiguous ranges of  $t_I$ , conditional or ensemble averages corresponding to the event-detection criteria can be formed:

$$\langle f(\tau) \rangle = \frac{1}{M} \sum_{m=1}^M f(t_m + \tau) \quad (1.4)$$

In this expression,  $M$  is the number of event realizations and  $\tau$  is the delay. The indicator function can be formed from  $f$  or another function at the same or a different position in space. When the triggering is at a different spatial location, random variations in transit times of the flow structures can significantly degrade the coherence of the ensemble average. This problem is referred to as *phase jitter*, and has been addressed by Blackwelder [1.24]. Different conditional sampling methods are distinguished from one another by the criteria or algorithms that define

I. The most common methods in the literature include the variable-interval time average (VITA), the  $u$ - $v$  quadrant, and the peak-event detection methods. Direct comparisons between the various methods have recently been done by Yuan and Mokhtarzadeh-Dehghan [1.25].

The VITA method computes the short-time variance of the signal and identifies an event as occurring when this quantity exceeds a certain threshold. The method is usually applied to the streamwise velocity, but has been applied to the wall-normal velocity and the Reynolds stress as well. Variations on VITA include distinguishing the slope of the function as well as the absolute level. When applied to velocity signals, the VITA technique is essentially a shear layer detector. Most of the work establishing the wall-pressure/near-wall flow structure relationship, cited in the previous section, was based on the VITA technique.

The  $u$ - $v$  quadrant method queries the sign of  $u$  and  $v$  to distinguish the four quadrants of the  $u$ - $v$  plane. This allows one to focus directly on the turbulence-producing motions (quadrants 2 and 4). If only strong events are of interest, an additional threshold value on the  $uv$  product may also be required. Similar to the quadrant-plus-level method, peak-event detection is perhaps the most straightforward means of conditioning ensemble averages. Here, an event is deemed to occur when the signal amplitude exceeds a given threshold. The work of Schewe [1.14] and Karangelen [1.15] made extensive use of this technique in studying the statistics of the wall pressure. Wilczynski [1.16] used both quadrant and peak-event techniques in proposing that Q2-Q4 event pairs are linked to wall-pressure peak events.

While conditional sampling has been extremely useful in illuminating coherent motions in the boundary layer, one must exercise care in its application. All of the methods require the input of one or more arbitrary parameters, in the form of averaging times or thresholds. The results obtained are highly dependent on the values chosen. Another difficulty, pointed out by Tiederman [1.26], occurs when a detection scheme triggers on different portions of the same flow structure. For example, from an Eulerian viewpoint, a single burst may contain several ejections. If the multiple ejections are not grouped into one event realization, skewed results will be obtained. A more general event-detection scheme that requires a minimum number of independent parameters is preferred. In addition, an approach that recognizes groupings of events, or *clusters*, that are associated with the passage of organized motion is required.

### 1.3 Research objectives and experimental approach

This research seeks to address two related questions that are central to the design of active turbulence control systems:

1. What are the detailed features of near-wall flow structures associated with wall-pressure peak events beneath turbulent boundary layers?

2. Are these near-wall structures coupled to and affected by the outer-layer dynamics?

To answer these questions, a series of experiments was performed in which simultaneous measurements of the fluctuating wall-pressure and the streamwise and wall-normal velocity were obtained. High-quality databases of time-resolved digital, statistical, and spectral data were constructed for each of two separate flows. The first flow consisted of a fully developed, turbulent boundary layer over a smooth wall with zero pressure gradient — the equilibrium or canonical case. The second flow was a nonequilibrium or disturbed turbulent boundary layer, in which the disturbances were primarily confined to the outer regions of the boundary layer. Specifically, the disturbed flow was that formed downstream of reattachment of the flow over an aft-facing step.

Once the data were collected, the following tasks were necessary to address the stated objectives:

- Confirm that wall-pressure peak events are footprints of near-wall organized motion in the equilibrium layer using traditional conditional sampling techniques.
- Develop appropriate filtering to extract the near-wall motions associated with wall-pressure peak events in the disturbed layer.
- Formulate a new conditional sampling approach that recognizes cluster groupings of events in order to test the robustness of the results.
- Document the spatial extent of the observed near-wall, turbulence-producing motions.

The two turbulent boundary layers studied will now be described.

### 1.3.1 Equilibrium turbulent boundary layer

The criteria for the existence of a fully developed, equilibrium turbulent boundary layer are given by Hussain [1.27]:

- A mean streamwise velocity profile with conventional shape factor  $H \approx 1.4$ , Clauser shape factor  $G \approx 6.3$ , and shear-to-freestream velocity ratio  $u_\tau/U_e = f(Re_\theta) \approx 0.04$ .
- A mean streamwise velocity profile with a log-law region of adequate extent based on the flow Reynolds number.
- A wake strength that is appropriate for the flow Reynolds number.
- A peak in the turbulence intensity profile of  $u/u_\tau = 2.5 \pm 10\text{percent}$ .

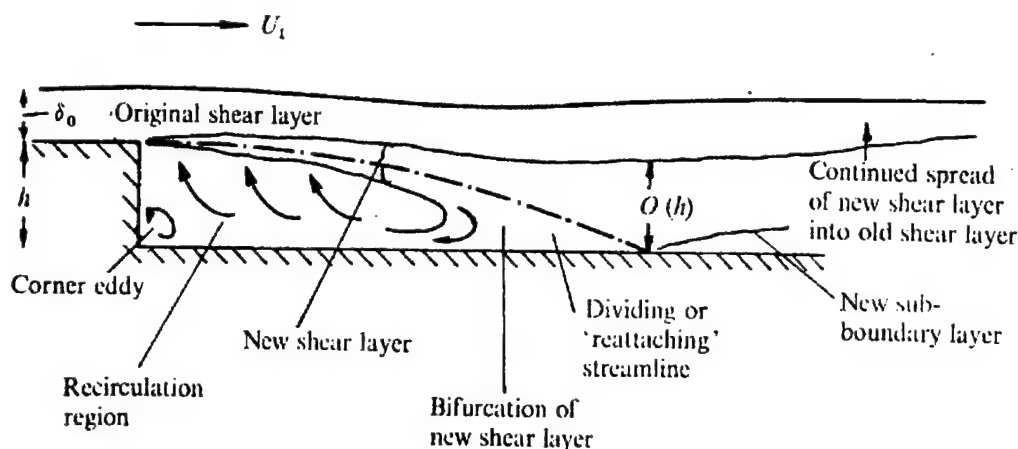


Figure 1.4: Features of the flow over a backward-facing step. From Bradshaw and Wong [1.30].

- A location of the peak turbulence intensity at  $y^+ = 15$ .
- A monotonic decrease in  $u$  to the freestream value.
- A broadband, continuous  $u$  spectrum that contains an inertial subrange.

In addition, the wall pressure rms level should be appropriate for the flow Reynolds number and have a smooth spectrum with no apparent discontinuities. These characteristics are confirmed for the present study in Chapter 3.

### 1.3.2 Disturbed turbulent boundary layer

The disturbed flow chosen for this study approximated the flow downstream of reattachment of flow over a backward-facing step. The selection was based on previous studies of step flows conducted in the same facility [1.28, 1.29]. The flow was obtained by installing a ramp on the equilibrium TBL test surface. The ramp had an inclination of 1.7 deg and terminated in a backward-facing step of height 1.5 cm. One advantage is a fixed point of separation. While not strictly the same as flow over a step, the ramp flow provided the desired disturbed TBL for comparison with the equilibrium case.

The characteristic features of flow over a backward-facing step are illustrated schematically in Figure 1.4, taken from Bradshaw and Wong [1.30]. The following discussion is based on the detailed measurements of Chandrsuda and Bradshaw [1.31] and Farabee and Casarella [1.28, 1.29]. The flowfield can be described in terms of overlapping zones. In the first zone, an initial or inflow boundary layer flows along the top of the step. At the edge of the step, the boundary layer separates and a free shear layer forms over a second zone of recirculating flow. The shear layer grows and

makes contact with the wall over a third zone of reattachment, which contains high levels of turbulence activity. Immediately downstream of reattachment, a boundary layer develops which is highly energized and has the characteristics of an attached free shear layer. This developing layer has a log law region even very close to reattachment. As the flow moves downstream, the boundary layer relaxes, eventually becoming an equilibrium TBL.

The rms wall pressure peaks just upstream of reattachment, decreasing monotonically thereafter. The magnitude of the peak is three to five times greater than for a flat plate, depending on the thickness of the inflow boundary layer. The wall-pressure spectrum exhibits increased low-frequency components compared to the flat plate case. Similar to the rms values, the highest spectral levels occur at reattachment, followed by a rapid decrease in the low-frequency components as the flow moves downstream.

## 1.4 Outline of dissertation

The following chapters present the details of the experimental measurements and the signal processing methods used to extract the desired information. Chapter 2 documents the experimental setup and methods used to obtain simultaneous wall pressure and flowfield velocity measurements across the equilibrium and disturbed turbulent boundary layers. The long-time averaged properties of the two flows are presented in Chapter 3. It will be shown that the disturbed TBL differs from the equilibrium TBL by the addition of large-scale, low-frequency disturbances in the outer regions of the boundary layer, but that the inner layers appear to be substantially the same. The hypothesis is made that the inner and outer layer portions of turbulent boundary layers are uncoupled.

To test this hypothesis, Chapter 4 implements a wavelet filtering scheme to isolate the common near-wall features of both flows. The analysis of the data is further enhanced using the idea of event clusters, introduced in Chapter 5. Two new analysis methods, Localized Variance and Localized Windowed Peak Detection, will be used to form correlations and conditionally sampled ensemble averages of the flowfield structures of interest. Correlations will be used to compute convection velocities of the wall-pressure events, and conditional sampling results will confirm the bidirectional relationship between positive wall-pressure peaks and accelerating  $u$ -velocity or second-quadrant  $uv$  motions. Finally, Chapter 6 assembles the results into a composite picture of the near-wall motions, allowing the fundamental questions of the research to be addressed.

## References

- [1.1] Y. F. Hwang and G. Maidanik. A wavenumber analysis of the coupling of a

- structural mode and flow turbulence. *J. of Sound and Vibration*, 142(1):135–142, 1990.
- [1.2] H. Choi, R. Temam, P. Moin, and J. Kim. Feedback control for unsteady flow and its application to the stochastic Burgers equation. *J. Fluid Mech.*, 253:509–543, 1993.
  - [1.3] S. K. Robinson. Coherent motions in the turbulent boundary layer. *Annu. Rev. Fluid Mech.*, 23:601–639, 1991.
  - [1.4] D. M. Bushnell and C. B. McGinley. Turbulence control in wall flows. *Annu. Rev. Fluid Mech.*, 21:1–20, 1989.
  - [1.5] S. J. Kline and S. K. Robinson. Quasi-coherent structures in the turbulent boundary layer. Part I: Status report on a community-wide summary of the data. In Kline and Afgan, editors, *Near-Wall Turbulence: Proceedings of the 1988 Zoran Zaric Memorial Conference*, pages 200–217. Hemisphere, 1990.
  - [1.6] H. Tennekes and J. L. Lumley. *A First Course in Turbulence*. The MIT Press, 1972.
  - [1.7] M. R. Head and P. Bandyopadhyay. New aspects of turbulent boundary-layer structure. *J. Fluid Mech.*, 107:297–338, 1981.
  - [1.8] A. S. W. Thomas and M. K. Bull. On the role of wall-pressure fluctuations in deterministic motions in the turbulent boundary layer. *J. Fluid Mech.*, 128:283–322, 1983.
  - [1.9] S. R. Snarski and R. M. Lueptow. Wall pressure and coherent structures in a turbulent boundary layer on a cylinder in axial flow. *J. Fluid Mech.*, 286:137–171, 1995.
  - [1.10] S. K. Robinson. *Kinematics of Turbulent Boundary Layer Structure*. PhD thesis, Stanford University, 1990.
  - [1.11] R. F. Blackwelder and J. H. Haritonidis. Scaling of the bursting frequency in turbulent boundary layers. *J. Fluid Mech.*, 132:87–103, 1983.
  - [1.12] C. E. Wark and H. M. Nagib. Experimental investigation of coherent structures in turbulent boundary layers. *J. Fluid Mech.*, 230:183–208, 1991.
  - [1.13] H. Eckelmann. A review of knowledge on pressure fluctuations. In Kline and Afgan, editors, *Near-Wall Turbulence: Proceedings of the 1988 Zoran Zaric Memorial Conference*, pages 328–347. Hemisphere, 1990.

- [1.14] G. Schewe. On the structure and resolution of wall-pressure fluctuations associated with turbulent boundary-layer flow. *J. Fluid Mech.*, 134:311–328, 1983.
- [1.15] C. C. Karangelen. *Temporal and Spectral Features of Wall Pressure Fluctuations Beneath a Turbulent Boundary Layer*. PhD thesis, The Catholic University of America, 1991.
- [1.16] V. Wilczynski. *Organized Turbulent Structures and Their Induced Wall Pressure Fluctuations*. PhD thesis, The Catholic University of America, 1992.
- [1.17] Y. Kobashi and M. Ichijo. Wall pressure and its relation to turbulent structure of a boundary layer. *Experiments in Fluids*, 4:49–55, 1986.
- [1.18] T. M. Farabee and M. J. Casarella. Spectral features of wall pressure fluctuations beneath turbulent boundary layers. *Phys. Fluids A*, 3(10):2410–2420, 1991.
- [1.19] A. V. Johansson, J. Her, and J. H. Haritonidis. On the generation of high-amplitude wall pressure peaks in turbulent boundary layers and spots. *J. Fluid Mech.*, 175:119–142, 1987.
- [1.20] J. H. Haritonidis, L. S. Gresko, and K. S. Breuer. Wall pressure peaks and waves. In Kline and Afgan, editors, *Near-Wall Turbulence: Proceedings of the 1988 Zoran Zaric Memorial Conference*, pages 397–417. Hemisphere, 1990.
- [1.21] J. A. Astolfi and B. E. Forestier. Flow noise associated with near-wall turbulence structure. In Farabee, Keith, and Lueptow, editors, *Flow Noise Modeling, Measurement, and Control*, number NCA 15/FED 168, pages 1–11. ASME, 1993.
- [1.22] J. Kim. On the structure of wall-bounded turbulent flows. *Phys. Fluids*, 26(8):2088–2097, 1983.
- [1.23] R. A. Antonia. Conditional sampling in turbulence measurement. *Annu. Rev. Fluid Mech.*, 13:131–156, 1981.
- [1.24] R. Blackwelder. On the role of phase information in conditional sampling. *Phys. Fluids*, 20(10):S232–S242, 1977.
- [1.25] Y. Yuan and M. Mokhtarzadeh-Dehghan. A comparison study of conditional-sampling methods used to detect coherent structures in turbulent boundary layers. *Phys. Fluids*, 6(6):2038–2057, 1984.
- [1.26] W. G. Tiederman. Eulerian detection of turbulent bursts. In Kline and Afgan, editors, *Near-Wall Turbulence: Proceedings of the 1988 Zoran Zaric Memorial Conference*, pages 874–887. Hemisphere, 1990.



- [1.27] A. Hussain. Coherent structures—reality and myth. *Phys. Fluids*, 26(10):2816–2850, 1983.
- [1.28] T. M. Farabee. An experimental investigation of wall pressure fluctuations beneath non-equilibrium turbulent flows. Technical Report DTNSRDC-86/047, David Taylor Naval Ship Research and Development Center, Bethesda, Maryland 20084-5000, 1986.
- [1.29] T. M. Farabee and M. J. Casarella. Effects of surface irregularity on turbulent boundary layer wall pressure fluctuations. *Trans. of ASME, J. of Vibration, Stress, and Reliability in Design*, 106(10):343–350, 1984.
- [1.30] P. Bradshaw and F. Y. F. Wong. The reattachment and relaxation of a turbulent shear layer. *J. Fluid Mech.*, 52:113–135, 1972.
- [1.31] C. Chandrsuda and P. Bradshaw. Turbulence structure of a reattaching mixing layer. *J. Fluid Mech.*, 110:171–194, 1981.

## Chapter 2

### Experimental setup and methods

#### 2.1 Introduction

The experiments were performed in the Catholic University Low Noise Flow Facility (LNFF). Two flows were studied: an equilibrium turbulent boundary layer (ETBL) and a disturbed turbulent boundary layer (DTBL). The instrumentation used included sensors to monitor the state of the wind tunnel, two microphones for the measurement of the fluctuating wall pressure, and single-component hot wire and two-component hot film anemometers for the measurement of fluctuating streamwise and wall-normal velocities. In this chapter, the facility, setup, measurement systems and calibration techniques, and data-acquisition hardware will be described, along with a description of the testing procedures and limitations. A detailed measurement uncertainty analysis is presented in Appendix B.

#### 2.2 Facility

The LNFF was constructed specifically for making acoustic measurements of wall pressure beneath turbulent flows. A complete description can be found in [2.1]. A schematic is shown in Figure 2.1. The inlet is covered by honeycomb and multiple screens for turbulence management. This is followed by a 16:1 contraction section designed to provide a gradual static pressure drop and to avoid flow separation along the tunnel walls. The test section is 2.4 m long and 0.6 m  $\times$  0.6 m in cross section. The tunnel is powered by a 25 horse power, variable speed dc motor driving a centrifugal blower in an open-return arrangement. The motor/blower assembly is located in a separate room and is isolated by acoustic mufflers to minimize facility vibrations and acoustic noise levels.

The tunnel speed can be varied from approximately 3 to 30 m/s. At a nominal speed of 16 m/s, the freestream turbulence level  $u_{rms}/U_e$  is approximately 0.2 percent. As documented in earlier studies [2.1–2.3] and confirmed in the present research, the acoustic performance is excellent above approximately 50 Hz. Below

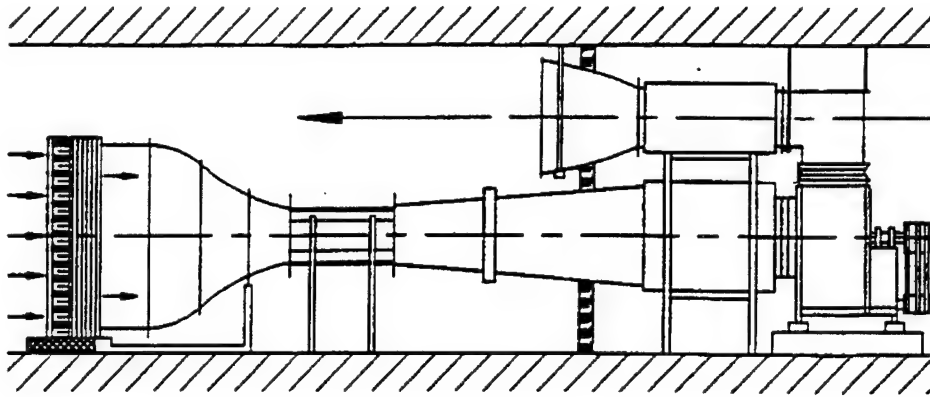


Figure 2.1: The Catholic University Low Noise Flow Facility.

this level, the wall pressure is contaminated by blower-generated acoustic standing waves. As discussed in a later section, this noise is well below the frequency range of interest and is removed by conventional digital filtering.

The boundary layers studied in this investigation were formed on one wall of the wind tunnel. The test wall was constructed of plywood covered with formica. A turbulent layer was ensured through the use of two 0.81-mm diameter trip wires epoxied to the wall 0.3 and 0.9 m upstream of the test section. The measurements were obtained on the tunnel center line at approximately 1.4 m downstream of the test section entrance ( $\approx 2100$  trip heights from the second trip). At this location, the boundary layer is approximately 3 cm thick for a tunnel speed of 16 m/s. The equilibrium state of the boundary layer will be demonstrated in the next chapter.

The disturbed turbulent boundary layer approximated the flow over an aft-facing step. This was accomplished by installing a formica ramp of length 0.51 m on the tunnel wall ending 0.13 m upstream of the measurement station. The step height,  $h$ , was 1.5 cm. The ramp spanned the width of the tunnel, and the leading edge was faired into the tunnel wall using modeling clay. The characteristics of the resulting boundary layers are presented in Chapter 3.

## 2.3 Facility instrumentation

The tunnel conditions were determined through the use of a test cell Pitot-static probe. The Pitot-static difference was measured directly with an Edwards High Vacuum (formerly Datametrics) model 570D-10T-2C2-V1X 0-10 torr differential pressure transducer and model 1174 electronic manometer and power supply. The transducer system zero, full scale, and sensitivity were set daily using internal calibration circuitry. Atmospheric pressure and temperature were measured using a Welch Scientific fixed cistern mercury barometer and a mercury-in-glass thermome-

ter. The density was computed using the perfect gas equation of state. Tunnel velocity was computed using the measured Pitot-static difference and the calculated density through Bernoulli's equation.

As outlined in Section 2.5, the output of a hot-wire anemometer is a function of the static temperature of the fluid. To compensate for temperature changes over the course of the experiments, the static temperature of the tunnel was monitored with a chromel-alumel (type K) thermocouple and Omega type DP11 thermocouple reference junction/monitor. The thermocouple was inserted into the flow through the test wall approximately 0.86 m downstream of the measurement station.

## 2.4 Wall pressure sensors

Wall-pressure measurements were made using two microphones, identified as  $p_1$  and  $p_2$ . Microphone  $p_1$  was mounted at the primary measurement station beneath the hot-wire probe, while microphone  $p_2$  was mounted 1.27 cm upstream of  $p_1$ . The microphones were Brüel and Kjær (B&K) model 4138  $\frac{1}{8}$  in. condenser microphones. Each microphone was connected to a B&K type 2633 preamplifier using a type UA160  $\frac{1}{8}$ -in. to  $\frac{1}{4}$ -in. adapter. Both microphones were powered by a B&K type 2807 two-channel power supply. The signals were then amplified an additional 40 dB (disturbed TBL) or 50 dB (equilibrium TBL) using an Ithaco model 451 amplifier with built-in high-pass filter set at a cutoff frequency of 1 Hz. The phase delay from this filter was less than 1 deg for frequencies greater than 100 Hz. Both the B&K and the Ithaco amplifiers were of the inverting type; their series connection kept the output signal in phase with the fluctuating pressures. Figure 2.2 shows a schematic of the microphone system in relation to the hot-wire and data-acquisition systems. Only one microphone is illustrated for clarity.

The microphone/preamplifier assemblies were inserted into plastic holders, which were in turn mounted in a track attached to the back of the test wall. This allowed the microphone to be positioned at the desired measurement location. The microphone was pushed into the hole until the pinhole cap extended past the test surface. Using the sharp edge of a razor blade, the cap was then pushed back flush with the wall. Modeling clay was then carefully applied to the seam between the wall and the cap, and feathered with the razor blade. This ensured a smooth surface with minimal disturbances.

### 2.4.1 Microphone calibration

The microphones were calibrated against a B&K type 4220 pistonphone. The pistonphone produced a known sound-pressure level (nominally 150 dB re 1  $\mu$ Pa) at a frequency of 250 Hz. Individual calibration curves provided by the manufacturer demonstrate that each microphone has a flat frequency response within  $\pm 1$  dB out

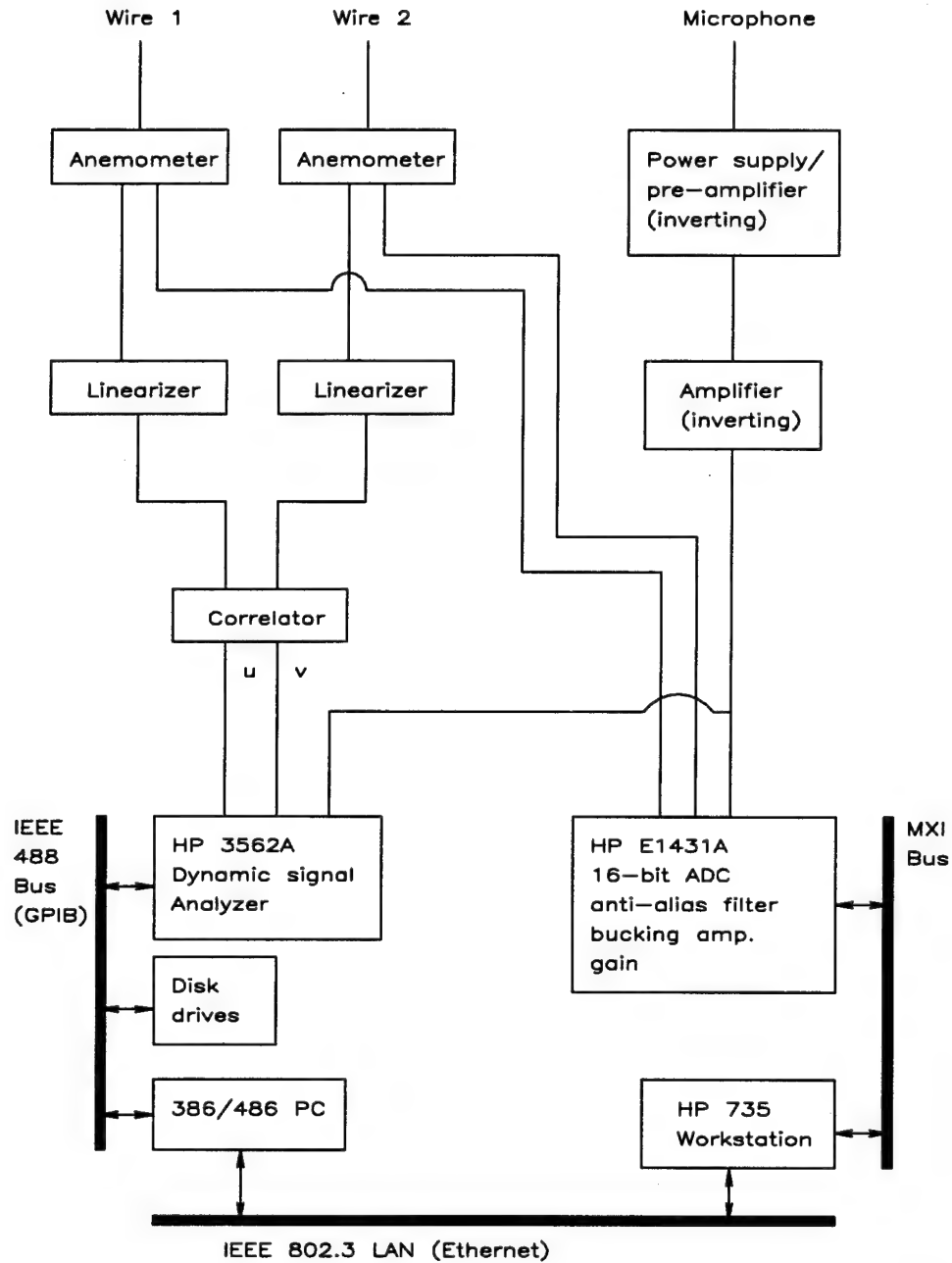


Figure 2.2: Schematic of instrumentation and data acquisition systems.

to 50 KHz. The microphone sensitivity was then calculated as

$$s = SPL/E_{rms} \quad (2.1)$$

where  $s$  is the microphone sensitivity in Pa/V,  $SPL$  is the pistonphone sound pressure level, and  $E_{rms}$  is the rms output voltage measured at the data acquisition system. For the disturbed TBL experiments with the Ithaco amplifiers set to 40 dB, a typical microphone sensitivity of 12.7 Pa/V was obtained.

## 2.4.2 Microphone resolution

To minimize spatial averaging of the fluctuating wall pressure, the microphone's standard protective screen was replaced with a pinhole cap. The cap had a 0.79-mm diameter hole drilled in the center. This resulted in nondimensional sensing diameters  $d^+ = du_\tau/\nu$  of 32 and 23 for the equilibrium and disturbed turbulent boundary layers, respectively. The pinhole cap and microphone assembly form a Helmholtz resonator, which limits the useful frequency range of the microphone data. Previous researchers [2.1, 2.4] have established that the Helmholtz resonance frequency for the current sensor configuration is approximately 25 KHz. This was confirmed in the present research as a small spike in the wall-pressure spectrum. As discussed in the Chapter 3, the Helmholtz frequency is well beyond both the energy-containing range of the wall pressure and the digital sampling Nyquist frequency of 16.3 KHz.

## 2.5 Hot-wire anemometers

Velocity measurements were obtained using a constant-temperature anemometry (CTA) system comprised of the following components:

- TSI Inc. type 1261 A-T1.5 miniature boundary-layer probe or type 1249 A-10 miniature "X" probe
- TSI 1155 probe support on a motorized traverse
- Dantec (formerly DISA) type 55M10 CTA standard bridges in type 55M01 main units
- Dantec type 55M25 linearizers
- TSI type 1015C correlator

The anemometer system is illustrated schematically in Figure 2.2.

The type 1261 A-T1.5 probe consisted of a single tungsten wire of length 1.52 mm,  $3.8 \mu\text{m}$  in diameter, with an active sensing length of 1.27 mm. The wire was oriented normal to the streamwise velocity in the  $z$ -direction. Curved wire supports allowed

the wire to be positioned close to a solid boundary. The type 1249 A-10 "X" probe consisted of two ceramic "wires" on which were deposited a platinum film. The wires were of length 1.27 mm and diameter 25  $\mu\text{m}$ , with active film sensing lengths of 0.51 mm. The wires were oriented in the x-y plane, at  $\pm 45$  deg to the x-axis. The two wires were separated in the z-direction by 1.0 mm. The probe incorporated a 90-deg elbow for making measurements close to the wall.

### 2.5.1 Hot-wire calibration

For digital measurements, the bridge outputs were input directly into the digital data acquisition system, which is described in Section 2.6.1. The single-wire voltages were converted to velocities in a conventional way [2.5, pp. 15-17], based on a form of King's law:

$$E^2 = A + BU^n \quad (2.2)$$

where  $E$  is the anemometer output voltage,  $U$  is the velocity in m/s, and  $A$ ,  $B$ , and  $n$  are constants. The exponent,  $n$ , was allowed to vary from 0.1 to 0.7 in increments of 0.01, and a least-squares method used to determine  $A$  and  $B$ . The value of  $n$  that resulted in the smallest standard error fixed the calibration. Eight voltage-velocity pairs were used for the calibration. The tunnel velocity was determined from the Pitot-static probe. Typical calibration data and the resulting fit are shown in Figure 2.3.

The X-film probe was calibrated according to the method of Camelio [2.6] as presented in Wilczynski [2.4]. The two velocity components,  $U$  and  $V$ , were represented by fourth-order, two-dimensional polynomials in the two wire voltages,  $E_1$  and  $E_2$ :

$$U = \sum_{i=0}^4 \sum_{j=0}^4 a_{ij} E_1^i E_2^j \quad (2.3)$$

$$V = \sum_{i=0}^4 \sum_{j=0}^4 b_{ij} E_1^i E_2^j \quad (2.4)$$

Calibration velocities  $U$  and  $V$  were obtained by rotating the probe to seven different angles,  $\phi$ , with respect to the tunnel velocity,  $Q$ , so that  $U = Q \cos \phi$  and  $V = Q \sin \phi$ . Seven different angles were used:  $\phi = -36, -18, -9, 0, 9, 18$ , and  $36$  deg. At each angle, data were recorded at eight tunnel speeds, resulting in a total of 56 calibration points. The coefficients  $a_{ij}$  and  $b_{ij}$  were then computed using a least-squares regression method. Typical data and the resulting calibration surfaces are shown in Figures 2.4 and 2.5.

More common methods of calibrating X-probes found in the literature involve fitting  $(Q, \phi)$  to  $(E_1, E_2)$ , then solving for  $U$  and  $V$ . Various curve fitting and table look-up implementations can be found. The present method, however, was felt to be a more direct approach, without sacrificing accuracy.

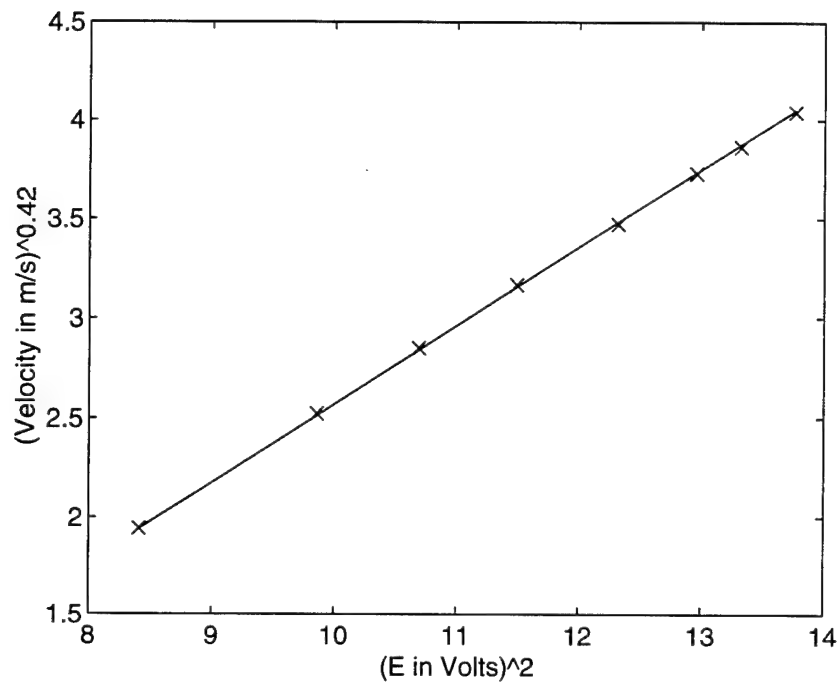


Figure 2.3: Sample hot wire calibration.

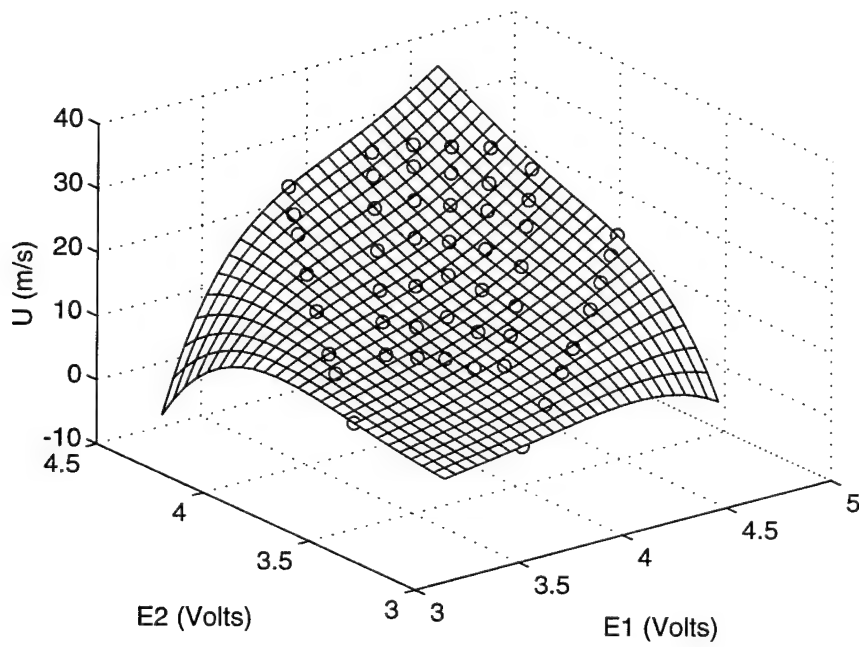


Figure 2.4: Sample X-wire U-velocity calibration.



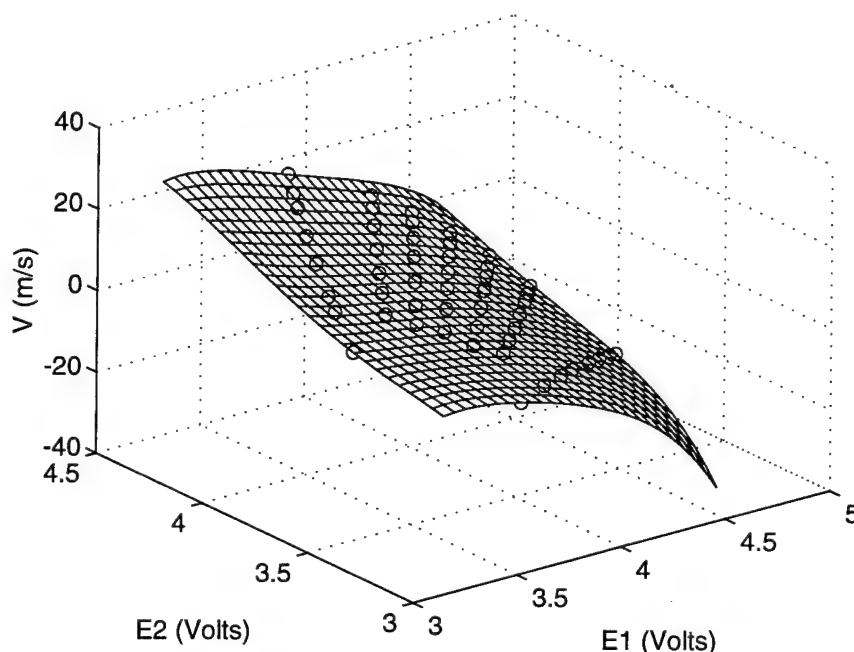


Figure 2.5: Sample X-wire V-velocity calibration.

The calibration methods outlined above assume that the flow being measured is isothermal and that the temperature remains constant. In the course of the experiments, changes of up to 3 deg C were observed between calibration and measurement. To account for these changes, a temperature compensation procedure was implemented as given in [2.5, pp. 194–198]:

$$E^2|_{T_{ref}} = E^2|_T \frac{T_w - T_{ref}}{T_w - T} \quad (2.5)$$

Here,  $E$  is the wire voltage,  $T$  is fluid temperature at the time of the measurement,  $T_w$  is the wire operating temperature, and  $T_{ref}$  is the reference temperature. The reference temperature was chosen to be the mean temperature observed over the course of collecting the calibration data. The correction was applied to the voltages prior to using them to compute calibration coefficients or velocities. This correction scheme is valid for temperature changes of a few degrees or less. For larger variations, more involved corrections must be made.

Spectral measurements (Section 2.6.2) require a voltage signal directly proportional to the velocity. For the single-wire data, the anemometer output was fed through the 55M25 linearizer before being input to the spectrum analyzer. The linearization was adjusted at flow speeds near the minimum and slightly above the maximum velocity measured. For the X-probe, the wire voltages were linearized corresponding to the flow components  $\pm 45$  deg to the x-direction. The linearized signals were then fed into the correlator, which added and subtracted them to pro-

vide signals proportional to  $U$  and  $V$ . The X-probe case is illustrated in Figure 2.2.

Solid boundaries in close proximity to a hot-wire probe can act as a heat sink, conducting heat away from the probe. This effect will appear as an increase in velocity, since more voltage is required to replace the lost heat. A survey of the literature on this effect can be found in [2.5]. For nonconducting walls, such as the formica covered plywood of the LNFF, corrections need not be made for measurements where  $y^+ = yu_\tau/\nu \geq 2.5$ , and then only for very low flow speeds. All measurements in this investigation were obtained at a sufficient distance from the wall and at a high enough flow speed such that corrections for wall conduction effects were not necessary.

## 2.5.2 Hot-wire resolution

The spatial resolution of the velocity measurements was limited by the active sensing length of the single-wire probe and by the separation distance of the X-probe. Expressed in wall units of  $l^+ = lu_\tau/\nu$ , the resolutions for the equilibrium TBL were 50 for the single wire and 41 for the X-probe. For the disturbed TBL, the resolutions were 26 and 29 wall units for the single and X-probes, respectively.

## 2.5.3 Probe displacement measurements

The hot-wire probe support was mounted on a three degree-of-freedom (3-DOF) traverse inside of the wind tunnel. The traverse could be controlled manually as well as remotely via stepper motors. In practice, the probe was positioned manually over microphone  $p_1$ , at approximately 1-mm downstream of the pinhole.

The probe was initially brought close to the wall while being observed through an Edmund Scientific 6-8 $\times$  close-focus telescope. The telescope was equipped with a combination radius/angle reticle and was mounted on a 3-DOF, micrometer-positioned platform manufactured by the Line Tool Company. The platform was placed on the top of the tunnel such that the telescope was located at the same  $x$ -location as the hot-wire probe, at  $y \approx 0$ , and sighted along the positive  $z$ -axis. From this shallow viewing angle, with the telescope focused on the wire support prongs, the reflection of the probe was clearly visible in the test wall. The probe could therefore be brought as close to the wall as possible without actually making contact.

Once positioned, the initial  $y$ -displacement could be determined with the telescope platform positioning micrometers by taking readings with the reticle cross hairs on the wire and then on the wall. This was repeated twice and the results averaged. Dust made the wall location clear midway between the probe image and its reflection. The accuracy of the micrometer readings was verified by sighting the telescope on a precision scale fixed to the tunnel wall with modeling clay. The position of the hot wire at subsequent measurement locations was monitored with

an Ono Sokki DG-357 digital gauge attached to the traverse assembly. Both the telescope micrometers and the potentiometer system had a resolution of 26  $\mu\text{m}$ .

## 2.6 Data acquisition and processing systems

Data acquired in this research fell into two categories: digital and spectral. This section will detail the two systems, which are illustrated in Figure 2.2.

### 2.6.1 Digital data system

Digital data were acquired on a system based on the VMEbus Extensions for Instrumentation (VXIbus or VXI) specification. The VXI system uses a mainframe chassis with slots to hold modular instruments on plug-in boards. The specific system was manufactured by the Hewlett Packard Company. An HP E1401A C-size mainframe provided the VXI backplane, cooling, power, and current requirements. Digitization was performed by an HP E1431A 25.6 KHz Eight Channel VXI Input Module. This module was chosen for its high sampling rates, built-in signal conditioning, and high resolution, 16-bit, analog-to-digital converter.

The module featured simultaneous sampling on up to eight differential input channels. Sampling rates were selectable in powers of two from 1 to 65536 Hz, with alias protection provided internally by analog and digital antialias filters. The internal digital filters used  $2.56\times$  oversampling, resulting in a maximum alias-protected input bandwidth of 25.6 KHz. System gains allowed input voltage ranges of 5 mV to 10 V peak and were selectable on an individual channel basis. In addition, bucking amplifiers provided dc offset compensation individually for each channel. The bucking amplifier subtracted a constant voltage from the input signal, allowing the remainder to be amplified and digitized, thus maximizing the resolution of the low-amplitude fluctuations. This feature was exploited in the velocity measurements, where a typical input consisted of mV-level fluctuations superimposed on a 4–5 V signal. Conventional high-pass filtering is not acceptable in this situation due to the nonlinear voltage-velocity relationship of the constant-temperature anemometer system.

The system was controlled by an HP model 735 workstation via Multi-system eXtension Interface bus (MXIbus), using an HP E1482B VXI-to-MXI interface module in the mainframe and an HP E1439I EISA/ISA-to-MXI interface card in the workstation. The MXIbus is a general-purpose, 32-bit multimaster system bus on a cable. It uses a hardware memory-mapped communication scheme to minimize software overhead for very high speed. Data were acquired from the E1431A direct to the HP 735 main memory. The maximum theoretical data rate for MXIbus is 20 Mbytes/s [2.7]. The use of MXI for system control allowed realtime acquisition of all eight channels of the E1431A sampled at 32768 samples/s without the need for

local memory modules in the VXI mainframe. A maximum of four channels was used simultaneously to acquire data from the two microphones and the two-component hot wire. The tunnel temperature and the hot-wire probe position were acquired and recorded manually.

The HP 735 was a general purpose Unix workstation. It was equipped with 64 Mbytes of RAM, an HP PA-RISC central processing unit clocked at 90 MHz, and approximately 6 Gbytes of hard disc storage. The software to control the VXI system was custom developed in-house [2.8]. It provided complete control of the E1431A setup and acted as the external trigger. The data were received into the HP 735 memory and then written to disc. One file was created per active channel. The raw data were stored in binary format and included the channel sample rate, digital count to voltage conversion factor, and dc offset in the record.

## 2.6.2 Spectral data system

Spectral data were acquired with an Hewlett Packard HP 3562A Dynamic Signal Analyzer. The HP 3562A is a two-channel, fast Fourier transform analyzer with internal antialias filters and a 100-KHz input bandwidth. The analyzer was used to compute auto spectra, cross spectra, phase response, and coherence functions.

A feature of the HP 3562A utilized in this study was its ability to compute spectral measurements in a logarithmic resolution mode. In this mode, the frequency span of interest was represented by 80 discrete frequencies per decade, logarithmically spaced. When plotted on a log-frequency axis, spectra computed in this mode had equal resolution in the lowest and the highest decades. This proved to be useful, since the turbulent flow fields of this study had significant spectral features spanning a frequency range of 10 Hz to approximately 20 KHz.

The analyzer was controlled by an IBM-compatible 486 personal computer equipped with an HP 82335 HP-IB (IEEE 488 or GPIB) interface card. Custom software was developed to initialize the analyzer, trigger the measurements, and write the results to external disc drives on the GPIB bus. As illustrated in Figure 2.2, the data were then available to the PC via the GPIB bus and to the HP 735 via Ethernet (IEEE 802.3) local area network. The measurements were made in the logarithmic resolution mode over a frequency span of 10 Hz to 100 KHz. The final results were the ensemble average of fifty individual spectra, using 50 percent overlap and the rms voltage as the basic amplitude unit.

## 2.7 Test conduct and data processing

This section describes the experimental procedures for collecting the raw data and the first-order processing done to create data bases needed for further analyses.

### 2.7.1 Test conduct

Data were collected for two different flows: an ETBL and a DTBL. For each of these flows, a single-wire survey and several X-wire surveys were performed. For each single wire survey, the streamwise velocity  $U$ , and the wall pressure at two  $x$ -locations  $p_1$  and  $p_2$ , were measured at each of 22 or 23  $y$ -locations within and outside of the boundary layer. For each X-wire survey, the wall-normal component of velocity  $V$  was measured as well. Several X-wire surveys were required to obtain the desired cross spectral data pairs:  $U-V$ ,  $U-p_1$ , and  $V-p_1$ .

The initial task was the calibration of the microphones. Each microphone was coupled to the pistonphone using a plastic coupler, and its output recorded on the VXI system in the same channel to be used for the survey. The rms voltage computed from the calibration data was checked against a voltmeter for consistency. The microphones were then installed in the test surface. Next, the Pitot-static pressure transducer was adjusted for zero, full scale, and sensitivity according to the manufacturer's procedures.

At this point, the single- or X-wire probe was installed in the traverse and the anemometer bridge was set up for a 70 percent overheat ratio. The tunnel was then set to a speed approximately equal to  $U_e$ , and the bridge balanced for frequency response using the internal square wave circuitry. The useful frequency ranges for both types of probe were found to be at least 47.6 KHz. Analog linearization of the anemometer was then checked at two tunnel speeds:  $\approx 0.2U_e$  and  $1.0U_e$ . Following linearization, the hot-wire calibration was performed. If the flow-disturbance ramp was installed, the hot-wire probe was traversed well upstream of the ramp where the flow angles were undisturbed. For the X-wire probe, the final calibration angle was always 0 deg so that the probe was not disturbed again prior to the survey.

With the preparations complete, the data collection was begun. The probe was positioned close to the wall as described in Section 2.5.3, and the initial displacement recorded. The tunnel was then started. Flow speeds were set according to motor speed, thus some variation in the actual velocities between surveys was observed. The spectral analyzer was then triggered to ensemble average 50 individual spectra. Concurrent with the spectral measurements, the digital system was triggered to record two data sets:

1. Statistics data, consisting of 140 s of the anemometer channel(s) at 500 samples/s per channel
2. Time series data, consisting of 10 s of all channels at 32768 samples/s per channel.

Both the digital and the spectral systems required approximately 2.5 min to complete their measurements. Once both systems were finished, the traverse was moved outward and data collected at the new location. This measure-move-measure process was repeated for 22 or 23 locations throughout the boundary layer. When the

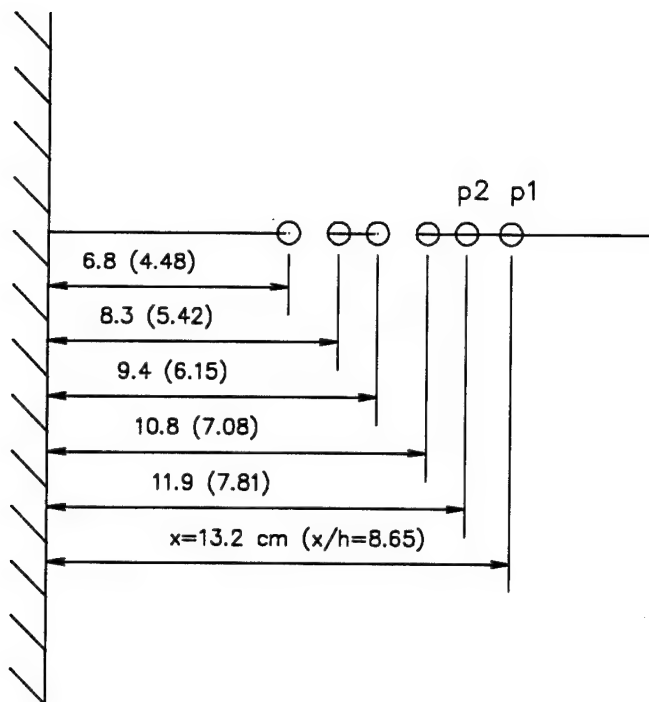


Figure 2.6: Pressure measurement locations relative to the aft-facing step.

survey was complete, the probe was returned to the near-wall position for collection of the remaining cross-spectral combinations.

The  $U$  power spectra and  $U$ - $p_1$  cross spectra obtained with the single-wire probe were compared with those obtained with the X-probe for consistency. Differences in the power spectra were less than 1 dB over the entire 100-KHz frequency span, with a similar agreement in the coherence data. Therefore, the  $U$ - $p_1$  cross spectra were obtained with the single-wire probe, since this probe could be positioned much closer to the wall than the X-probe. Cross-spectral data were also obtained for the  $p_1$ - $p_2$  input pair with the hot-wire probe at its closest and farthest measurement locations from the wall.

Figure 2.6 shows the locations relative to the aft-facing step where pressure measurements were made. The stations labeled  $p_1$  and  $p_2$  were the primary stations, where pressure measurements in conjunction with hot-wire anemometry were simultaneously obtained. Wall-pressure measurements were obtained at these other stations to locate the flow reattachment point and to separate the spectral signature of the free shear layer from that of the developing TBL. These wall pressure results upstream of the primary location are presented in Appendix A.

## 2.7.2 Data reduction and filtering

In addition to controlling the VXI data system, the HP workstation performed engineering unit conversions and all subsequent analyses of the digitized data. All computations and graphics were performed using MATLAB<sup>TM</sup> scientific software running under the HP-UX operating system. The raw binary statistics and time series data were read into MATLAB and converted to Pa or m/s according to Sections 2.4.1 and 2.5.1. The data were then digitally filtered to remove unwanted electrical and acoustical noise. This was done using a 5th-order high-pass Butterworth filter with a cutoff frequency of 100 Hz. The filter was applied both forwards and backwards to eliminate phase lags. To account for end effects, 500 points were deleted from both ends of the filtered record. The data were then stored in MATLAB binary format for further processing.

The MATLAB file format proved convenient for two reasons. First, the binary format is efficient. One channel of filtered data occupied 2.5 Mbytes of disk space. One complete survey therefore required  $2.5 \text{ MBytes} \times 4 \text{ channels} \times 22 \text{ stations} = 220 \text{ MBytes}$  of storage, excluding raw data. Second, the file header contains a machine signature, allowing the program to convert data written by a different platform. This proved convenient in transmitting results between the HP 735 and the 486 PC. The format is completely documented so that it can be read without the MATLAB software using FORTRAN or C routines.

As detailed in Section 2.6.2, the spectral data were acquired by the spectrum analyzer and stored on an external GPIB disk drive. The 486 PC retrieved the data and converted it from HP 3562A binary format into MATLAB format using Hewlett Packard Standard Data Format utility software. The data could then be processed on the PC running MATLAB under Microsoft Windows or transferred to the HP 735 via Ethernet.

## References

- [2.1] T. M. Farabee. An experimental investigation of wall pressure fluctuations beneath non-equilibrium turbulent flows. Technical Report DTNSRDC-86/047, David Taylor Naval Ship Research and Development Center, Bethesda, Maryland 20084-5000, 1986.
- [2.2] H. Helal, M. Casarella, and T. Farabee. An application of noise cancellation techniques to the measurement of wall pressure fluctuations in a wind tunnel. In Farabee, Hansen, and Keltie, editors, *Flow-Induced Noise Due to Laminar-Turbulence Transition Process*, number NCA 5, pages 49–59. ASME, 1989.
- [2.3] T. M. Farabee and M. J. Casarella. Spectral features of wall pressure fluctuations beneath turbulent boundary layers. *Phys. Fluids A*, 3(10):2410–2420, 1991.

- [2.4] V. Wilczynski. *Organized Turbulent Structures and Their Induced Wall Pressure Fluctuations*. PhD thesis, The Catholic University of America, 1992.
- [2.5] J. Foss, C. Tropea, and R. Menon. Principles of thermal anemometry and applications in fluid mechanics. Short Course, Michigan State University, East Lansing, MI, 1991.
- [2.6] F. J. Camelio. Variation of wall shear stress and Reynolds stress over a flat plate downstream of a boundary layer manipulator. Master's thesis, Massachusetts Institute of Technology, 1990.
- [2.7] National Instruments Corp. *IEEE 488 and VXIbus Control, Data Acquisition, and Analysis Catalog*, 1994.
- [2.8] P. B. Penafiel. VXI driver for the HP-9000/735 workstation using the HP-E1489I MXIbus controller interface. Technical report, Dept. of Mech. Engineering, The Catholic University of America, Washington, D.C. 20064, 1994.



## Chapter 3

### Properties of equilibrium and disturbed flows

#### 3.1 Introduction

This chapter presents the first-order analysis of the equilibrium and disturbed flows. The mean features of each flow are presented, followed by single-point statistics and spectra. Peak-event detection results are then presented on wall pressure and Reynolds stress. For each perspective, the equilibrium and disturbed cases are compared and contrasted for insight into the physics of turbulence.

#### 3.2 Mean features

The mean features of the two flows studied are presented in Table 3.1, which also summarizes the measurement resolutions. For each flow, the shear velocity,  $u_\tau$ , was chosen as the value which best fit the profile to the log-law relation given by Clauser [3.1]:

$$U/u_\tau = 2.44 \ln y^+ + 4.9 \quad (3.1)$$

where  $y^+ = yu_\tau/\nu$ . This assumes that the standard logarithmic law applies near the surface of the disturbed flow, which was shown to be valid in [3.2]. The boundary layer thickness,  $\delta$ , was defined as the location where  $U = 0.99U_e$ . The displacement thickness,  $\delta^*$ , and the momentum thickness,  $\theta$ , were evaluated using trapezoidal rule integrations of the mean velocity profiles. Calculated skin friction coefficients,  $C_f$ , were obtained from the Ludwig-Tillman formula:

$$C_f = 0.246 Re_\theta^{-0.268} 10^{-0.678H} \quad (3.2)$$

where the momentum thickness Reynolds number  $Re_\theta = \theta U_e/\nu$  and  $H = \delta^*/\theta$  is the conventional shape factor. "Measured" friction coefficients were obtained from the definition of the shear velocity as:

$$C_f = 2 \left( \frac{u_\tau}{U_e} \right)^2 \quad (3.3)$$

Table 3.1: Nominal boundary-layer properties and measurement resolutions.

	Equilibrium TBL		Disturbed TBL	
	Single Wire	X-wire	Single wire	X-wire
$U_e$	14.79 m/s	16.13 m/s	13.74 m/s	16.18 m/s
$u_\tau$	0.60 m/s	0.64 m/s	0.32 m/s	0.45 m/s
$u_\tau/U_e$	0.040	0.040	0.023	0.028
$\delta$	2.72 cm	2.95 cm	4.05 cm	4.30 cm
$\delta^*$	0.43 cm	0.46 cm	0.97 cm	0.89 cm
$\delta^+$	1064	1202	836	1255
$Re_\theta$	3045	3358	4599	5397
$H$	1.39	1.42	1.85	1.74
$G$	6.93	7.41	19.72	15.38
$C_f$ (calculated)	0.00329	0.00304	0.001431	0.001627
$C_f$ (measured)	0.00324	0.00318	0.00108	0.00153
$l_\nu = \nu/u_\tau$	25.6 $\mu\text{m}$	24.6 $\mu\text{m}$	48.4 $\mu\text{m}$	34.2 $\mu\text{m}$
$t_\nu = \nu/u_\tau^2$	42.9 $\mu\text{s}$	38.2 $\mu\text{s}$	151.3 $\mu\text{s}$	76.5 $\mu\text{s}$
$l_{wire}$	1.27 mm	1.0 mm	1.27 mm	1.0 mm
	(50 $l_\nu$ )	(41 $l_\nu$ )	(26 $l_\nu$ )	(29 $l_\nu$ )
$d_{mic}$	0.79 mm	0.79 mm	0.79 mm	0.79 mm
	(31 $l_\nu$ )	(32 $l_\nu$ )	(16 $l_\nu$ )	(23 $l_\nu$ )
$\Delta t_s$	30.5 $\mu\text{s}$	30.5 $\mu\text{s}$	30.5 $\mu\text{s}$	30.5 $\mu\text{s}$
	(0.71 $t_\nu$ )	(0.80 $t_\nu$ )	(0.20 $t_\nu$ )	(0.40 $t_\nu$ )

Figure 3.1 shows the mean streamwise velocity profiles of the two flows. The equilibrium layer is seen to exhibit the classic full profile, while the disturbed layer has a significantly retarded section over most of the layer. Alternatively, the disturbed layer can be viewed as having an accelerated or energized outer layer. This is emphasized by Figure 3.2, where the profiles are normalized by wall variables. Both the single wire and the X-wire surveys are shown in this figure, with the single wire surveys approaching much closer to the wall. The low values of skin friction result in highly exaggerated wake regions for the disturbed flows. The difference in wake strengths between the disturbed flow single and X-wire runs is due to the slightly different freestream conditions resulting in differences in the location of shear layer reattachment. This also accounts for the dip below the law of the wall seen in the disturbed flow X-wire survey. The higher value of  $U_e$  for this run places reattachment closer to the measurement station than for the single-wire run. Therefore, the flow is exhibiting the constant mixing length character of the free shear layer, having not yet relaxed to a mixing length proportional to distance from the wall as assumed in the law of the wall [3.2, 3.3]. Figure 3.3 shows the mean wall-normal velocity

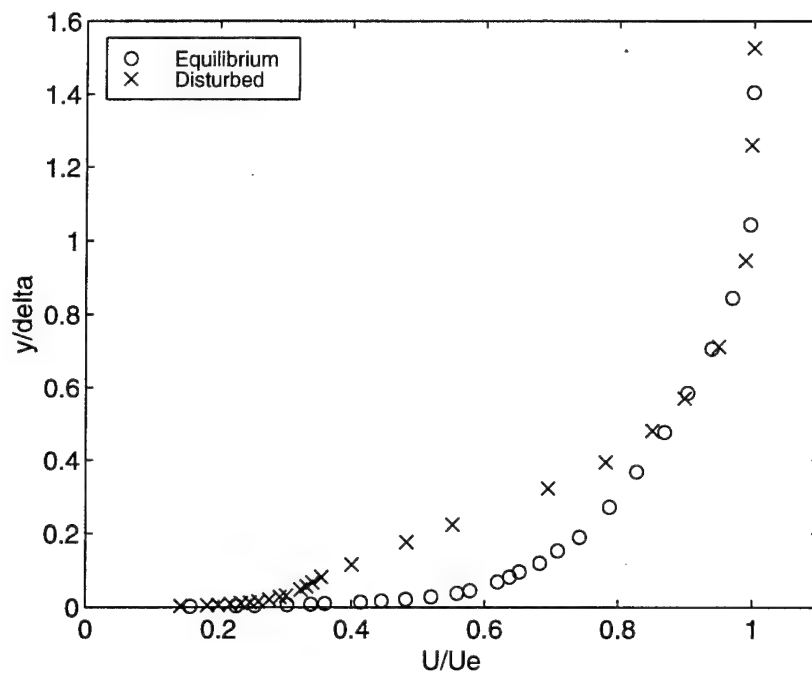


Figure 3.1: Mean streamwise velocity profiles from single wire surveys.

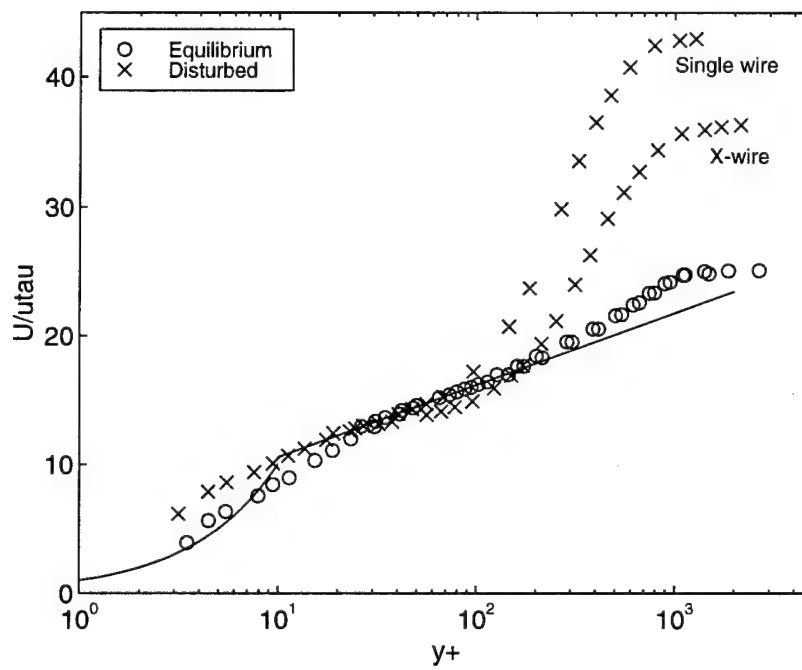


Figure 3.2: Mean streamwise velocity profiles normalized by wall variables.

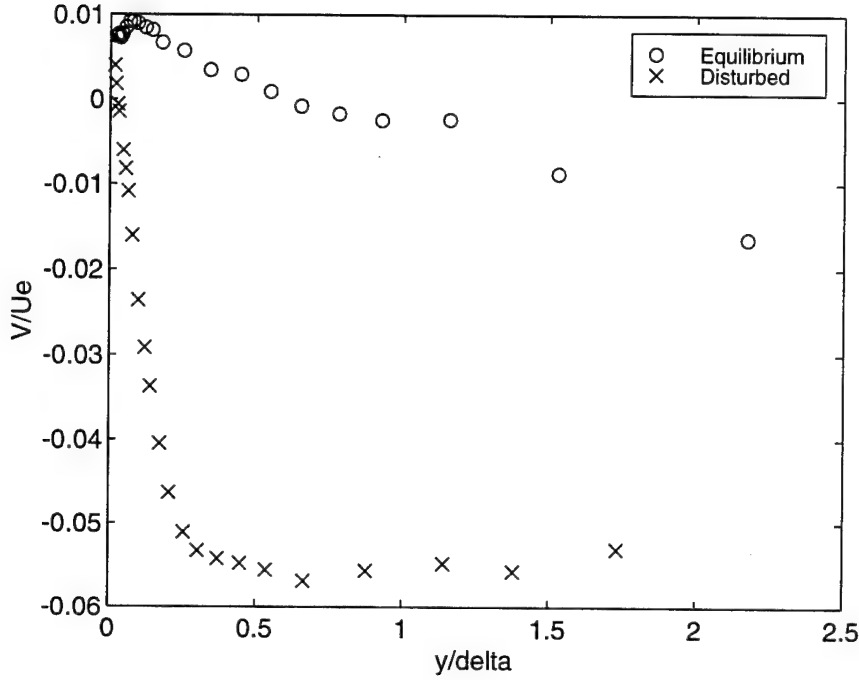


Figure 3.3: Mean wall-normal velocity profiles.

profiles. As expected, the disturbed case is exhibiting significant inflow over most of the layer until constrained by the wall. This inflow manifests itself as higher values of fluctuating wall pressure, as will be seen in Section 3.3.3.

### 3.3 Single-point statistics and spectra

In addition to the mean values presented above, higher-order statistics were computed from the statistics data sets for both components of velocity, the  $uv$  product, and the wall pressures. The higher-order statistics were the root-mean-square or rms, the skewness, and the kurtosis or flatness. These quantities are (the square root of) the second, the third, and the fourth central moments, respectively, of a random variable or signal. They describe the probability density function; i.e., how the fluctuations are distributed around an average value. Using  $u$  for the zero-mean, random variable, the statistics are given by:

$$\text{rms} = \left( \frac{1}{N} \sum_{i=1}^N u_i^2 \right)^{1/2} \quad (3.4)$$

$$\text{skewness} = \frac{1}{N} \sum_{i=1}^N \left( \frac{u_i}{u_{\text{rms}}} \right)^3 \quad (3.5)$$

$$\text{kurtosis} = \frac{1}{N} \sum_{i=1}^N \left( \frac{u_i}{u_{rms}} \right)^4 \quad (3.6)$$

where  $N$  is the number of samples. The rms value has the dimensions of the variable of interest and is used to normalize the skewness and kurtosis. It is a measure of the variation from the mean value. The skewness relates to the symmetry of the probability density function; i.e., it is an indication of whether a variable favors positive or negative excursions from the mean. The kurtosis is indicative of how "spiky" the signal is. A signal with a high kurtosis takes on values far away from the mean relatively more often than a signal with a low kurtosis.

Auto or power spectra and cross spectra were also obtained for  $u$ ,  $v$ ,  $p_1$ , and  $p_2$ . The  $u$  power spectrum is given by  $\Phi_u(\omega) = \mathcal{F}_u(\omega)\mathcal{F}_u^*(\omega)$ , where

$$\mathcal{F}_u(\omega) = \frac{1}{2\pi} \int u(t)e^{-i\omega t} dt \quad (3.7)$$

is the Fourier transform of the signal  $u$ ,  $\mathcal{F}^*$  is its complex conjugate,  $\omega$  is the frequency, and  $t$  is the time. Spectra are decompositions of a signal into waves of different periods or wavelengths. The value of the spectrum at a given frequency is the mean energy in that wave. As outlined in Tennekes and Lumley [3.4], the spectrum is indicative of the way in which waves, or eddies, of different sizes exchange energy with each other.

The spectra as presented above are frequency spectra where a function of time is mapped into the frequency domain. If the signals were measured as a function of space at a fixed time, the mapping would be from the spatial domain into the wavenumber domain. The transformation between frequency and wavenumber spectra can be made by assuming Taylor's hypothesis,  $k_1 = \omega/U_c$ , which gives  $\Phi(k_1, y) = U_c \Phi(\omega, y)$ . Here,  $k_1$  is the streamwise component of the wavenumber vector and  $U_c$  is the convection velocity, taken to be constant and equal to the local mean velocity,  $U(y)$ . The wavenumber has dimensions of  $\text{length}^{-1}$ .

Compared to mean measurements, higher-order statistics are particularly sensitive to probe resolution. Blackwelder and Haritonidis [3.5], using hot wires to detect the burst frequency in an equilibrium TBL, found that only sensors having a spatial scale less than  $20l_v$  were free from spatial averaging effects. Bandyopadhyay and Gad-el-Hak [3.6] have recently reviewed the literature on turbulent boundary-layer flows, concentrating on Reynolds number effects. They argue that the velocity probe resolution expressed in wall units " $l^+$  should not be much larger than 5, where  $l$  is the probe length." As given in Table 3.1, the hot-wire probe resolutions for this study were in the range 20–50 wall units. As will be seen in the following sections, this is small enough to resolve a significant portion of the small-scale structure and events that are the focus of the investigation, at least outside of the inner layer.

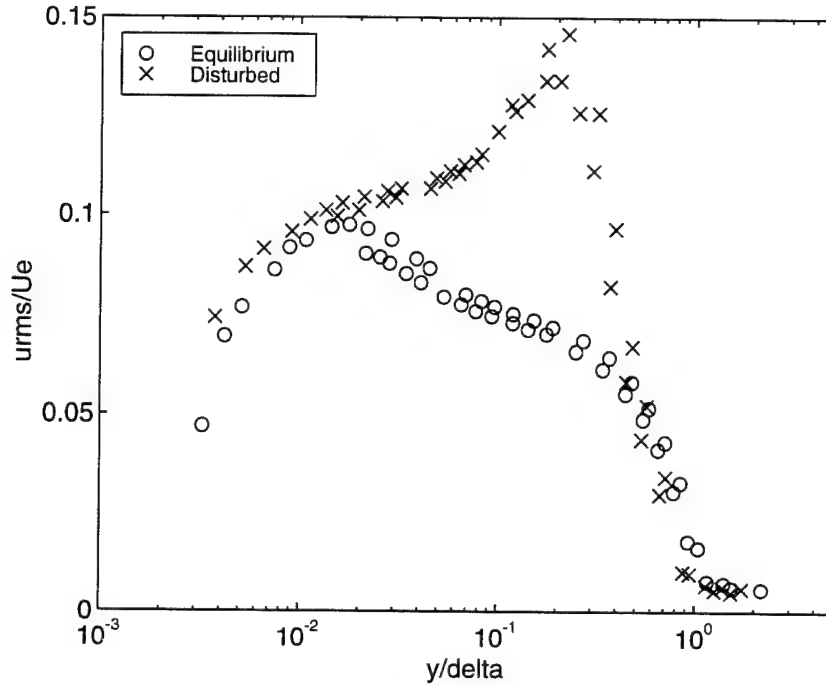


Figure 3.4: Streamwise turbulence intensity profiles.

### 3.3.1 Velocity statistics

Figures 3.4 and 3.5 show the rms streamwise and wall-normal velocity fluctuations, respectively. Outer-layer scaling is used since the disturbed flow perturbations are large scale, located outside of the buffer layer. Again, differences between the single and X-wire runs are attributable to the slight differences in edge velocities.

In Figure 3.4, the peak in the rms profile of the equilibrium boundary layer corresponds to  $u_{rms}/u_\tau = 2.42$  at  $y^+ = 18.9$ , in agreement with the criteria of Hussain. This compares with a peak value of  $u_{rms}/u_\tau \approx 2.7$  as compiled by Bandyopadhyay and Gad-el-Hak [3.6] from other investigations where  $l^+ < 7$ . The probe does indeed appear to resolve the significant small-scale motions. The disturbed flow shows  $u_{rms}$  and  $v_{rms}$  behavior similar to the equilibrium flow in the inner layer and at the boundary layer edge, but also shows a higher peak in turbulence intensity at  $y/\delta \approx 0.2$ . This *disturbance layer* is the remnants of the free shear layer that formed at the step and contacted the surface at the point of flow reattachment. It moves away from the wall as the flow progresses downstream, as demonstrated in the work of Farabee [3.7].

The  $u$  and  $v$  skewness profiles are shown in Figures 3.6 and 3.7. Bandyopadhyay and Gad-el-Hak [3.6, p. 62] point out that

... the third and all higher odd-number moments retain the sign information and thus contain valuable statistical information related to the co-

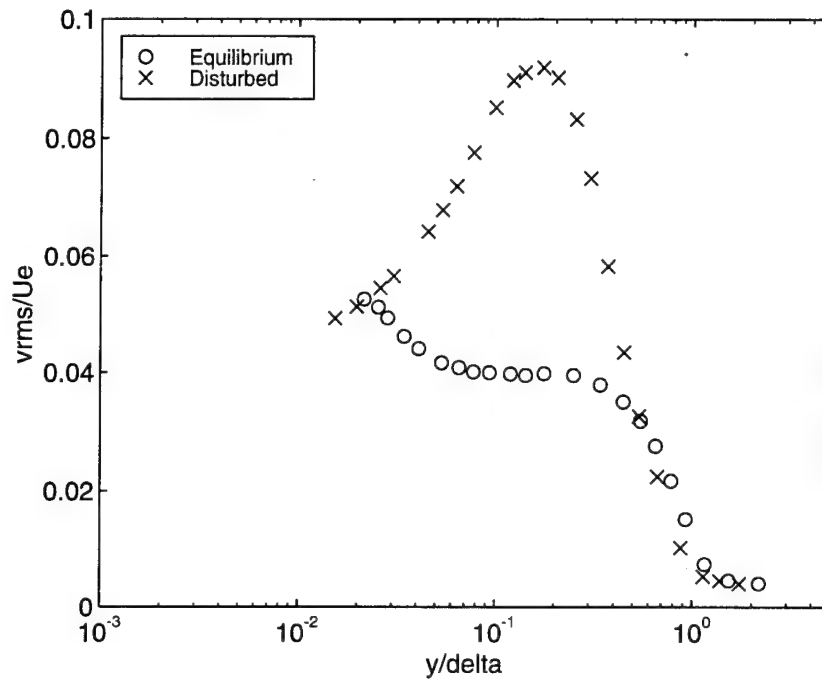


Figure 3.5: Wall-normal turbulence intensity profiles.

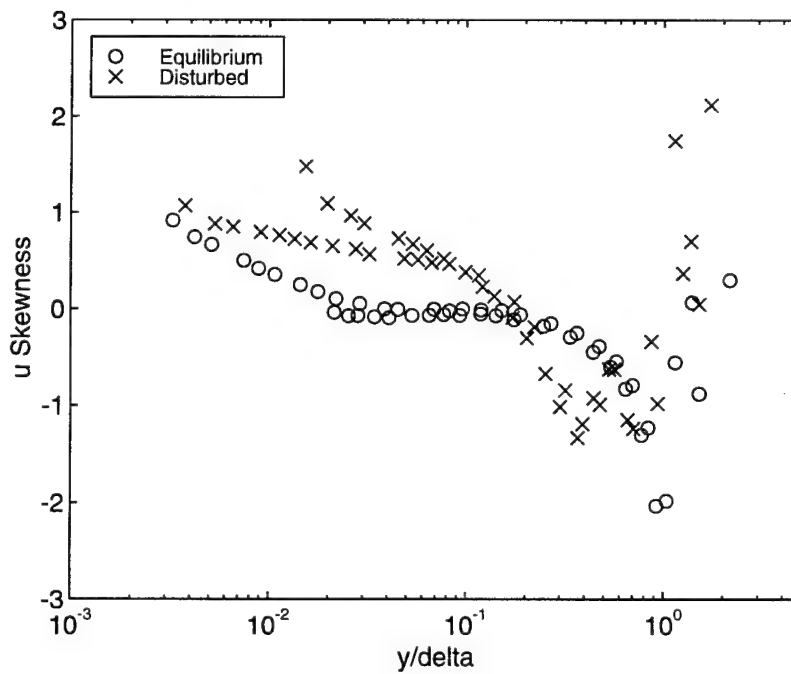


Figure 3.6: Profiles of the skewness factor of the streamwise velocity fluctuations.

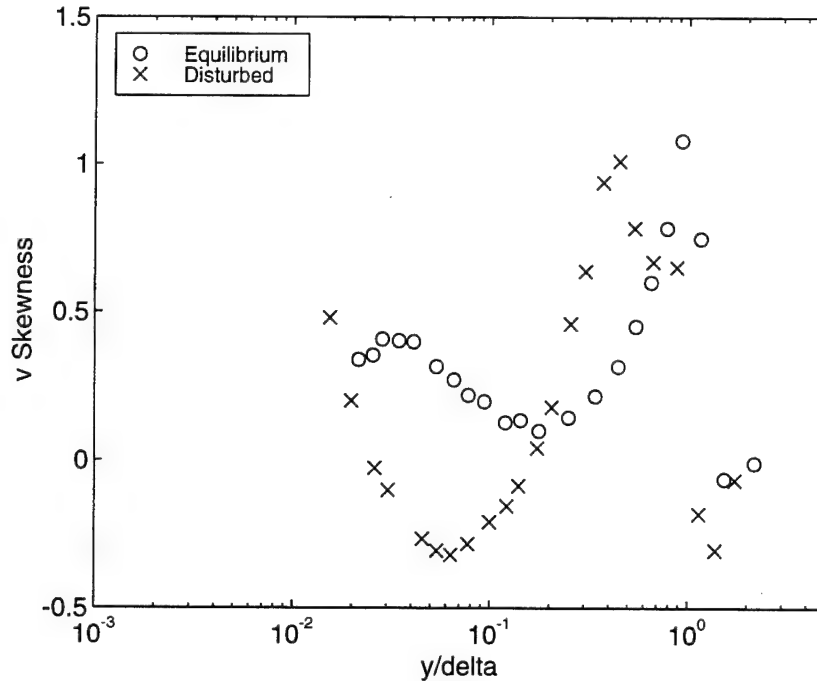


Figure 3.7: Profiles of the skewness factor of the wall-normal velocity fluctuations.

herent structures. The skewness of a turbulence quantity can be thought of as representing the flux of a stress that is directly attributable to coherent structures. For example,  $\overline{u^3}$  is the streamwise flux of the streamwise turbulence kinetic energy  $\overline{u^2}$ , ...

The  $u$  skewness of the equilibrium flow is positive near the wall. This indicates acceleration-dominated velocity fluctuations consistent with the arrival of high-speed fluid from regions away from the wall (sweep events). In the log-law region, the equilibrium flow  $u$  skewness is zero changing to negative farther away while the  $v$  skewness remains positive. This indicates a change to deceleration-dominated (ejection) events with an outward transport of wall-normal turbulence kinetic energy. For the disturbed flow, the  $u$  skewness remains positive over the log-law region changing sign at approximately the same location as the equilibrium case. The disturbed flow  $v$  skewness, however, evolves from positive at the edge of the sublayer to negative over the log-law region to positive again in the outer layer. This shows a net transport of wall-normal turbulence kinetic energy away from, towards, and away from the wall in the three regions. The skewness behavior for both flows is erratic in the turbulent-nonturbulent interface region at the edge of the boundary layer.

Kurtosis profiles of the  $u$  and  $v$  velocities are shown in Figures 3.8 and 3.9. Unlike the skewness, it is always positive, so no structural information can be deduced. The kurtosis is seen to be approximately 3 in the overlap region, the same as a



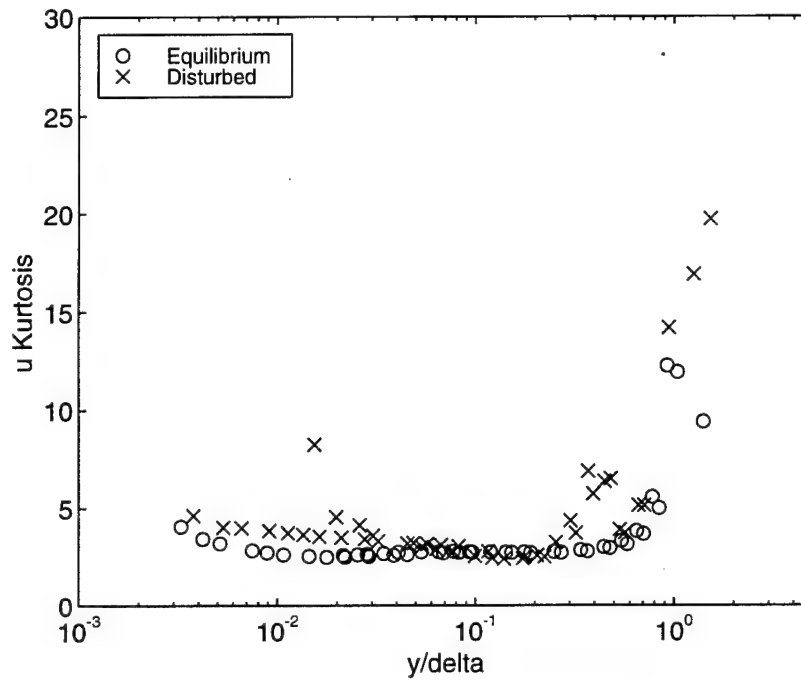


Figure 3.8: Profiles of the kurtosis factor of the streamwise velocity fluctuations.

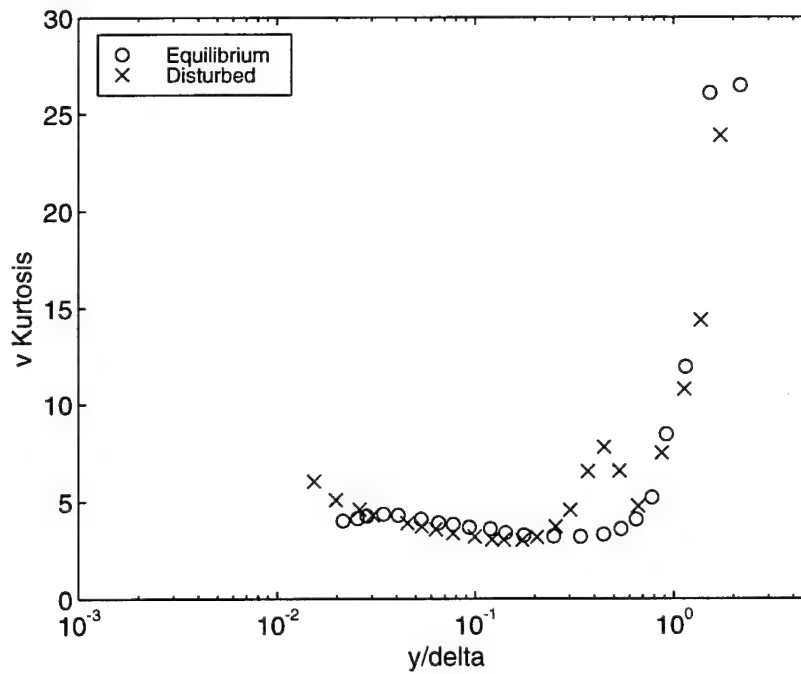


Figure 3.9: Profiles of the kurtosis factor of the wall-normal velocity fluctuations.

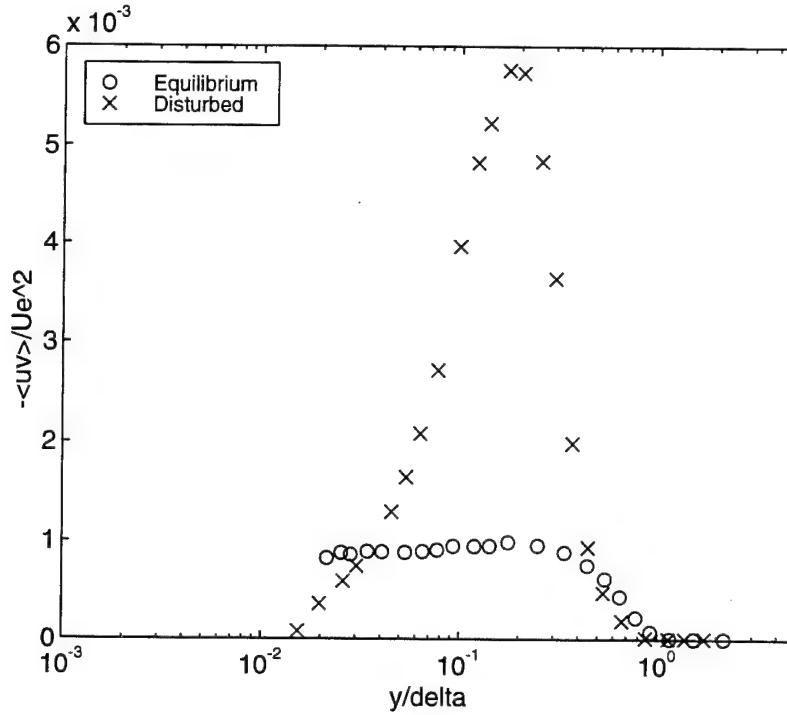


Figure 3.10: Reynolds stress profiles.

Gaussian signal. The kurtosis increases to large values at the boundary layer edge, and is seen to be increasing as the wall is approached, indicating that the turbulence is intermittent in both places.

The Reynolds stress profiles, normalized by the square of the edge velocity, are shown in Figure 3.10. The disturbed flow shows a peak in Reynolds stress at the same location as the peaks in  $u_{rms}$  and  $v_{rms}$ , again highlighting the added energy in the outer-layer regions. However, the Reynolds stress near the wall is much reduced from that of the equilibrium layer, indicating that the inner layer is either still developing or is contaminated by outer-layer structures. Figure 3.11 shows the same profiles normalized by  $(u_{rms}v_{rms})$ . Similar observations can be made from this figure.

### 3.3.2 Velocity power spectra

Power spectra of the velocity components will be considered next. Since the rms can be obtained from  $(\int \Phi(\omega) d\omega)^{1/2}$ , the spectral levels follow the trends of the rms fluctuations shown in Figures 3.4 and 3.5; i.e., they increase with increasing  $y$  up to some point and then decrease. For clarity, the spectra inside and outside of the location of the peak rms level will be shown separately, and for selected  $y$ -locations only.

The  $u$  power spectra are shown in Figures 3.12 and 3.13. From both figures, it

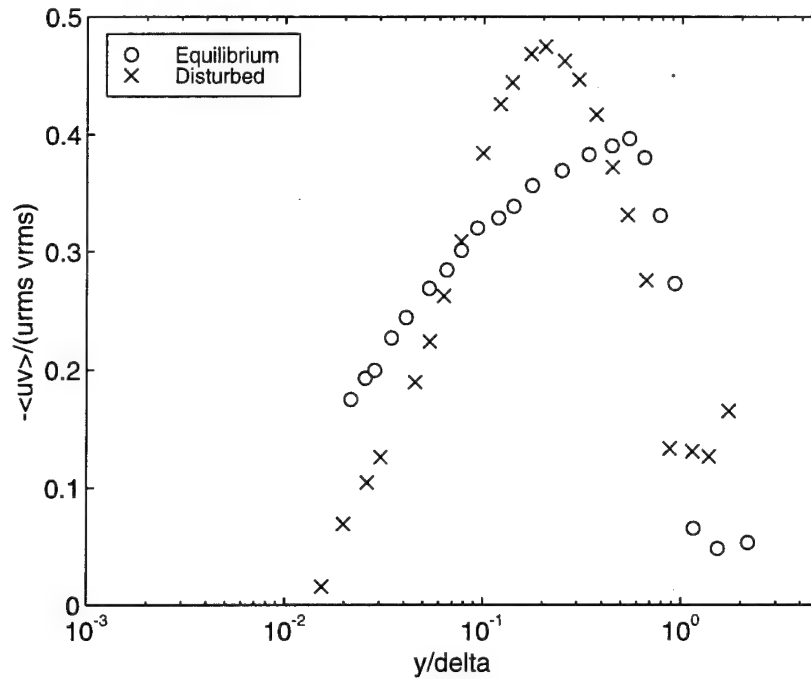
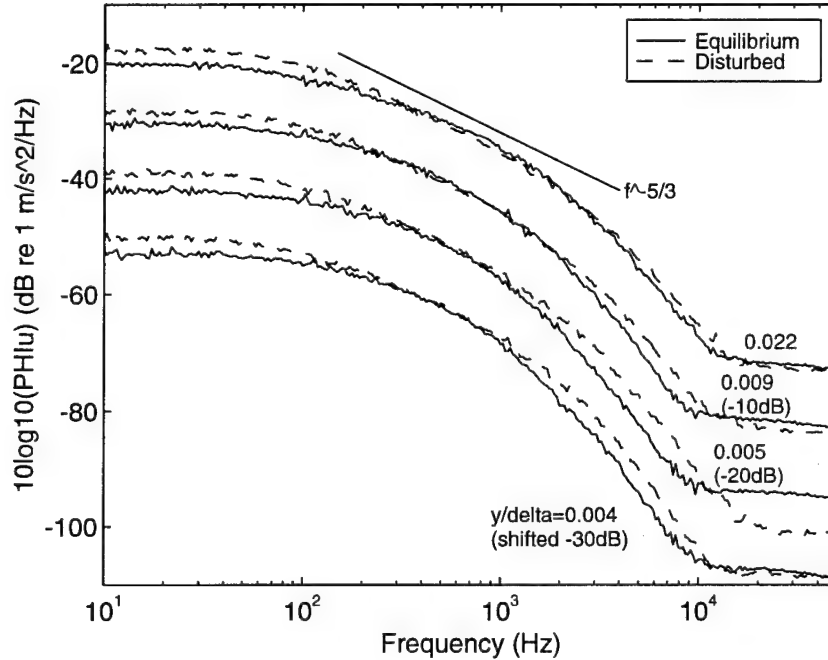


Figure 3.11: Profiles of turbulence stress correlation coefficient.

Figure 3.12: Streamwise velocity spectra inside of the location of peak equilibrium  $u_{rms}$ .

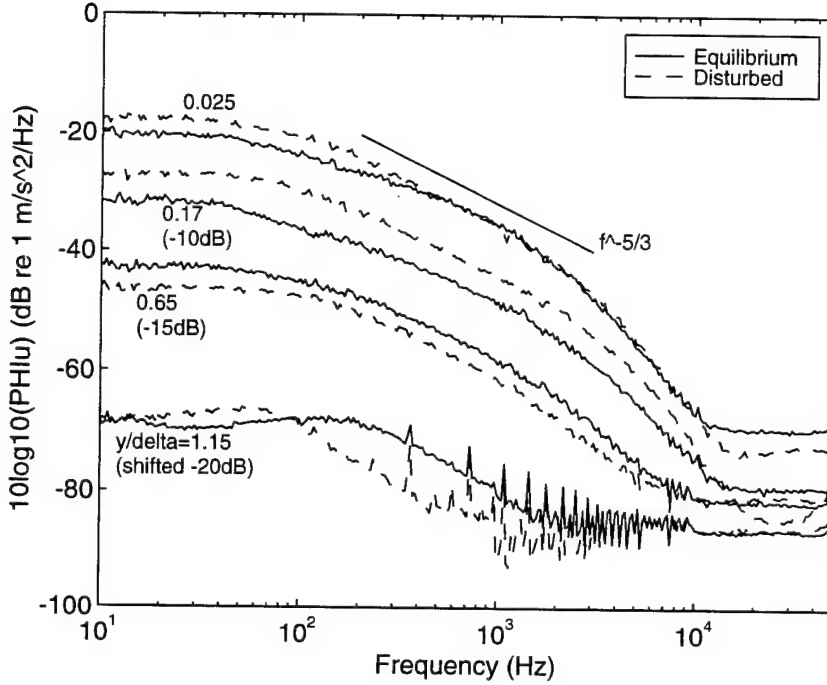


Figure 3.13: Streamwise velocity spectra outside of the location of peak equilibrium  $u_{rms}$ .

is apparent that inside  $y/\delta \approx 1$ , the spectra are broadband, with a high-frequency rolloff that is completed by 10 KHz. For  $y > \delta$ , the spectra become band limited with a peak in the neighborhood of 200 Hz. The band-limited behavior is the result of irrotational motion in the freestream induced by the turbulent boundary layer. This statement is supported by the  $u$ - $v$  cross spectral data of the present investigation as well as that of Wilczynski [3.8].

Careful examination of Figure 3.12 reveals that the spectral levels, though very similar, are increasing slightly through  $y/\delta = 0.022$ . Note that the three lower sets of curves have been shifted down by 10, 20, and 30 dB, respectively, for clarity. The disturbed flow low- and high-frequency components are increased relative to the equilibrium flow. Also, a linear midfrequency region is perceptible in the disturbed flow spectra for  $y/\delta \geq 0.005$ . The extent of the linear range grows with increasing  $y$ . A line of  $-5/3$  slope is shown for comparison. Such scaling is also found in other wake flows, such as the axisymmetric jet studied by Champagne [3.9]. Equilibrium boundary layers also exhibit this behavior in the frequency range bridging the high and low wavenumber spectra. This is known as the "inertial subrange", the extent of which is dependent on the turbulence Reynolds number [3.4]. It was not apparent in the equilibrium data of this investigation because the turbulence Reynolds number is not high enough.

Continuing across the boundary layer in Figure 3.13, the equilibrium layer spec-

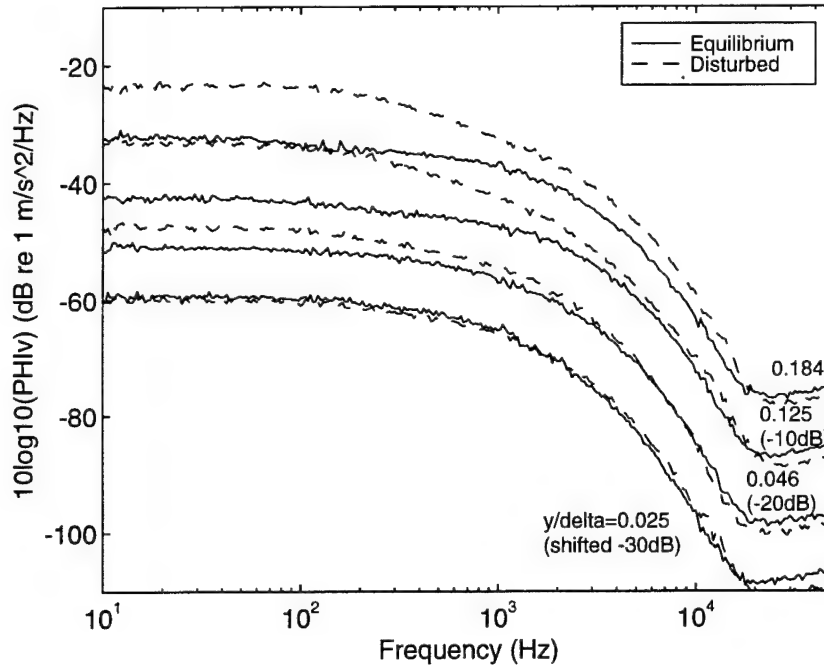


Figure 3.14: Selected wall-normal velocity spectra inside of the location of peak disturbed  $v_{rms}$ .

tral levels are seen to peak at  $y/\delta = 0.022$  to  $0.025$ , consistent with Figure 3.4. As in Figure 3.12, the lower curve sets have been shifted down by 10, 15, and 20 dB, respectively. From  $y/\delta = 0.025$  to  $0.17$ , the equilibrium levels decrease slowly. The range of  $f^{-5/3}$  scaling in the disturbed flow continues to increase, covering a maximum frequency range of  $200 < f < 2000$  Hz at  $y/\delta = 0.17$ . This coincides with the peak in the disturbed flow turbulence intensities, confirming that the disturbance layer is the source of the  $f^{-5/3}$  scaling.

The  $v$  spectra of Figures 3.14 and 3.15 show behavior similar to the  $u$  spectra. At the closest measurement locations, the equilibrium and disturbed spectra are very similar, with a wider low-frequency flat section and steeper rolloff than the corresponding  $u$  spectra. Moving away from the wall, the disturbed  $v$  spectral levels increase relative to the equilibrium case because of the disturbance layer. Again, the peak disturbed flow spectral levels correspond in location to the peak in  $v_{rms}$ . However,  $f^{-5/3}$  scaling is not apparent.

The band-limited character is also more prevalent, occurring closer to the wall than for the  $u$  spectra. The disturbed flow shows a peak at  $f \approx 150$  Hz at  $y/\delta = 0.35$ . As  $y$  increases further, the peak becomes more pronounced and moves to lower frequencies. This behavior was observed in the step flow experiments of Farabee [3.7] at multiple downstream locations. He suggested that the shift to lower frequencies in the disturbed flow spectra can be explained by considering structures that have

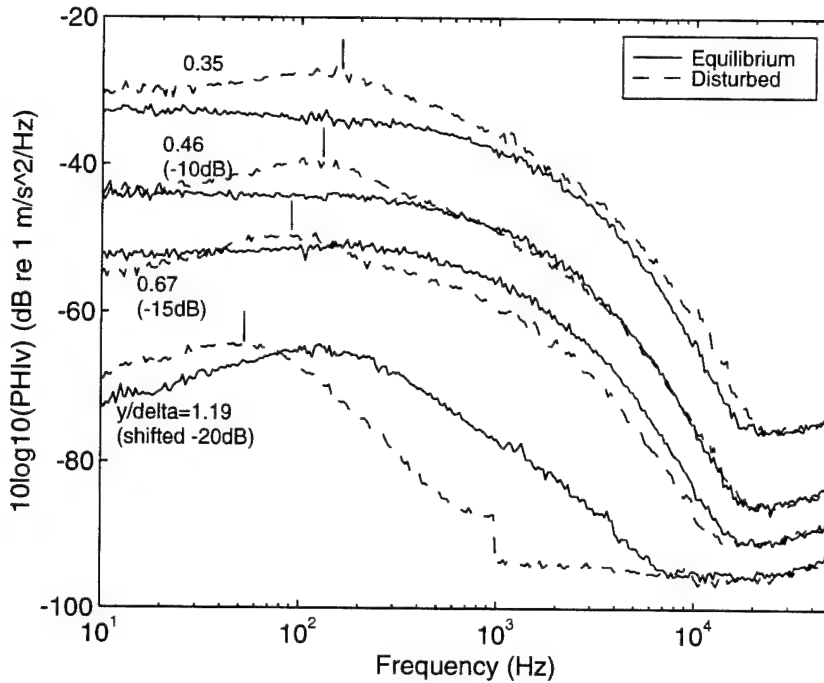


Figure 3.15: Selected wall-normal velocity spectra outside of the location of peak disturbed  $v_{rms}$ .

length scales equal to the distance from the wall. Assuming further that these structures convect with a speed equal to the edge velocity results in

$$f_{peak}(y) = \frac{1}{2\pi} \frac{U_e}{y} \quad (3.8)$$

Frequencies predicted by this equation are indicated in Figure 3.15.

The equilibrium flow, on the other hand, does not show a peak until  $y/\delta = 0.66$ , where it occurs at approximately 200 Hz. This peak also moves to lower frequencies with increasing  $y$ . By  $y/\delta \approx 1.5$  (not shown), the peak is at approximately 100 Hz. The movement of the equilibrium flow peak is linked to the induced irrotational motion at the boundary layer edge.

### 3.3.3 Wall-pressure statistics

Fluctuating wall pressure statistics are functions of both flow Reynolds number and sensor resolution. The Reynolds number determines the scales of turbulence structures present in the flow. Sensor resolution, generally expressed in wall units as  $d^+ = d/l_\nu = du_\tau/\nu$  where  $d$  is the effective diameter, determines the scale of the turbulence structures that will be spatially averaged out. The wall-pressure statistics were examined for consistency with previous research and for any effects

Table 3.2: Wall pressure statistics, averaged over the X-wire surveys.

Transducer	rms (Pa)	Skewness	Kurtosis
Equilibrium TBL, $d_{mic} = 32l_\nu$			
$p_1$	1.535	0.0496	4.2627
$p_2$	1.465	0.0376	4.4550
Disturbed TBL, $d_{mic} = 23l_\nu$			
$p_1$	3.903	0.1426	4.1281
$p_2$	4.123	0.1861	4.2201
Uncertainties	0.011	0.039	0.342

of external disturbances. The results are presented in Table 3.2. The values listed are the averages over the X-wire surveys.

The rms levels for the equilibrium flow equate to  $3.15\tau_w$  and  $3.01\tau_w$  for transducers  $p_1$  and  $p_2$ , respectively. This is in excellent agreement with other experimental results compiled by Farabee and Casarella [3.10] for transducer sizes less than  $d^+ = 80$ . The disturbed-flow rms levels are approximately three times those of the equilibrium flow, consistent with the mean inflow shown in Figure 3.3, and the increased turbulence activity in the vicinity of reattachment [3.11].

External disturbances that could possibly affect the pressure measurements include facility noise and the presence of the hot-wire/traverse assembly. As noted in Sections 2.2 and 2.7.2, the facility noise is limited to frequencies of 50 Hz and below, and is removed by digital filtering. Farabee and Casarella [3.10] note that low-frequency components contribute little to the turbulent rms level and can be neglected. The effects of the hot-wire/traverse assembly for the equilibrium flow can be seen in Figure 3.16. The hot wire influences transducer  $p_1$  by increasing the pressure levels by approximately 3 percent when near the wall. Transducer  $p_2$ , situated upstream, is unaffected. This effect is also evident in the power spectra, discussed in Section 3.3.4. The disturbed flow case is shown in Figure 3.17. For this case, the wire/traverse assembly affects both transducers, increasing the rms levels by 3–5 percent over the average values. The lower mean velocity levels in the retarded layer allow the traverse influences to penetrate further upstream than for the equilibrium layer. The skewness and kurtosis coefficients for both flows were examined in a like manner and found, within the uncertainty of the measurements, to be unaffected by the traverse.

The skewness and kurtosis for random data with a Gaussian probability distribution are zero and three, respectively. Referring to Table 3.2, the equilibrium flow wall-pressure skewness is seen to be essentially zero, while the disturbed flow value is slightly positive. Both flows exhibit high values of the kurtosis, indicating that the signals are characterized by spikes of large amplitude. The disturbed flow experiences relatively more positive, large amplitude fluctuations, consistent with the

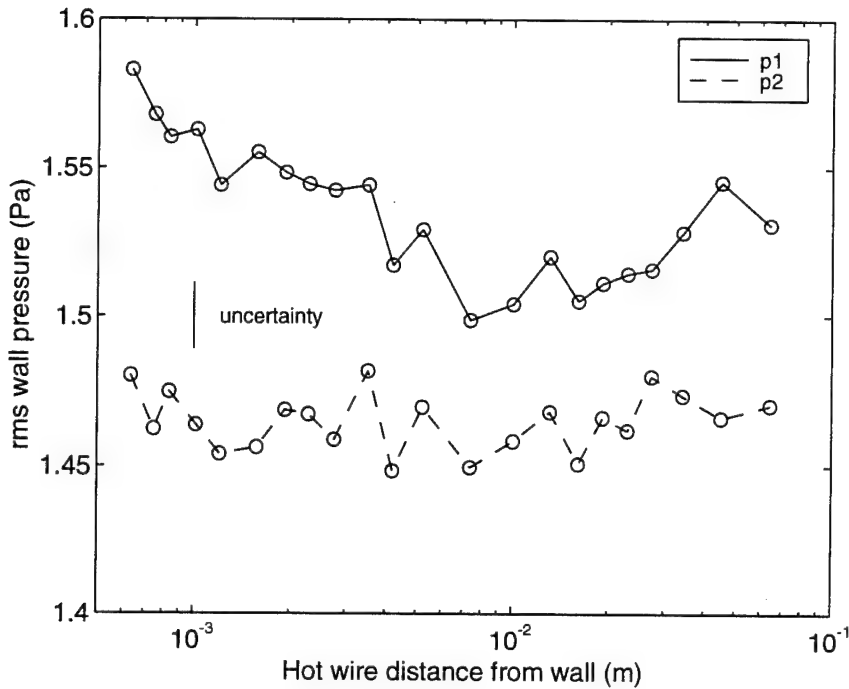


Figure 3.16: Effect of the hot wire traverse assembly on the equilibrium flow wall pressure.

negative mean  $V$  velocity. The equilibrium flow, on the other hand, is symmetric, with nearly equal numbers of positive and negative large-amplitude excursions.

Further discussion of the wall-pressure skewness is necessary. Schewe [3.12] studied the dependence of measured wall-pressure statistics on transducer size. He concluded that as transducer size increases, spatial averaging drives the statistics to their Gaussian values. His results showed that skewness  $\rightarrow 0$  for  $d^+ > \approx 50$  and kurtosis  $\rightarrow 3$  for  $d^+ > \approx 325$  at  $Re_\theta = 1400$ . Interpolating Schewe's results, the skewness for the present investigation equilibrium flow should be approximately  $-0.15$  instead of zero.

This discrepancy was resolved by a series of tests that focused on the processing of the pressure signal, namely, the method of high-pass filtering to remove unwanted noise. The hot wire traverse assembly was removed from the tunnel to eliminate as many external-flow disturbances as possible, and wall-pressure data were recorded for a nominal 16 m/s equilibrium TBL. Three methods of high-pass filtering were used to remove the remaining facility noise:

1. Analog filter prior to digitization, elliptic type of order 5, cutoff frequency=100 Hz.
2. Digital filter after digitization, Butterworth type of order 5, single pass, cutoff frequency=100 Hz.



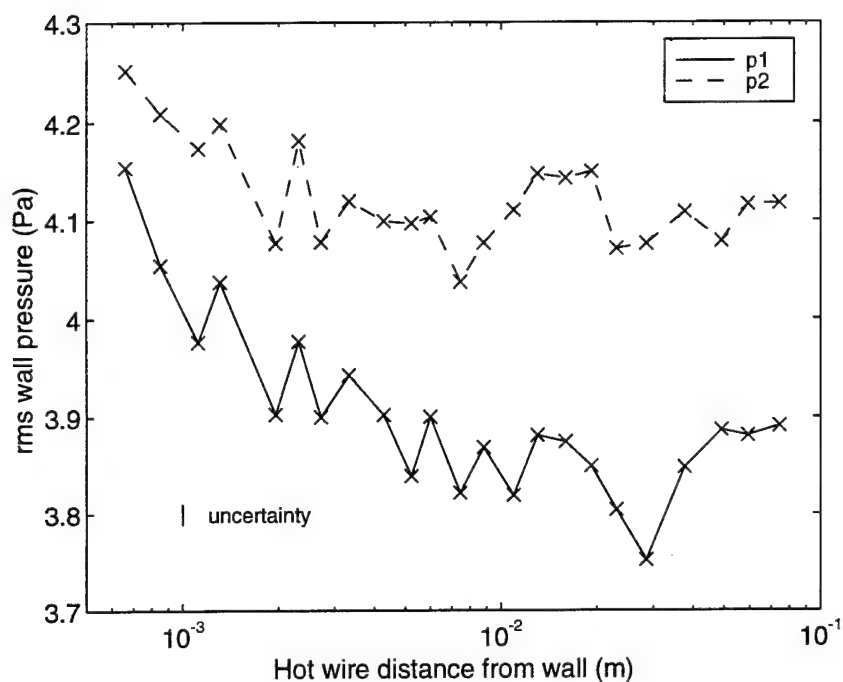


Figure 3.17: Effect of the hot wire traverse assembly on the disturbed flow wall pressure.

3. Digital filter after digitization, Butterworth type of order 5, double pass, cutoff frequency=100 Hz.

The results are presented in Table 3.3. The analog and single-pass digital filters introduce phase lags into the data and give equivalent results for the skewness, which are consistent with the results of Schewe. The double-pass digital filter, on the other hand, introduces no phase lags and produces results equivalent to Table 3.2. The ways in which phase lags influence the skewness are not understood, but the effects are clearly evident. One must therefore be careful when reviewing results in the literature, as many researchers neglect to specify the exact type of filtering performed

Table 3.3: Effects of high-pass filtering on equilibrium TBL wall pressure skewness.

Filter type	Skewness
Analog, elliptic	-0.1996
Digital, Butterworth, single pass	-0.1999
Digital, Butterworth, double pass	0.0212

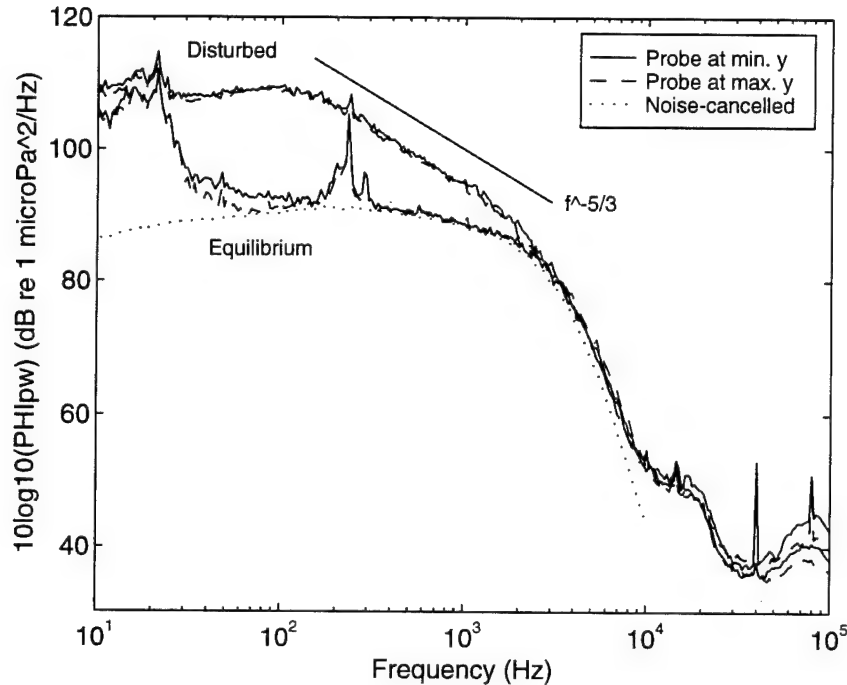


Figure 3.18: Equilibrium and disturbed TBL wall pressure spectra from microphone  $p_1$ . The noise-cancelled equilibrium spectrum is from Farabee and Casarella [3.10].

on the data. Within the precision of the measurements, the rms and kurtosis values showed no dependence on filter choice. Peak event analysis, as detailed in Section 3.4, is likewise unaffected.

### 3.3.4 Wall-pressure power spectra

Figure 3.18 presents the wall-pressure power spectra for both the equilibrium and disturbed flows. For each case, measurements are shown with the X-wire probe closest to and furthest away from the wall. This illustrates again the effect of the traverse and hot wire probe on the pressure measurements: below 1000 Hz, the spectral levels with the probe close to the wall are slightly above those with the probe far away. Integration of these spectra over the frequency range corresponding to the digitized data (100–12800 Hz) results in the same percentage increase reported in Section 3.3.3.

The equilibrium spectra show the expected broad-banded behavior. Also included in Figure 3.18 is an equilibrium-flow spectrum. This spectrum was obtained in the same facility at a flow speed  $U_e = 15.2$  m/s, using a noise cancellation technique to eliminate facility noise [3.10]. The technique involves subtracting the outputs of two microphones located at the same streamwise location but separated by a spanwise distance. The spectrum is shown to illustrate the regions where the current data

are contaminated by unwanted acoustic sources. The first region is the frequency range below 40 Hz. The noise source here is the tunnel's centrifugal blower, which was identified by Farabee [3.7] and Helal, et al. [3.13]. The second region of contamination is in the range 150–300 Hz. This source, identified by Wilczynski [3.8], is Strouhal shedding from the hot-wire traverse. The fact that these do not show up in the velocity spectra confirms that they are acoustical. The blower noise was removed by digital high-pass filtering at 100 Hz during data reduction. At this stage of the signal processing, no attempt was made to remove the traverse-related noise, and its presence will be acknowledged. However, calculations made on wall-pressure data collected in a clean wind tunnel revealed no discernable effects of the traverse on peak-event detection results.

Compared to the equilibrium pressure spectra, the disturbed-flow pressure spectra exhibit excess low-frequency components, as was also seen in the disturbed flow velocity spectra. Farabee [3.7] showed that this region of the spectrum scales on "disturbance variables", given as

$$\frac{\Phi_p(\omega, x/h)U(\delta_d)}{(\rho\bar{u}\bar{v})^2\delta_d} \quad \text{vs.} \quad \frac{\omega h}{U_e} \quad (3.9)$$

Here,  $\omega$  is the frequency in rad/s, the length scale,  $\delta_d$ , is the distance that the disturbance layer is away from the wall,  $h$  is the step height, and the pressure scale,  $-\rho\bar{u}\bar{v}$ , is the maximum value of the turbulence Reynolds stress measured in the disturbance layer. This scaling means that the disturbance layer is the source of the excess low-frequency energy. The region of  $f^{-5/3}$  behavior, as in the  $u$  velocity spectra, is characteristic of free shear layer flows.

The spectra for the two flows show identical behavior in the high-frequency range above 3000 Hz. The source of these high-frequency fluctuations is the small-scale structures near the wall [3.10, 3.14]. Since the two flows show nearly identical near-wall turbulence levels (Figure 3.4), their similarity in pressure spectral behavior is not surprising. However, a word of warning is in order. Farabee had shown for equilibrium flows that the high-frequency data collapsed on inner variables. Since the values of  $t_\nu$  between the equilibrium and disturbed flows differ by a factor of two, the disturbed flow will not collapse on inner variables. This raises the question of the proper inner variable scaling for nonequilibrium flows. This is also related to the questions of inner/outer layer coupling, since  $u_\tau$  depends on the outer layer, but the near wall turbulence structure of  $u_{rms}$  and  $v_{rms}$  appears to be independent.

### 3.4 Peak-event detection

The analysis up to this point has been in the form of time averages and Fourier spectra. Each of these involved integration of the signals over long times. Attention will now be focused on those sections of the time series that are believed to be associated

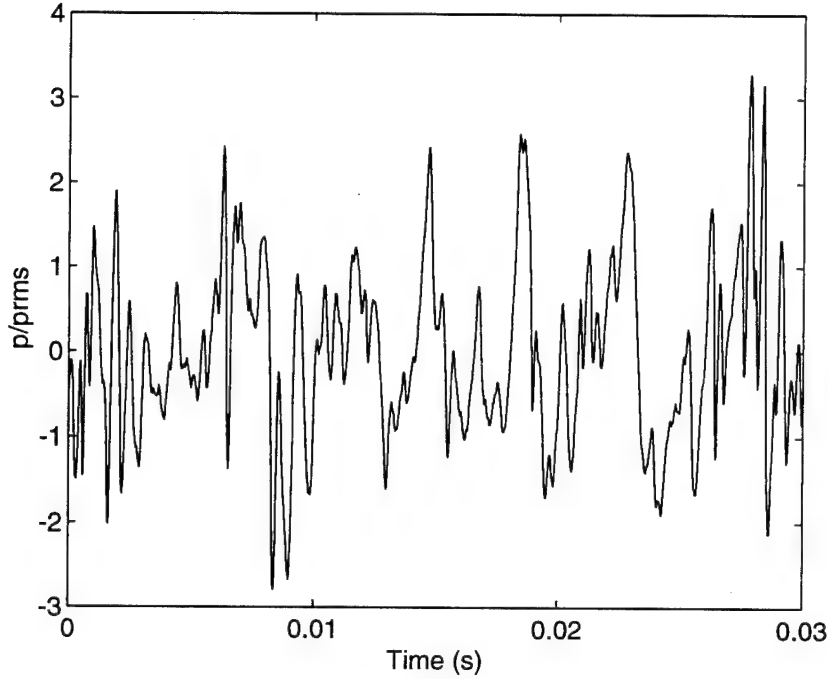


Figure 3.19: Sample time record of the equilibrium flow fluctuating wall pressure.

with the active, or turbulence-producing motions. This requires a method of identifying or detecting turbulence-related portions of a signal. Figure 3.19 shows approximately 1000 samples of the wall-pressure signal from the equilibrium boundary-layer flow. High-amplitude fluctuations are apparent and are intuitively associated with the turbulence. Hence, the most basic scheme is to declare an *event* when the signal exceeds a given threshold value. The threshold is expressed as a multiple of the rms value. This is known as peak-event detection. For example, peak wall-pressure events occur when  $|p| > \kappa p_{rms}$ , where  $\kappa$  is the threshold level. In the discussion to follow, positive and negative events will be distinguished by the sign of  $\kappa$ :

$$\begin{aligned} \kappa > 0 &\Rightarrow \text{positive event, } p > \kappa p_{rms} \\ \kappa < 0 &\Rightarrow \text{negative event, } p < \kappa p_{rms} \end{aligned} \quad (3.10)$$

The specific peak-event detection algorithm was that used by Karangelen [3.15] and Wilczynski [3.8]. The time record was scanned, and four points for each event identified: the point where the signal exceeded the given threshold (the trigger point), the point of peak amplitude, and the two zero crossings bracketing the trigger point. Figure 3.20 illustrates this for a threshold level  $\kappa = 2$ , using the two positive events from the center of Figure 3.19. The indices to these points were stored, from which the following event statistics were compiled: the number of events, the average event shape, the average event duration, the distribution of the time between consecutive events, and the contribution of the events to the total record length and

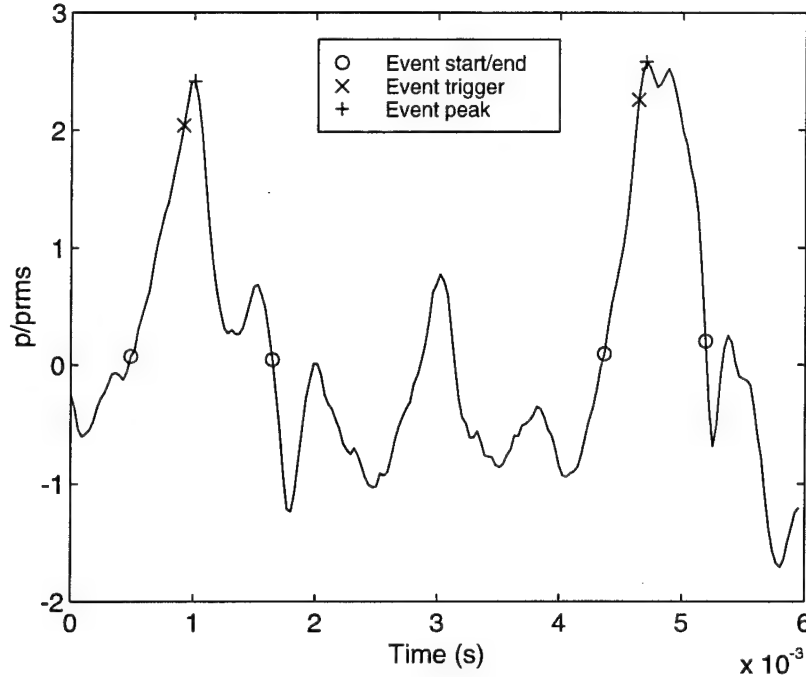


Figure 3.20: Consecutive positive wall-pressure peak events for threshold  $\kappa = 2$ .

to the signal's fluctuating power.

Average event shapes were computed by setting a window around each event, centered about the peak magnitude, and ensemble averaging. The event duration,  $\Delta t$ , was defined as the time between the zero crossings. The zero crossings were also used to determine the fractional contribution of the events to the total record length and to the fluctuating power. The power fraction was computed relative to the signal's variance as opposed to the signal's rms value, as reported by previous investigators. For comparison, the two quantities are related by

$$\text{rms fraction} = (\text{power fraction})^{1/2} \quad (3.11)$$

The power fraction is felt to be more meaningful and less ambiguous, since rms fractions often total to values greater than one. The time between consecutive events,  $\Delta T$ , was defined as the time between trigger points. The analysis was performed on both the wall pressure and the Reynolds stress time records.

### 3.4.1 Wall-pressure peak events

Table 3.4 summarizes the equilibrium and disturbed flow wall-pressure peak-event detection statistics. Results are given separately for positive and negative events, for threshold values  $\kappa = 1-3$ . The equilibrium flow results are in close agreement with the results of Karangelen [3.15] and Wilczynski [3.8]. The large amplitude

Table 3.4: Wall pressure peak-event detection statistics for transducer  $p_1$ .

$\kappa$	Time fraction	Power fraction	$\Delta t^+$	$\Delta T^+$	Number of events	Frequency per $1000t^+$
Equilibrium						
+1	<b>0.330</b>	<b>0.487</b>	<b>17.1</b>	<b>51.9</b>	<b>5034</b>	<b>19.3</b>
-1	0.343	0.459	17.4	50.7	5150	19.7
+2	<b>0.124</b>	<b>0.308</b>	<b>19.6</b>	<b>157.7</b>	<b>1654</b>	<b>6.3</b>
-2	0.114	0.260	19.3	169.6	1540	5.9
+3	<b>0.029</b>	<b>0.118</b>	<b>19.4</b>	<b>666.8</b>	<b>391</b>	<b>1.5</b>
-3	0.022	0.089	17.1	765.0	342	1.3
Disturbed						
+1	<b>0.343</b>	<b>0.494</b>	<b>18.0</b>	<b>52.6</b>	<b>2472</b>	<b>19.0</b>
-1	0.352	0.454	19.1	54.1	2405	18.5
+2	<b>0.137</b>	<b>0.326</b>	<b>19.8</b>	<b>144.0</b>	<b>901</b>	<b>6.9</b>
-2	0.105	0.246	20.7	196.6	659	5.1
+3	<b>0.039</b>	<b>0.147</b>	<b>19.7</b>	<b>503.9</b>	<b>257</b>	<b>2.0</b>
-3	0.019	0.075	18.2	965.6	134	1.0

events are seen to contribute a majority to the total power. Events exceeding  $3p_{rms}$  occur 5 percent of the time but contribute almost 21 percent to the total power. To appreciate the significance, Karangelen compared equilibrium turbulent wall-pressure data to a random, Gaussian, signal. To facilitate the comparison, she used only those portions of the signals that actually exceeded the threshold. She showed that for a threshold  $\kappa = 3$ , the turbulent wall pressure events occupied 1 percent of the time but contributed 14 percent to the total power, while the Gaussian signal events occupied 0.4 percent of the time while contributing only 4 percent to the power. This is consistent with the high kurtosis values seen in Table 3.2.

In Table 3.4, the average event durations and time between events are given in viscous time units,  $t^+ = t/t_\nu$ . Also, the frequency of realizations is reported in the form of number of events per  $1000t^+$ . The choice of viscous or wall variable scaling reflects the belief that wall-pressure events are related to the turbulent burst frequency [3.8, 3.15–3.17]. The average event duration is seen to be relatively constant with threshold value, ranging from 17 to 20 viscous time units. As expected, the average time between events increases with increasing threshold.

The disturbed-flow event statistics are remarkably similar to the equilibrium-flow results. The sum of the positive and negative event contributions to the total time and power for a given threshold are equivalent to the equilibrium flow case. However, the disturbed flow results show relatively more positive than negative events, as seen in the power fraction and event frequency values. This is consistent with the positive skewness results shown in Table 3.2. It is noteworthy that event durations, times between events, and event frequencies for the disturbed flow reduce to the

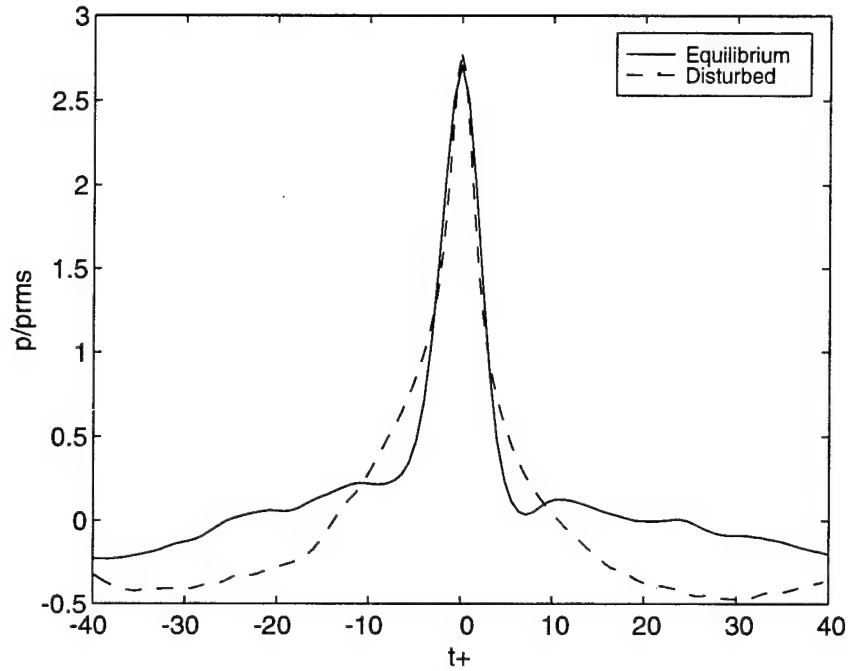


Figure 3.21: Average positive wall-pressure peak-event shapes,  $\kappa = 2$ .

equilibrium values when scaled on wall variables, particularly in light of the drastic differences in the number of events observed. This implies that the wall-pressure peak events are indeed driven by the near-wall flow, and that effects of the outer layer disturbances on the near-wall motion are secondary.

Average event shapes for a threshold level of 2 are presented in Figures 3.21 and 3.22. Shapes for the equilibrium flow are very similar to those reported by Karangelen [3.15] and Wilczynski [3.8]. The positive events show an overshoot on the return from the peak value. The negative events are inverted mirror images of the positive events. The disturbed flow average event shapes match the equilibrium case over the central portions of the events, but have broader bases. The portions of the pressure signal away from the event also appear to be more highly correlated than in the equilibrium flow, where the ensemble average oscillates about zero. These observations seem to be consistent with the increased lower-frequency components produced by the step flow. The disturbed-flow event shapes are not symmetric, with the rise in pressure to the positive peaks being more gradual than the falloff beyond the peaks. Like the equilibrium flow, the disturbed-flow negative pressure events are inverted mirror images of their positive counterparts.

Figures 3.23 and 3.24 show the distribution of the time between positive pressure events for a threshold level of 1. The time axis has been normalized by the mean time between events for that threshold. The equilibrium flow shows the same log-normal-like distribution observed by Karangelen and Wilczynski. Karangelen [3.15]

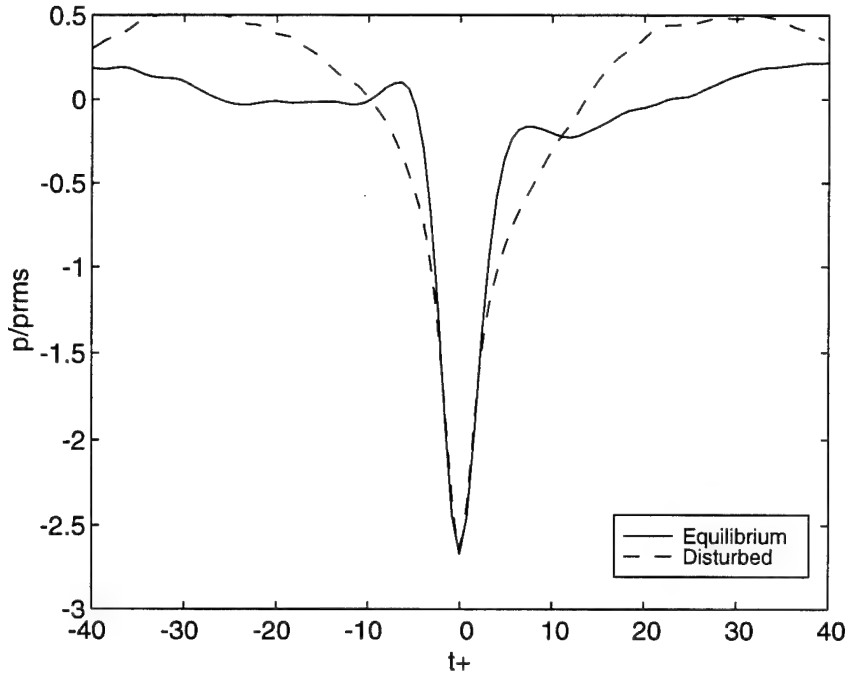


Figure 3.22: Average negative wall-pressure peak-event shapes,  $\kappa = 2$ .

showed that a Gaussian signal has a log-normal distribution for the time between events. As we have seen, the equilibrium wall pressure signal has a probability distribution that is similar to Gaussian, but with an elevated value for the kurtosis. In contrast, the disturbed-flow distribution is much more uniform. Results for the negative events are very similar and are not shown.

### 3.4.2 Reynolds stress peak events

Peak-event detection statistics for the Reynolds stress are presented in Table 3.5. Results are given for a threshold level  $\kappa = 2$  at four locations across the boundary layer. Here, the threshold is relative to the product  $u_{rms}v_{rms}$ . Unlike the wall pressure events, wall variable scaling does not collapse the equilibrium and disturbed results. This is perhaps not surprising since the disturbed flow is dominated by large scale eddy structures that span the entire boundary layer. Even more so than for the wall pressure events, the large amplitude  $uv$  events contribute a majority to the signal power, totaling over 70 percent for both flows. Turbulence production is clear for both flows; the power fractions for the negative events are roughly 3–5 times the levels of the positive events. The exception is the disturbed TBL near the wall, where positive events contribute 13 percent more than the negative events. At this location, the total disturbed-flow Reynolds stress is very low, as seen in Figures 3.10 and 3.11. This indicates again that the disturbed-flow inner layer has either not



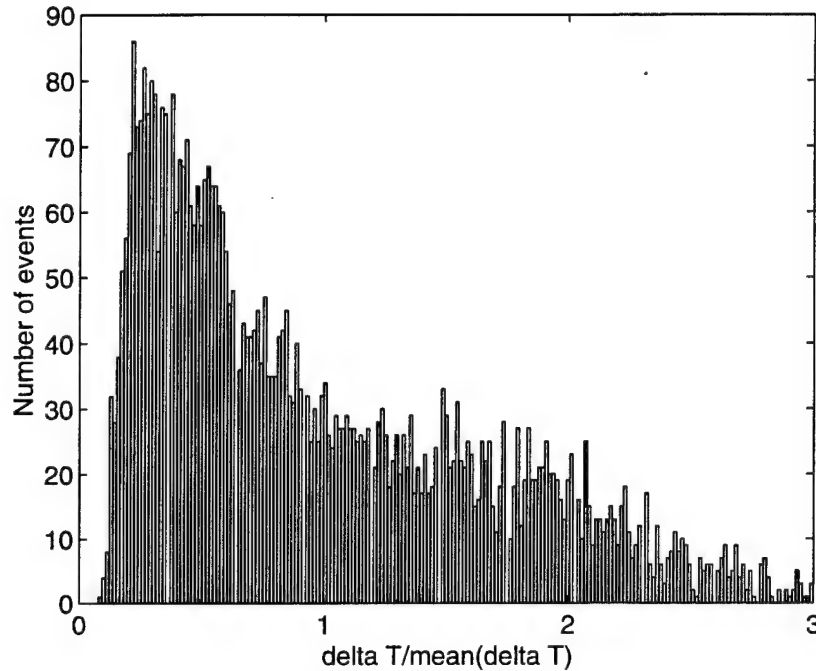


Figure 3.23: Distribution of the time between equilibrium-flow positive wall-pressure peak events,  $\kappa = 1$ .

reached a fully developed state or is contaminated by the outer-layer structures.

Considering event duration, spacing, and frequency, the equilibrium flow results are roughly constant across the boundary layer. This corresponds to the relatively constant levels of Reynolds stress shown in Figure 3.10. The disturbed-flow event durations are even more constant across the layer. Again, this is consistent with a characteristic structure that spans the boundary layer. The disturbed flow time between events, and hence the event frequency, however, are not constant. The behavior of these statistics follows the overall level of Reynolds stress, which was shown to peak at  $y/\delta = 0.2$ . As the Reynolds stress increases, large-amplitude negative events occur more frequently.

Average  $uv$  event shapes across the boundary layers, for a threshold level of  $-2$ , are presented in Figures 3.25–3.28. The differences in event durations noted in Table 3.5 are apparent. Figures 3.26 and 3.27 are for  $y/\delta = 0.08$  and  $0.25$ , corresponding to the log-law region. Here, the event shapes and durations are the most similar, but wall variable scaling still cannot be said to collapse the data. Figure 3.28 is for  $y/\delta = 0.65$ , which is outside the location of the disturbance layer. The magnitude of the events has increased; a consequence of the increased intermittency.

The Reynolds stress events were investigated further by discriminating the individual signs of the  $u$  and  $v$  signals; i.e. the quadrants of the  $u-v$  plane. This is known as quadrant-event detection. Events detected according to quadrant criteria

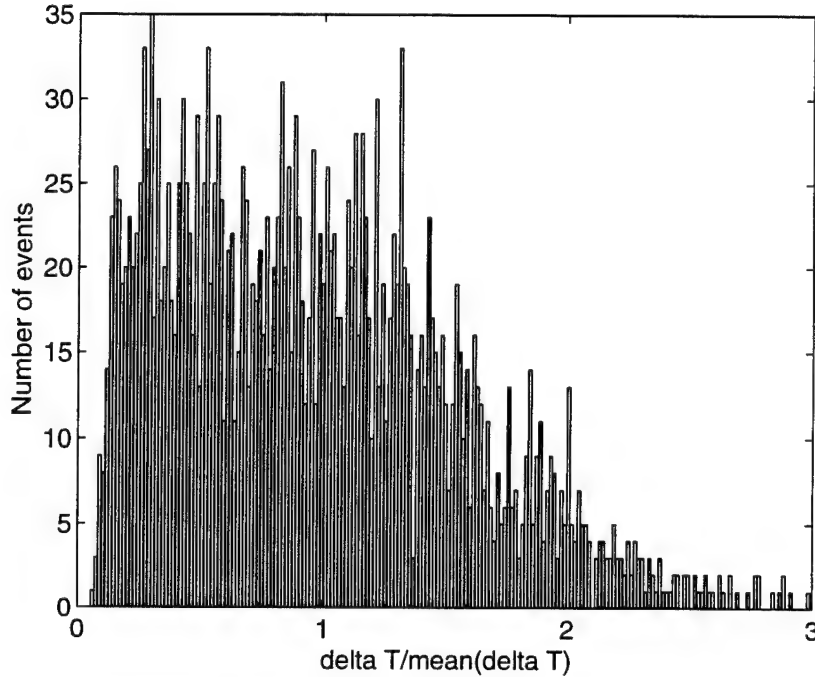


Figure 3.24: Distribution of the time between disturbed-flow positive wall-pressure peak events,  $\kappa = 1$ .

are designated Q events. An event is declared present as before, when the  $uv$  product exceeds a specified threshold. However, the limits of the event are determined by when the signal “enters” and “leaves” the quadrant. It should be noted that because of the discrete nature of the  $u$  and  $v$  time sequences, a quadrant change can occur with or without a zero crossing of the  $uv$  product. This means there is not necessarily a one-to-one correspondence between, for example, second or fourth quadrant events and negative  $uv$  events.

The event statistics for the turbulence-producing quadrant events across the boundary layers are presented in Table 3.6. Positive Reynolds stress or negative  $uv$  corresponds to the second (Q2) and fourth (Q4) quadrants of the  $u$ - $v$  plane. For the equilibrium flow, Q2 events occur more often and contribute more power than the Q4 events at all tabulated locations. In contrast, the disturbed flow exhibits a change from Q4 to Q2 dominance with increasing  $y$ . To examine this further, the event frequencies for all quadrants across the boundary layers are plotted in Figures 3.29 and 3.30.

In Figure 3.29, Q2 and Q4 quadrant events are seen to dominate the equilibrium flow over most of the boundary layer. For  $y/\delta > 0.7$ , Q1, Q3, and Q4 events occur with roughly the same frequency, while Q2 events remain dominant. In Figure 3.30, the disturbed flow is seen to be dominated by Q1 events at the closest measurement station. This is further evidence that the inner layer is contaminated. Moving away

Table 3.5: Reynolds stress peak-event detection statistics.

$y^+$ ( $y\delta$ )	Time fraction	Power fraction	$\Delta t^+$	$\Delta T^+$	Number of events	Frequency per $1000t^+$
Equilibrium, $\kappa = +2$						
25.9 (0.022)	0.053	0.185	14.0	261.7	998	3.8
93.1 (0.077)	0.039	0.138	7.5	191.2	1364	5.2
300.0 (0.250)	0.041	0.152	8.4	202.0	1293	4.9
781.1 (0.650)	0.044	0.146	9.1	203.7	1280	4.9
Equilibrium, $\kappa = -2$						
25.9 (0.022)	0.148	0.576	14.7	99.5	2625	10.0
93.1 (0.077)	0.183	0.628	11.7	63.8	4095	15.7
300.0 (0.250)	0.191	0.600	13.8	72.3	3613	13.8
781.1 (0.650)	0.182	0.677	15.6	85.4	3054	11.7
Disturbed, $\kappa = +2$						
24.9 (0.020)	0.091	0.488	5.6	61.7	2110	16.2
97.2 (0.077)	0.069	0.275	5.7	82.4	1581	12.1
320.2 (0.255)	0.040	0.151	4.5	113.1	1152	8.8
833.6 (0.664)	0.063	0.182	5.6	88.5	1471	11.3
Disturbed, $\kappa = -2$						
24.9 (0.020)	0.103	0.352	6.7	64.9	2007	15.4
97.2 (0.077)	0.163	0.523	8.2	50.5	2578	19.8
320.2 (0.255)	0.219	0.653	9.2	41.8	3112	23.9
833.6 (0.664)	0.156	0.697	7.9	50.6	2572	19.7

from the wall, first Q2, then Q4 events become prevalent, with Q4 dominating over most of the layer. The changeover point from Q2 to Q4 occurs at the disturbance location,  $y/\delta \approx 0.2$ .

Another view of the situation near the wall is provided in Figures 3.31 and 3.32. Here, the peak value of each quadrant event exceeding a threshold value  $\kappa = 1$  is plotted on the  $u$ - $v$  plane, providing a measure of the joint probability density function. The dominance of the equilibrium flow Q2 events is again evident. In Figure 3.32, the dominance of the Q1 and Q4 events, both in magnitude as well as in number, is also confirmed. These two quadrants involve positive  $u$ , or accelerating perturbations. This is consistent with the larger values of disturbed flow  $u$ -skewness shown in Figure 3.6.

### 3.5 Discussion

Overall flowfield and wall-pressure results have been presented on two turbulent boundary-layer flows: an equilibrium layer and a disturbed layer formed downstream

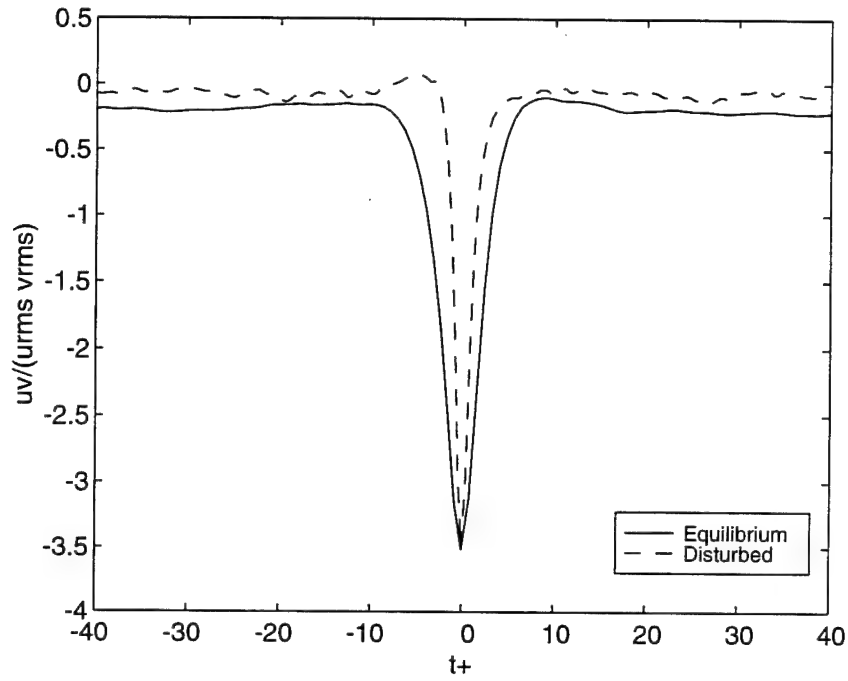


Figure 3.25: Average  $uv$  peak-event shapes at  $y/\delta = 0.02$ ,  $\kappa = -2$ .

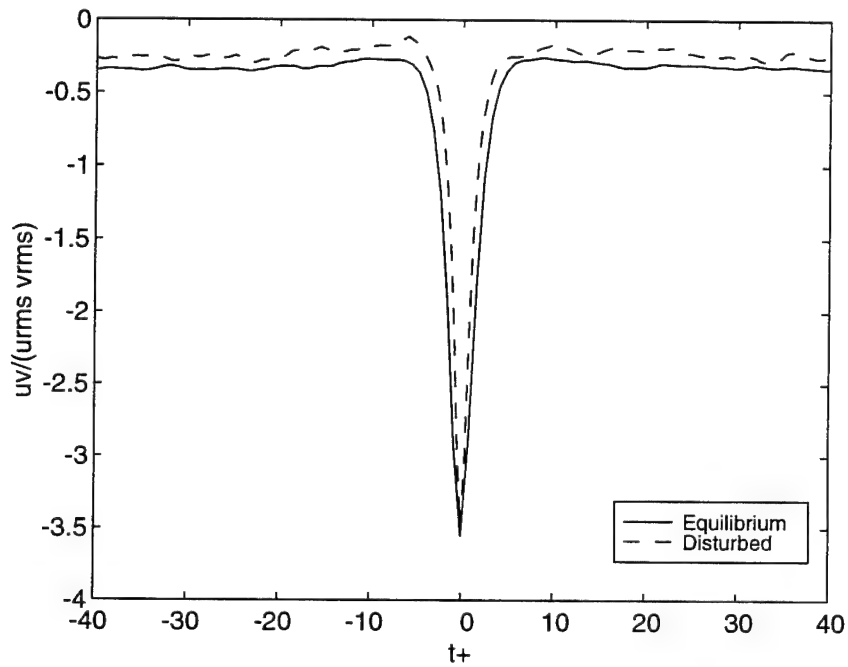


Figure 3.26: Average  $uv$  peak-event shapes at  $y/\delta = 0.08$ ,  $\kappa = -2$ .

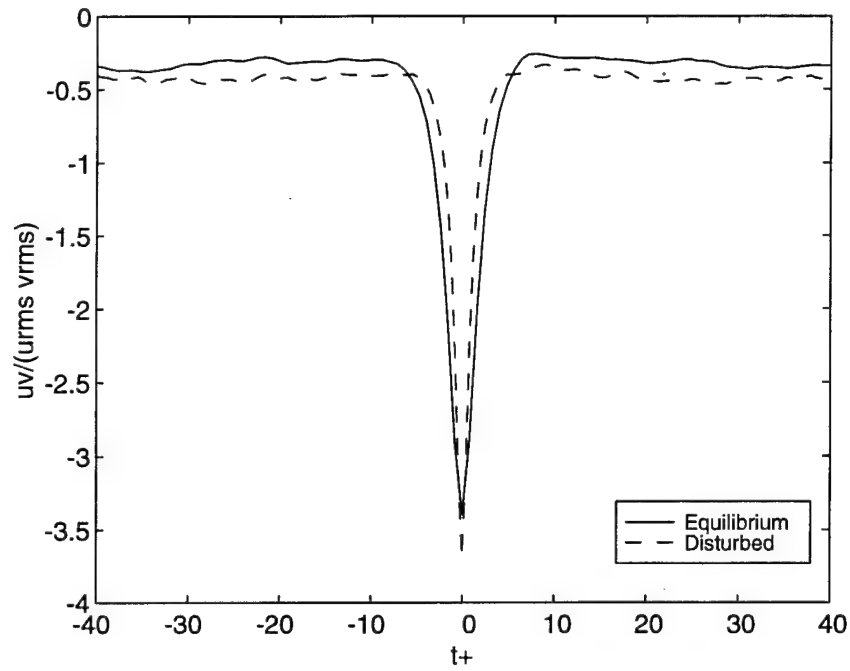


Figure 3.27: Average  $uv$  peak-event shapes at  $y/\delta = 0.25$ ,  $\kappa = -2$ .

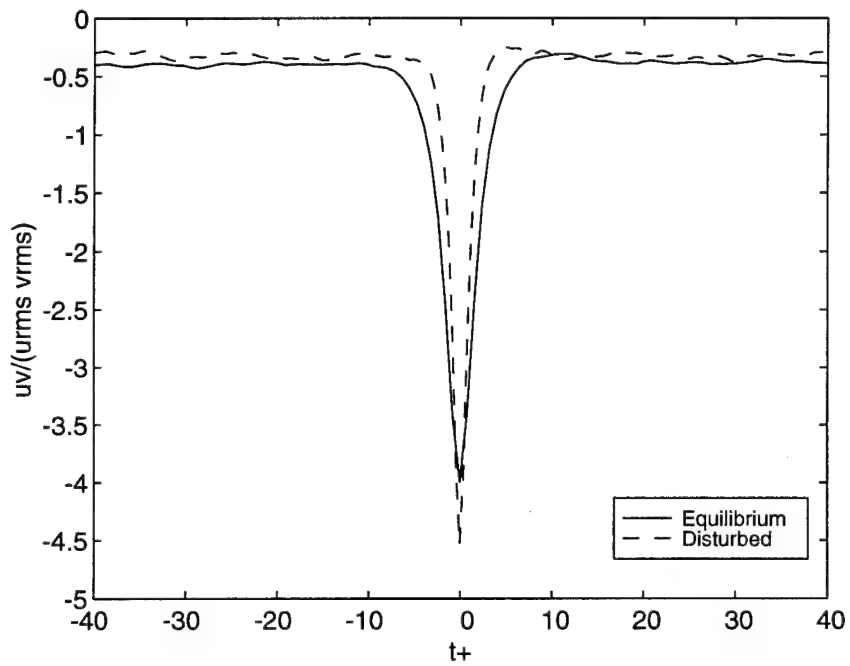


Figure 3.28: Average  $uv$  peak-event shapes at  $y/\delta = 0.65$ ,  $\kappa = -2$ .

Table 3.6: Reynolds stress quadrant-event detection statistics,  $\kappa = -2$ .

$y^+$ ( $y\delta$ )	Time fraction	Power fraction	$\Delta t^+$	$\Delta T^+$	Number of events	Frequency per $1000t^+$
Equilibrium, quadrant 2						
25.9 (0.022)	0.104	0.495	13.94	133.35	1957	7.5
93.1 (0.077)	0.101	0.425	10.92	107.61	2427	9.3
300.0 (0.250)	0.100	0.367	12.75	127.79	2043	7.8
781.1 (0.650)	0.109	0.562	13.38	122.96	2122	8.1
Equilibrium, quadrant 4						
25.9 (0.022)	0.040	0.081	15.24	382.61	683	2.6
93.1 (0.077)	0.076	0.201	11.56	152.43	1711	6.6
300.0 (0.250)	0.087	0.233	14.36	164.18	1589	6.1
781.1 (0.650)	0.069	0.115	18.89	273.78	951	3.6
Disturbed, quadrant 2						
24.9 (0.020)	0.048	0.132	8.56	179.23	727	5.6
97.2 (0.077)	0.072	0.176	10.02	138.18	938	7.2
320.2 (0.255)	0.123	0.455	8.74	70.81	1835	14.1
833.6 (0.664)	0.101	0.624	6.85	67.88	1918	14.7
Disturbed, quadrant 4						
24.9 (0.020)	0.056	0.220	5.67	101.66	1280	9.8
97.2 (0.077)	0.091	0.347	7.23	79.44	1640	12.6
320.2 (0.255)	0.096	0.198	9.77	101.80	1277	9.8
833.6 (0.664)	0.055	0.073	10.90	199.08	654	5.0

of reattachment of the flow over an aft-facing ramp. The two flows each had a nominal external velocity of 16 m/s and a boundary-layer thickness of approximately  $1200l_\nu$ . The data are of high quality. Comparisons of the statistical and spectral results for the equilibrium flow with the archived literature indicate that the sensors were of sufficiently small size to resolve the majority of the small-scale turbulent structures. The scaling for the disturbed flow was even more favorable due to its larger physical boundary-layer thickness and lower skin friction. Considering time-series analyses, the sampling intervals were less than one viscous time unit.

The primary purpose of this investigation is to shed light on the question of inner/outer layer coupling in turbulent wall-bounded flows. The developing boundary layer downstream of a ramp was chosen because it exhibits similarities to the baseline equilibrium case in the near-wall region, with the disturbances primarily limited to the outer regions. In particular, the two flows show the same classic log-law velocity profile for  $y^+ < 100$ , and equivalent  $u_{rms}$  and  $v_{rms}$  profiles for  $y/\delta < 0.02$  when scaled on outer-flow variables. In addition, the high-frequency behavior of the  $u$ ,  $v$ , and  $p$  power spectra are similar both in level and rolloff. Also, the wall pressure peak-event detection statistics and the central, high-gradient portion of the

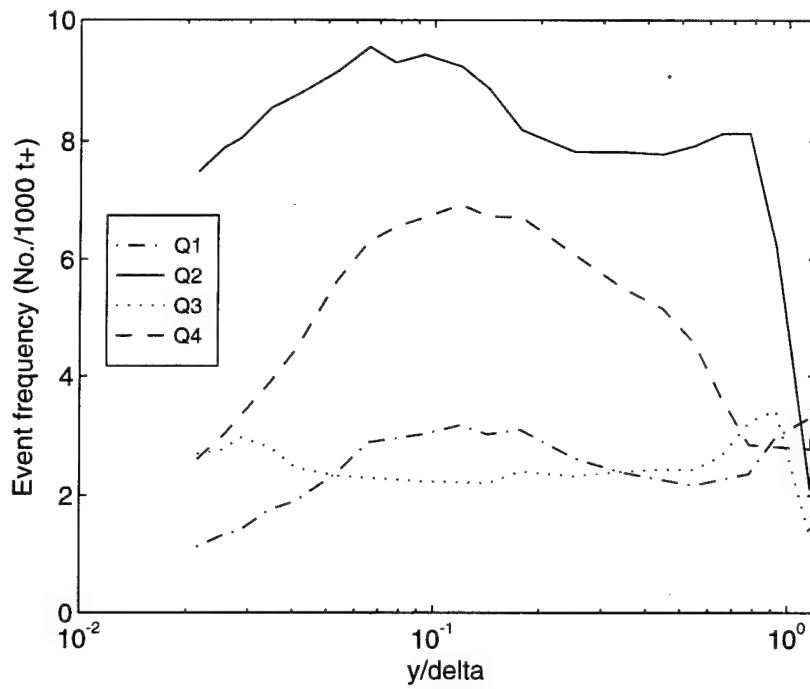


Figure 3.29: Equilibrium flow quadrant-event frequency,  $\kappa = 2$ .

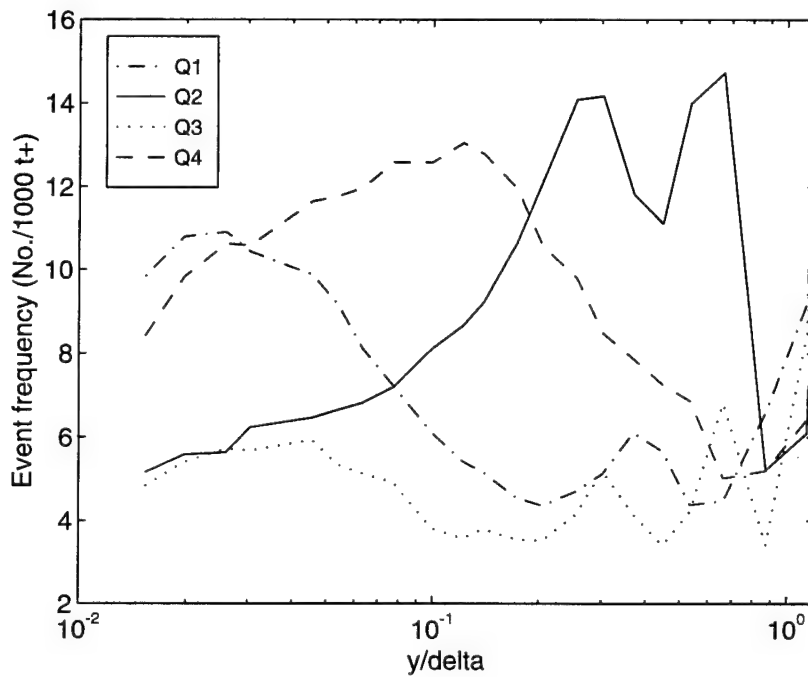


Figure 3.30: Disturbed flow quadrant-event frequency,  $\kappa = 2$ .

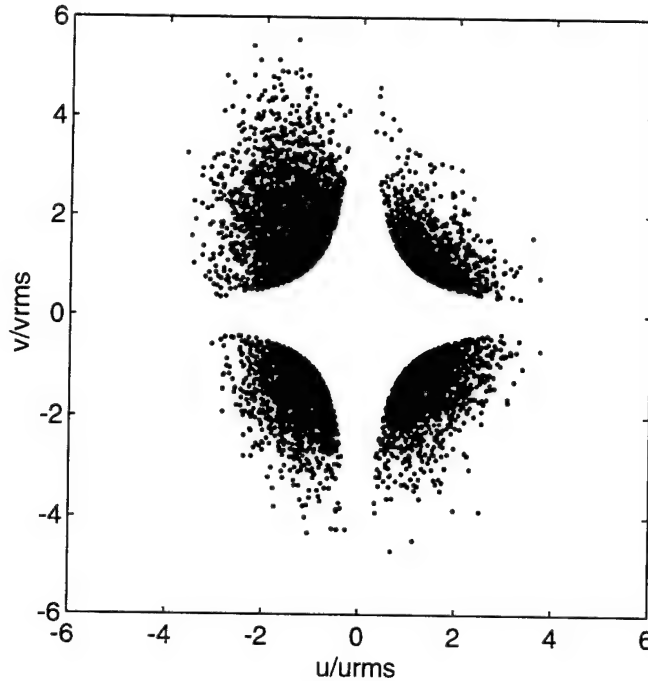


Figure 3.31: Peak values of the equilibrium flow Reynolds stress quadrant events at  $y/\delta = 0.02$ ,  $\kappa = 1$ .

event shapes all scale on wall variables. Taken together, these points indicate that near-wall, turbulence production-driven processes are common to both flows.

The most notable feature of the nonequilibrium flow is the presence of a disturbance layer located at  $y/\delta = 0.2$ . This disturbance layer, directly visible as peaks in the  $u_{rms}$ ,  $v_{rms}$ , and  $uv$  profiles, is a remnant of the free shear layer formed at the ramp trailing edge. Its effects are felt throughout the boundary layer and extend right down to the wall, where it manifests itself as a range of  $f^{-5/3}$  behavior in the  $u$  and  $p$  power spectra and increased correlation of the tails of wall-pressure peak events.

Other differences between the two flows were seen in the makeup of the peak-event detection results. At the wall, the disturbed flow showed relatively more positive peak-pressure events than the equilibrium flow. Away from the wall, different flow structures were indicated by the  $uv$  quadrant analysis. The equilibrium flow is dominated by second quadrant events over the entire boundary layer. In contrast, the disturbed flow is characterized by first and fourth quadrant events near the wall, changing to second quadrant dominance at the location of the disturbance layer.

While the event-detection results for the disturbed boundary layer are distorted by the large-scale, low-frequency motions introduced into the outer layer, the near-wall motions show a basic similarity to the equilibrium boundary layer. Based on these observations, the hypothesis is made that the inner and outer layer portions



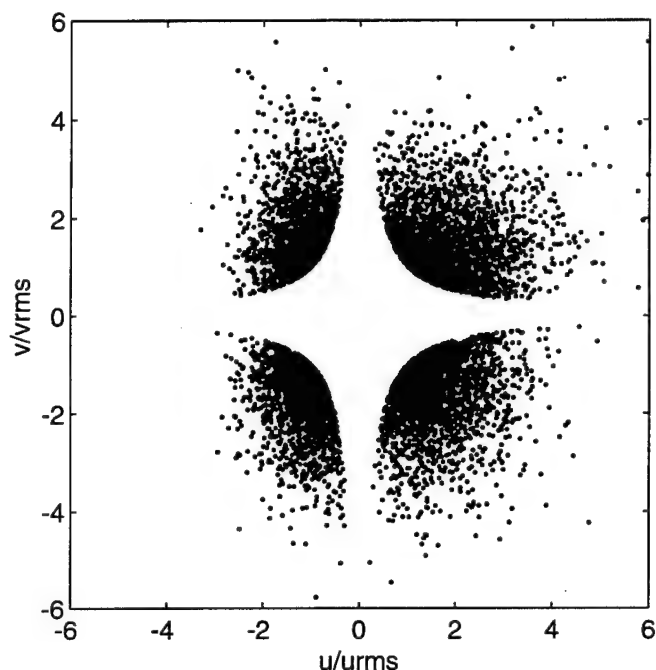


Figure 3.32: Peak value of the disturbed flow Reynolds stress quadrant events at  $y/\delta = 0.02, \kappa = 1$ .

of turbulent boundary layers are uncoupled. Proof of this hypothesis will require filtering of the disturbance “noise” from the disturbed flow data. The remainder of the research will focus on separating the disturbances from the common near-wall features using wavelet filtering techniques. This will allow a more thorough examination of the extent of the inner-outer-layer coupling.

## References

- [3.1] F. H. Clauser. The turbulent boundary layer. In *Advances in Applied Mechanics*, volume 4, pages 2–51. Academic Press, 1956.
- [3.2] C. Chandrsuda and P. Bradshaw. Turbulence structure of a reattaching mixing layer. *J. Fluid Mech.*, 110:171–194, 1981.
- [3.3] P. Bradshaw and F. Y. F. Wong. The reattachment and relaxation of a turbulent shear layer. *J. Fluid Mech.*, 52:113–135, 1972.
- [3.4] H. Tennekes and J. L. Lumley. *A First Course in Turbulence*. The MIT Press, 1972.

- [3.5] R. F. Blackwelder and J. H. Haritonidis. Scaling of the bursting frequency in turbulent boundary layers. *J. Fluid Mech.*, 132:87–103, 1983.
- [3.6] P. R. Bandyopadhyay and M. Gad-el-Hak. Reynolds number effects in wall-bounded turbulent flows. Technical Report NUWC-NPT TR 10,296, Naval Undersea Warfare Center, Newport, Rhode Island 02841-1708, 1994.
- [3.7] T. M. Farabee. An experimental investigation of wall pressure fluctuations beneath non-equilibrium turbulent flows. Technical Report DTNSRDC-86/047, David Taylor Naval Ship Research and Development Center, Bethesda, Maryland 20084-5000, 1986.
- [3.8] V. Wilczynski. *Organized Turbulent Structures and Their Induced Wall Pressure Fluctuations*. PhD thesis, The Catholic University of America, 1992.
- [3.9] F. H. Champagne. The fine-scale structure of the turbulent velocity field. *J. Fluid Mech.*, 86, part 1:67–108, 1978.
- [3.10] T. M. Farabee and M. J. Casarella. Spectral features of wall pressure fluctuations beneath turbulent boundary layers. *Phys. Fluids A*, 3(10):2410–2420, 1991.
- [3.11] T. M. Farabee and M. J. Casarella. Effects of surface irregularity on turbulent boundary layer wall pressure fluctuations. *Trans. of ASME, J. of Vibration, Stress, and Reliability in Design*, 106(10):343–350, 1984.
- [3.12] G. Schewe. On the structure and resolution of wall-pressure fluctuations associated with turbulent boundary-layer flow. *J. Fluid Mech.*, 134:311–328, 1983.
- [3.13] H. Helal, M. Casarella, and T. Farabee. An application of noise cancellation techniques to the measurement of wall pressure fluctuations in a wind tunnel. In Farabee, Hansen, and Keltie, editors, *Flow-Induced Noise Due to Laminar-Turbulence Transition Process*, number NCA 5, pages 49–59. ASME, 1989.
- [3.14] W. L. Keith, D. A. Hurdis, and B. M. Abraham. A comparison of turbulent boundary layer wall-pressure spectra. *Trans. of ASME, J. of Fluids Eng.*, 114:338–347, September 1992.
- [3.15] C. C. Karangelen. *Temporal and Spectral Features of Wall Pressure Fluctuations Beneath a Turbulent Boundary Layer*. PhD thesis, The Catholic University of America, 1991.
- [3.16] A. V. Johansson, J. Her, and J. H. Haritonidis. On the generation of high-amplitude wall pressure peaks in turbulent boundary layers and spots. *J. Fluid Mech.*, 175:119–142, 1987.

- [3.17] J. H. Haritonidis, L. S. Gresko, and K. S. Breuer. Wall pressure peaks and waves. In Kline and Afgan, editors, *Near-Wall Turbulence: Proceedings of the 1988 Zoran Zaric Memorial Conference*, pages 397–417. Hemisphere, 1990.

## Chapter 4

# Application of wavelet filtering

### 4.1 Introduction

The previous chapter introduced the concept of event detection, wherein the portions of a signal that satisfy a given criteria are noted for further analysis. Identification of the desired event and determination of the event statistics are hampered by the presence of "noise" in the data. Noise in this instance includes unwanted signal components as well as the more common sources such as imperfect transducer response and electrical line noise. For example, the wall pressure is obtained as the integral of turbulent sources in the entire velocity field. If one wishes to study the pressure resulting from a particular flow region, the influences from other regions need to be excluded. This is precisely what is required to achieve the present goal of assessing the relative effects of the inner and outer layer flow structures on the turbulence production mechanism. This chapter examines a filtering scheme based on wavelet transforms to accomplish this selective exclusion.

As reported by Eckelmann [4.1], Kobashi and Ichijo [4.2] used high- and low-pass filters to separate pressure fluctuations produced by the boundary-layer bulges from those originating within the boundary layer. Naguib and Wark [4.3] discriminated between the influences of different flow regions by using FIR band-pass filters matched to the spectral signature of each region. For the current goal of learning more about the sources of turbulent events, traditional Fourier-based analysis may not be ideal. As noted by Tennekes and Lumley [4.4, p. 259], and more recently by Zubair [4.5], eddies or organized structures are associated with many Fourier coefficients and the phase relations among them. Therefore, any frequency-based filtering will affect all structures to some degree, those of interest as well as those considered noise. A filtering scheme based on structure or scale instead of frequencies may be more appropriate.

This chapter will briefly review wavelet theory, develop a wavelet filter, and assess the effectiveness of the filter for turbulent event-detection applications. Wavelet transforms are a relatively recent development in applied mathematics. The subject has been receiving a great deal of attention in several different fields. A comprehen-

sive presentation of the theory can be found in Daubechies [4.6]. Applications to fluid mechanics are covered in the review article by Farge [4.7].

## 4.2 Wavelet transforms

Like the Fourier transform, the wavelet transform is obtained from the inner product of the signal under investigation with a set of analyzing functions. In the case of the Fourier transform, the analyzing functions are sines and cosines of infinite extent. The result is a mapping of global frequency content. In the case of the wavelet transform, the analyzing functions (wavelets) are dilations and translations of a "mother" function which itself is localized in the functional domain. Dilation, or contraction, results in decomposition of the signal into scales or frequencies. Translation enables the retention of time information. The limited spatial support of the wavelets means that the behavior of the signal at infinity plays no role. Thus, the wavelet transform is a means of time-scale decomposition.

The continuous wavelet transform of a function  $f(t)$  is defined as

$$\mathcal{W}_f(a, b) = |a|^{-1/2} \int f(t) \psi \left( \frac{t-b}{a} \right) dt \quad (4.1)$$

where the function  $\psi(t)$  is termed the "mother" wavelet. The scale is controlled through the parameter  $a$  while the time localization through  $b$ . As usual, if  $\psi$  is complex, its conjugate is used in forming the inner product. The inverse transform exists, and is given by

$$f(t) = C_\psi^{-1} \int \int \mathcal{W}_f(a, b) \psi^{a,b}(t) \frac{da db}{a^2} \quad (4.2)$$

where the  $\psi^{a,b}(t) = |a|^{-1/2} \psi(\frac{t-b}{a})$  are the wavelets and the constant  $C_\psi$  is given by

$$C_\psi = 2\pi \int |\mathcal{F}_\psi(\omega)|^2 |\omega|^{-1} d\omega \quad (4.3)$$

For the inverse transform to make sense,  $C_\psi$  must be finite, which leads to the admissibility condition on  $\psi$ :

$$\int \psi(t) dt = 0 \quad (4.4)$$

For the present investigation, the functions to be analyzed are discrete time series. Therefore, the discrete wavelet transform is required. This is obtained by replacing  $(a, b)$  with discrete values  $(m, n)$ , as described by Daubechies [4.6]. The discretization of the dilation parameter is straightforward:  $a = a_0^m$ . The discretization of the time parameter must be done to cover the entire range. This means that the shifts depend on the wavelet scale. Since  $a$  is a measure of the width of the wavelet, this is accomplished by letting  $b = nb_0 a_0^m$ . The values for  $m$  and  $n$  range over the

integers, and  $a_0 > 1$  and  $b_0 > 0$  are constants, which in general depend on the particular wavelet,  $\psi$ . A function  $f(t)$  is then represented by its wavelet expansion with coefficients  $C_{m,n}$  given by

$$C_{m,n} = \int f(t) \psi^{m,n}(t) dt \quad (4.5)$$

In the continuous case, the wavelet transform is highly redundant. If the wavelet functions  $\psi^{m,n}(t)$  are chosen such that they form an orthogonal basis, then the redundancies are eliminated. For this case, the smallest scale will correspond to two data points and the shifts will be integer multiples of the scale widths:  $a_0 = 2$  and  $b_0 = 1$ . The basis can then be written as

$$\psi^{m,n}(t) = \frac{1}{2^{m/2}} \psi(2^{-m}t - n2^{-m}) \quad (4.6)$$

This leads to several useful properties of the wavelet transform. In particular, analogous to Parseval's theorem for Fourier transforms, the total power is conserved:

$$\int |f(t)|^2 dt = \sum_m \sum_n |C_{m,n}|^2 \quad (4.7)$$

Fast algorithms have been developed for the computation of the orthogonal wavelet transform and its inverse. The algorithm of Press, et al. [4.8, 4.9] has been implemented for the present study. This algorithm will be referred to as the fast wavelet transform (FWT). Like the fast Fourier transform, the time series under analysis must have a length that is an integer power of two. If the total number of samples is  $2^N$ , then the wavelet expansion will also have  $2^N$  coefficients,  $C_\ell$ , with  $0 \leq \ell \leq 2^N - 1$ . The index  $\ell$  is related to the scale/time indices  $(m, n)$  by the following relationships

$$m = \begin{cases} N + 1, & \text{if } \ell = 0 \\ N - \lfloor \log_2 \ell \rfloor, & \text{if } \ell > 0 \end{cases} \quad (4.8)$$

$$n = \begin{cases} 1, & \text{if } \ell = 0 \\ \ell - 2^{\lfloor \log_2 \ell \rfloor} + 1, & \text{if } \ell > 0 \end{cases} \quad (4.9)$$

where  $\lfloor x \rfloor$  is the largest integer not exceeding  $x$ . This represents a dyadic pattern in the  $(m, n)$  plane, as illustrated in Figure 4.1. The expansion is performed at  $N$  different scales, with each scale represented by a row in the grid. For each row  $m$ , there are  $2^{N-m}$  values of the shift index,  $n$ . The index  $\ell = 0$  corresponds to what is known as the scaling function; it is roughly analogous to the dc component in a Fourier decomposition. The index  $\ell = 2^N - 1$  corresponds to the smallest scale in the analysis located at the end of the record.

Up to this point, the choice of wavelet has not been discussed. Families of orthogonal wavelets with compact support have been defined in the literature. A

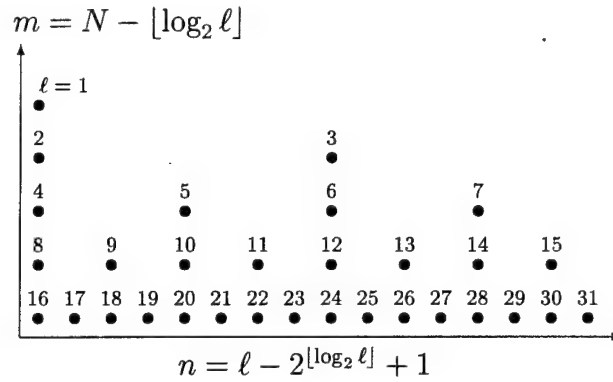


Figure 4.1: Dyadic arrangement of wavelet coefficients,  $N = 5$ .

particular family is described by a set of coefficients, called wavelet filter coefficients, which is recursively applied to the data. Guidelines for choosing a wavelet family are given, for example, by Farge [4.7]. The choice can also be automated, as is done in the “wavelet-packet” transforms utilized by Zubair [4.5]. In this method, the family is selected from a library of basis functions according to a minimum entropy criterion. The family so chosen provides the “best representation” of the data from the standpoint of data compression. Data compression is discussed further in Section 4.4.1.

Several wavelet families have been studied for the present analysis [4.10, 4.11]. The conclusion, based on extensive computations, was that turbulent event-detection results are robust with respect to the families examined. Therefore, one family of wavelets was selected and used in all subsequent work, namely, the Daubechies extremal phase set with eight coefficients [4.6, p. 195]. This family will be referred to as the D8 set. The shapes of the wavelets for four different scales and locations are illustrated in Figure 4.2. This curve was generated by performing the *inverse* wavelet transform of a vector of arbitrary length 1024 ( $N = 11$ ) consisting of all zeroes, except elements 19, 48, 110, and 243, which were set equal to one. These elements represent unit vectors in the wavelet bases. In the dyadic grid, they are located in rows 6, 5, 4, and 3, respectively. Element 19 is early in the range  $16 \leq \ell \leq 31$ , row  $m = 6$ , resulting in a wavelet positioned early in time, while element 48 is in the middle of the range  $32 \leq \ell \leq 63$ , row  $m = 5$ , resulting in a wavelet positioned near the middle of the sequence, and so forth. Notice how each successive wavelet is one half as wide as its predecessor, with an increasing amplitude such that the energy is constant.

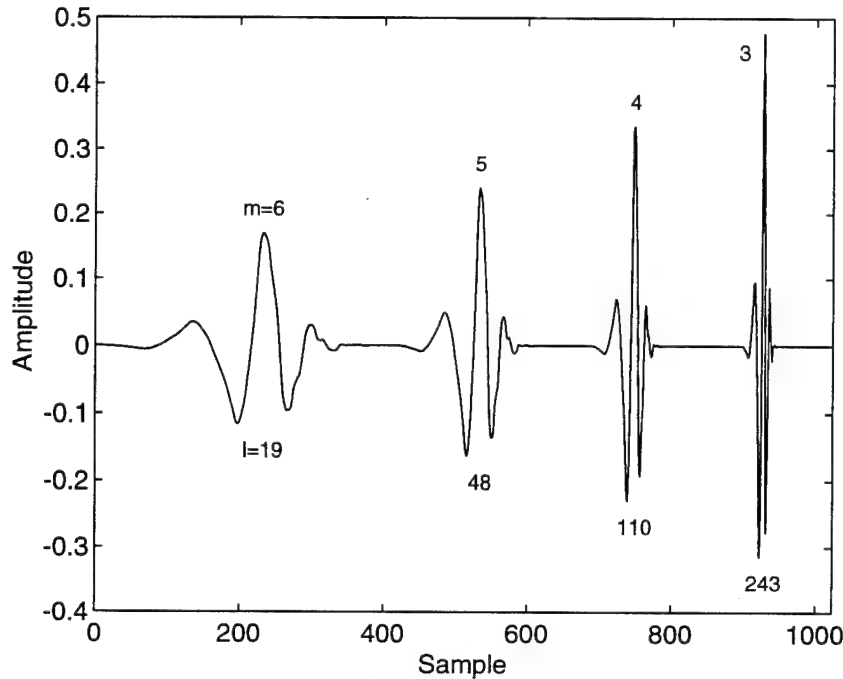


Figure 4.2: Four different scales of the Daubechies extremal phase wavelet with 8 coefficients.

### 4.3 Scale-frequency relations and wavelet power

The fast wavelet transform performs a time-scale decomposition of a signal in terms of a set of orthogonal basis functions. Before constructing a wavelet-based filter, two questions naturally arise:

1. What is the relationship between wavelet scale and conventional frequency?
2. What is an appropriate wavelet equivalent to the Fourier power spectral density?

The first question can be addressed by performing the Fourier transform of the wavelets at fixed scales. This was done by forming a wavelet from a unit vector as seen in Figure 4.2 and taking the fast Fourier transform (FFT). The conversion to Hertz depends on the sampling interval, which was equal to  $30.5 \mu s$  for this investigation. The results are illustrated in Figure 4.3 for the four smallest scales. Sequential wavelet scales are seen to contain overlapping frequency bands. However, each scale can be characterized by the frequency where the FFT magnitude is a maximum. This is termed the *center frequency*,  $f_c$ , and is tabulated in Table 4.1 for  $1 \leq m \leq 11$ . Notice how the smallest scale does not have a peak in the power spectral density (PSD), but rather a wide plateau extending to the Nyquist frequency. This



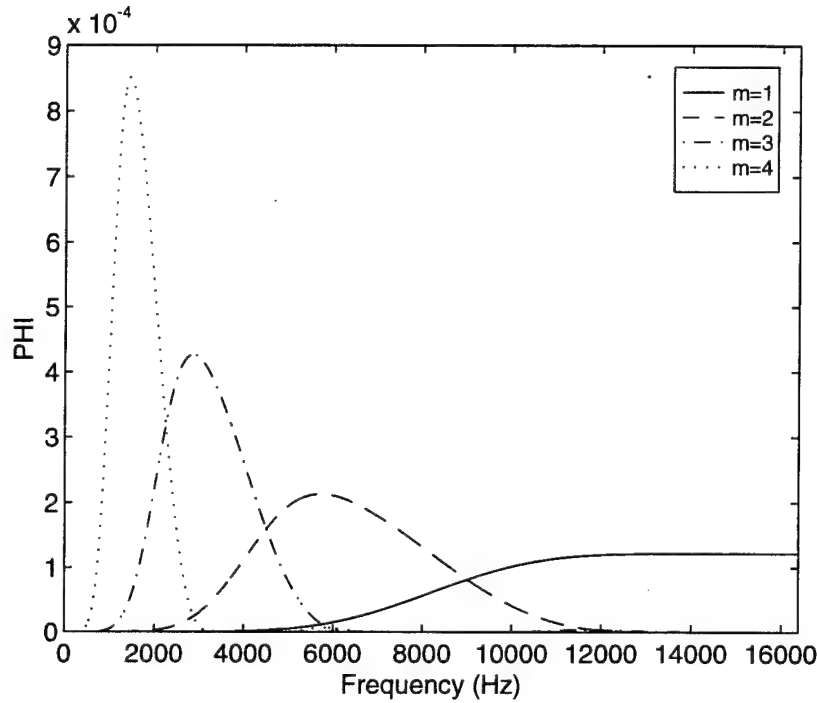


Figure 4.3: Power spectrum magnitude of the D8 wavelets at several scales for a sampling rate of 32768 Sa/s ( $\Delta t_s = 30.5 \mu s$ ).

exercise demonstrates the trade-offs between localization in frequency of the Fourier analysis and localization in scale of the wavelet analysis.

Analogous to the Fourier power spectral density is the wavelet power *scalar* density,  $\Phi^w$ , abbreviated as PScD. This can be constructed for a general function  $f$  by summing the square magnitude of the wavelet coefficients in each scale,  $m$ :

$$\Phi_f^w(m) = \sum_n C_{m,n}^2 \quad (4.10)$$

Power scalar densities of the equilibrium flow  $u$ ,  $v$ , and  $p$  time records are shown in Figure 4.4. The majority of the power for each signal is located in the scales  $2 \leq m \leq 8$ . The second peak in the wall pressure at scale  $m = 7$ , centered at 179 Hz, corresponds to extraneous noise caused by the traverse system disturbances as seen in Figure 3.18.

## 4.4 Wavelet filtering

Filtering based on the orthogonal wavelet expansion can be accomplished by modification, in some rational way, of the individual wavelet coefficients [4.5, 4.8, 4.9]. For example, setting a particular coefficient  $C_{m,n}$  equal to zero would eliminate scale  $m$

Table 4.1: D8 wavelet scales and approximate center frequencies for a sampling rate of 32768 Sa/s ( $\Delta t_s = 30.5 \mu s$ ).

Scale (row) $m$	Shift $a = 2^m$ (samples)	$f_c$ (Hz)
1	2	16384
2	4	5719
3	8	2858
4	16	1429
5	32	714
6	64	357
7	128	179
8	256	89
9	512	45
10	1024	22
11	2048	11
$\vdots$	$\vdots$	$\vdots$

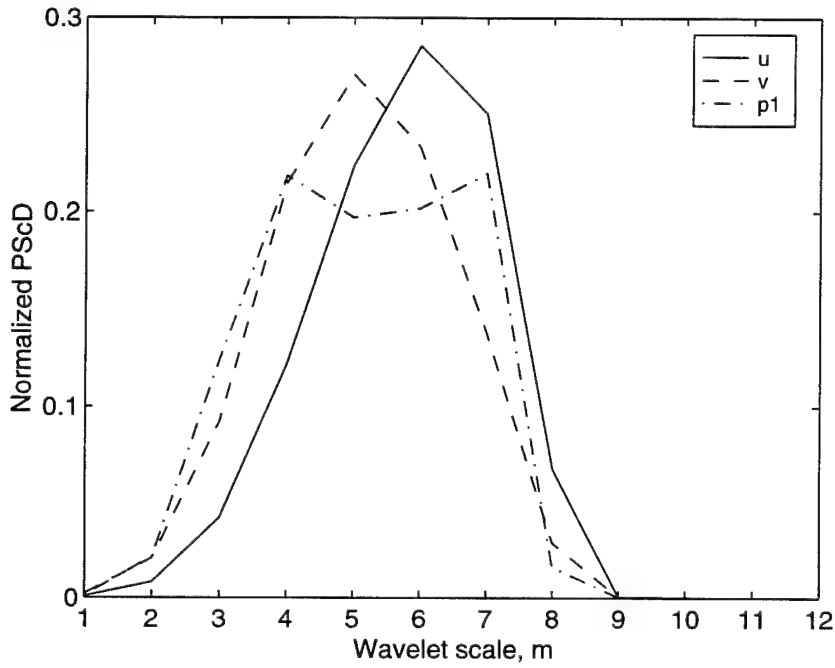


Figure 4.4: D8 power scalar densities of the equilibrium flow  $u$ ,  $v$ , and  $p$  time records at  $y/\delta = 0.02$ .

from the location  $n$ . Due to the finite support of the wavelet basis functions, other scales and locations remain unaffected.

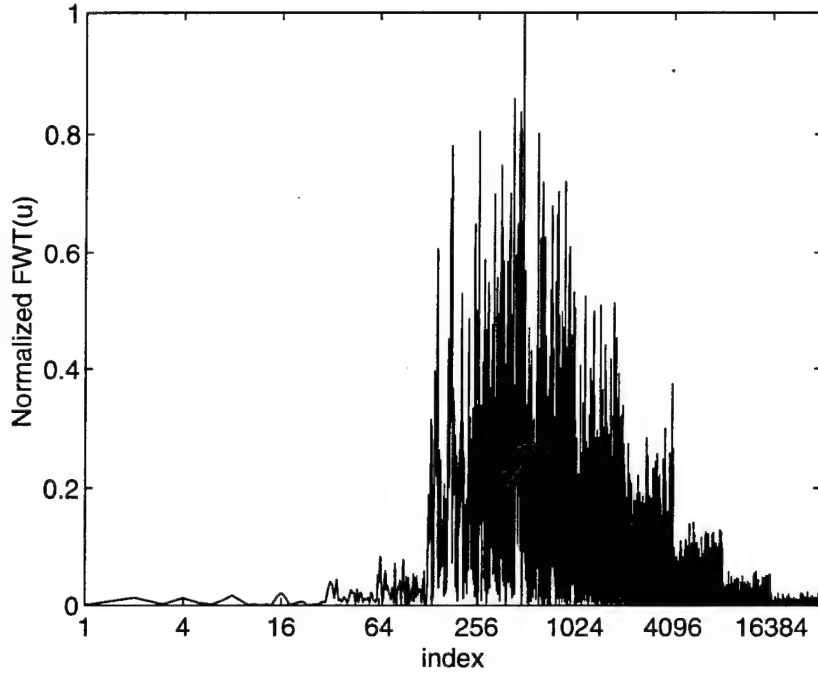


Figure 4.5: Normalized D8 FWT magnitude of a segment of the equilibrium flow  $u$  velocity at  $y/\delta = 0.02$ .

#### 4.4.1 Conventional wavelet filtering

A first-order wavelet filter can be implemented by setting to zero all coefficients with magnitude less than some threshold [4.5, 4.8–4.10]. The threshold can be set in terms of the fraction of the total signal energy to be retained in the filtered sequence, denoted by  $k_f$ . First, the signal is transformed and the resulting wavelet coefficients arranged in decreasing magnitude order. The cumulative energy is computed until it equals the desired energy fraction. All coefficients beyond this point are then set equal to zero. To construct the filtered sequence, the modified coefficients are returned to their original order and inverse wavelet transformed. For a general function  $f$ , the wavelet-filtered sequence,  $f_{wf}$ , will have energy

$$\sum f_{wf}^2 = k_f \sum f^2 \quad (4.11)$$

This filtering scheme will reject those structures contributing the least to the signal energy. The effects can be predicted by looking at the magnitude of the wavelet coefficients of a signal of interest. This is shown in Figure 4.5 for a 32768-point segment of a typical  $u$  velocity trace. The normalized magnitude of the D8 wavelet coefficients are plotted versus index,  $\ell$ . Elimination of coefficients would generally begin with the largest scales  $\ell \leq 31$ , then continue with the smallest scales  $\ell \geq 16384$ , etc. Of course, some coefficients at all scales will be eliminated based

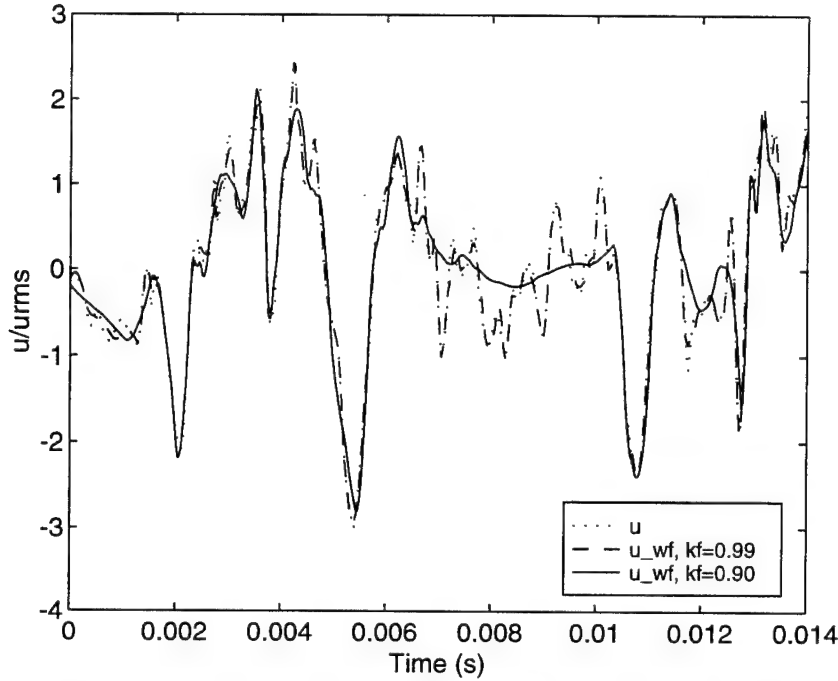


Figure 4.6: Segment of equilibrium  $u$  velocity before and after conventional wavelet filtering with  $k_f = 0.99$  and  $0.90$ .

on their magnitude. Since the signal has a zero mean, very little energy is in the largest scales. Therefore, most of the eliminated energy will come from the smallest, high-frequency scales. The conventional wavelet filter will therefore appear similar to a Fourier-based, low-pass filter.

The conventional wavelet filter highlights the data compression capabilities of the wavelet transform. This is illustrated by performing D8 conventional wavelet filtering on the equilibrium flow  $u$  velocity at location  $y/\delta = 0.02$ . A filtered sequence with  $k_f = 0.99$  can be reconstructed using only 17% of the wavelet coefficients. This represents a 6:1 compression ratio with only a 1% loss of information. If 10% of the original energy is filtered out ( $k_f = 0.90$ ), then only 5% of the wavelet coefficients are needed for reconstruction. These high compression ratios confirm that the D8 wavelets are an appropriate basis for turbulence records, as conjectured at the beginning of this chapter. Figure 4.6 shows these results in the time domain. The low-pass characteristics of the filter are evident in the  $k_f = 0.90$  case. Small-scale (high-frequency) fluctuations have been filtered out, while larger scale structures have been faithfully reproduced with no phase distortions.

### 4.4.2 Weighted wavelet filtering

In the preceding section, it was seen that conventional wavelet filtering is similar to low-pass filtering for typical turbulence quantities. A more sophisticated filter can be constructed by explicitly taking scale into account in the modification of coefficients. Several rational schemes for weighting the coefficients before selection were investigated [4.10, 4.11]. For the present application, the approach that proved to be appropriate was to first decide which scales  $m_r$  would be retained in the filtered sequence, and then assign an energy fraction for each retained scale. In terms of conventional wavelet filtering,

$$k_f = \begin{cases} k_f(m), & \text{if } m \in m_r \\ 0, & \text{otherwise} \end{cases} \quad (4.12)$$

where  $m_r$  designates the discrete set of retained scales.

Selecting which rows to retain is analogous to selecting cutoff frequencies in Fourier filtering. This was done based on the physical features of the flows and numerous computational experiments, with the major consideration being the disturbed flow data. Referring to the wall-pressure spectra in Figure 3.18, the disturbed flow exhibits excess energy in frequencies below approximately 3000 Hz. According to Table 4.1 and Figure 4.3, this range corresponds to scales  $m > 4$ , which will be eliminated. The smallest scale  $m = 1$  corresponds primarily to frequencies above  $10^4$  Hz, and contains very little energy, as seen in Figure 4.4. It will also be eliminated, leaving  $m_r = \{2\ 3\ 4\}$  for the wall pressure. The energy fractions  $k_f(m_r) = \{0.99\ 0.99\ 0.60\}$  were selected. The value  $k_f(4) = 0.60$  was chosen since scale  $m = 4$  is mostly below the spectral range of interest. The values  $k_f(2) = k_f(3) = 0.99$  were arbitrarily chosen to provide some level of data compression.

The  $u$  and  $v$  velocities were considered together. The goal is to separate passive disturbances from active turbulence production; i.e., the Reynolds stress  $-uv$ . Because of the increase in axis crossings, the  $uv$  product will exhibit higher-frequency components than either  $u$  or  $v$  separately. Therefore, the scales for  $u$  and  $v$  were increased by one relative to the wall pressure:  $m_r = \{3\ 4\ 5\}$  along with  $k_f(m_r) = \{0.99\ 0.99\ 0.99\}$ . This set of filtering parameters was designated the F2 wavelet filter, and is summarized in Table 4.2.

The effects of the F2 wavelet filter in terms of the wavelet power (Figure 4.4) are obvious; the power in each scale will be multiplied by  $k_f(m_r)$ . In the frequency domain, the effect is shown in Figures 4.7 and 4.8 for equilibrium flow  $u$  and  $p$  records. The  $v$ -velocity case is not shown, since the filtering parameters for  $u$  and  $v$  are identical. The power spectra were computed using Welch's averaged periodogram method with a window length of 1024 points and 50% overlap. At first glance, the results appear similar to a band-pass Fourier filter. However, there are several differences. The rolloffs on the low-frequency side are not as sharp as

Table 4.2: The F2 wavelet filter.

D8 discrete orthogonal wavelet expansion		
Variable	Scales retained	Power fractions
	$m_r$	$k_f(m_r)$
$u$	3	0.99
	4	0.99
	5	0.99
$v$	3	0.99
	4	0.99
	5	0.99
$p$	2	0.99
	3	0.99
	4	0.60

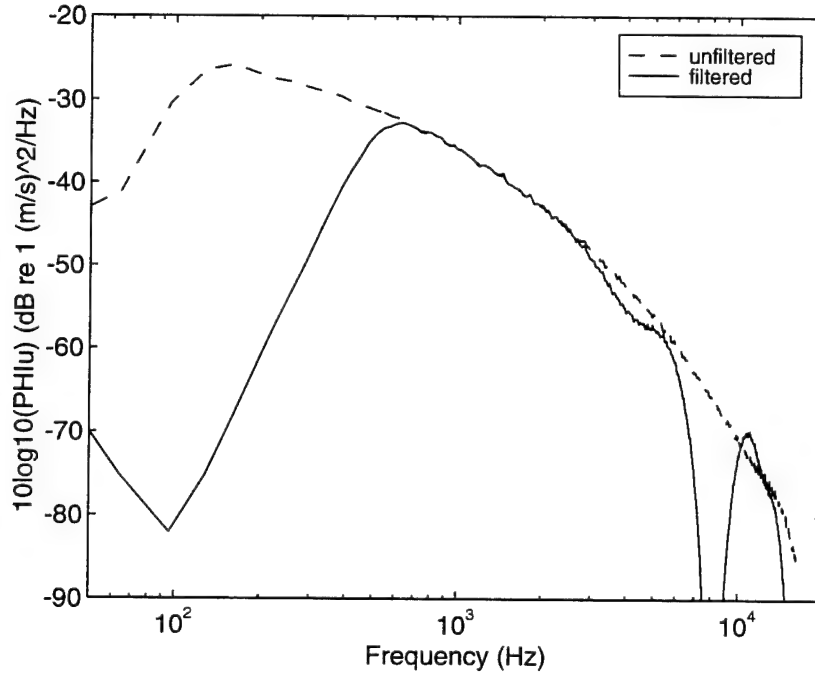


Figure 4.7: Power spectra of the equilibrium flow  $u$  velocity before and after F2 wavelet filtering.

typical Fourier filters, especially for the wall pressure where the value  $k_f(4) = 0.60$  introduces an even smoother transition. On the high-frequency side, a single cutoff frequency is not evident in either case. These features occur because wavelet scales are not localized in frequency, as was shown in Figure 4.3. Indeed, these features are difficult to replicate using conventional band-pass filters.

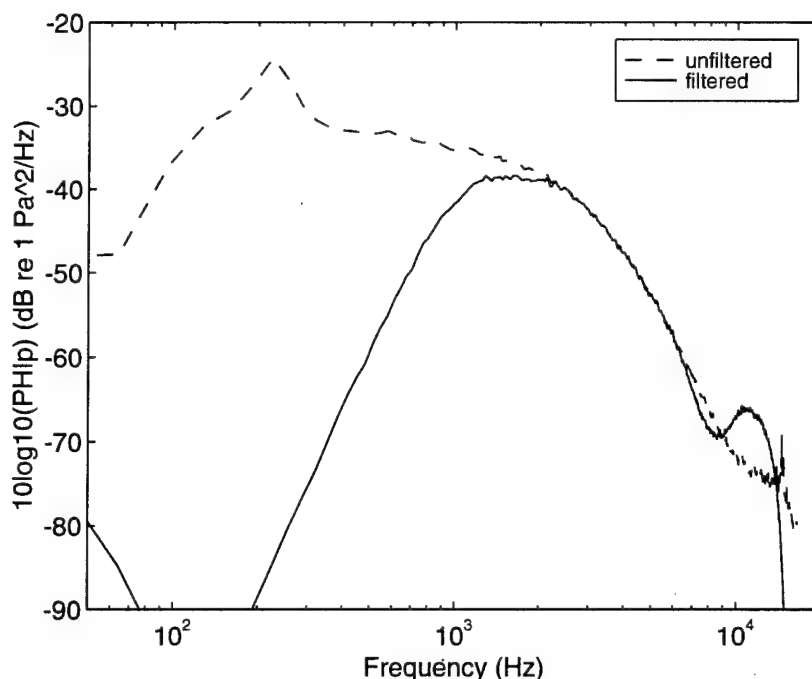


Figure 4.8: Power spectra of the equilibrium flow wall pressure before and after F2 wavelet filtering.

The effects of the filter on segments of equilibrium and disturbed flow  $u$ ,  $v$ , and  $p$  time records are illustrated in Figures 4.9 and 4.10. The features of the signals at the selected scales are left intact. For example, the large amplitude events around the time 6 ms in Figure 4.9 are reproduced, while others are filtered out. This emphasizes the ability of the wavelet transform to highlight transients in a signal. Spectral filtering, on the other hand, would attenuate all events at all locations in time.

## 4.5 Comparison of results

To evaluate the F2 wavelet filter, the peak wall pressure and quadrant event detection analyses, pursued for the unfiltered data and discussed in the previous chapter, were repeated for the wavelet-filtered equilibrium and disturbed flow data. In addition, conditional sampling was performed for both unfiltered and F2-filtered data. The aim of the conditional sampling studies was to examine the bidirectional relationship between wall pressure and near-wall organized motions [4.12–4.14], and to assess the ability of the F2 filter to preserve/enhance this relationship in the equilibrium and disturbed flow data.

Quantities that have been processed by the F2 filter will be denoted with a

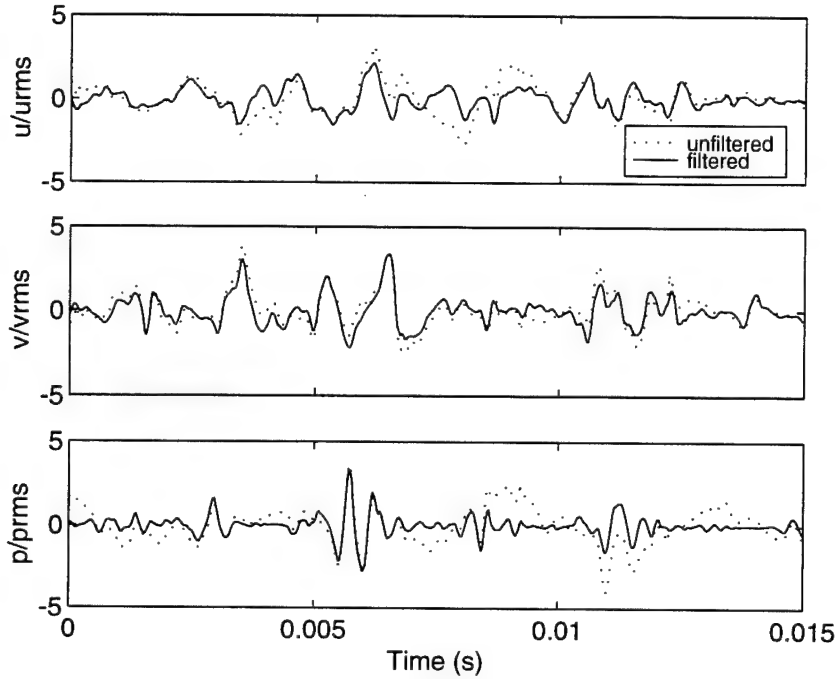


Figure 4.9: Effects of F2 wavelet filtering on equilibrium flow  $u$ ,  $v$ , and  $p_1$  at  $y/\delta = 0.02$ .

subscript  $F2$ . In keeping with the length requirements of the FWT algorithm, the first  $2^{18} = 262144$  points were used. This represents 8 s of the 10 s recorded. Thresholds were defined with respect to the *filtered* rms levels.

#### 4.5.1 Peak and quadrant event detection

Table 4.3 summarizes the results of peak-event detection performed on the equilibrium and disturbed wall pressure after F2 filtering. Comparing with Table 3.4, the numbers of events detected are increased, resulting in higher event frequencies, in spite of the shorter time record examined. This is because the rms level has been reduced by the filtering, but the amplitude of the detected events has not. The average event durations  $\Delta t^+$  have been reduced by factors of 3 to 6, with corresponding reductions in the time fractions. This indicates that large-scale structures have been filtered out. Whereas wall variable scaling collapsed the equilibrium and disturbed data before F2 filtering, that is no longer the case. Since identical filtering parameters were applied to both equilibrium and disturbed data, large amplitude events of the same physical scale (time) were retained. The difference in the statistics for the filtered data is therefore due to the difference in  $u_\tau$  (cf. Table 3.1). Average event shapes will be presented in the next section with the results of flowfield ensemble averaging conditioned on the peak wall-pressure events.



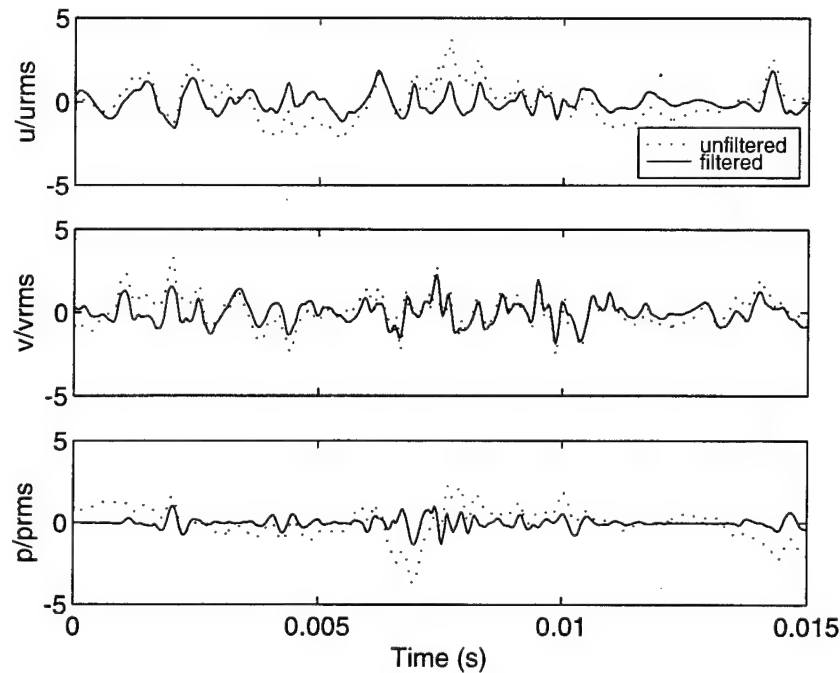


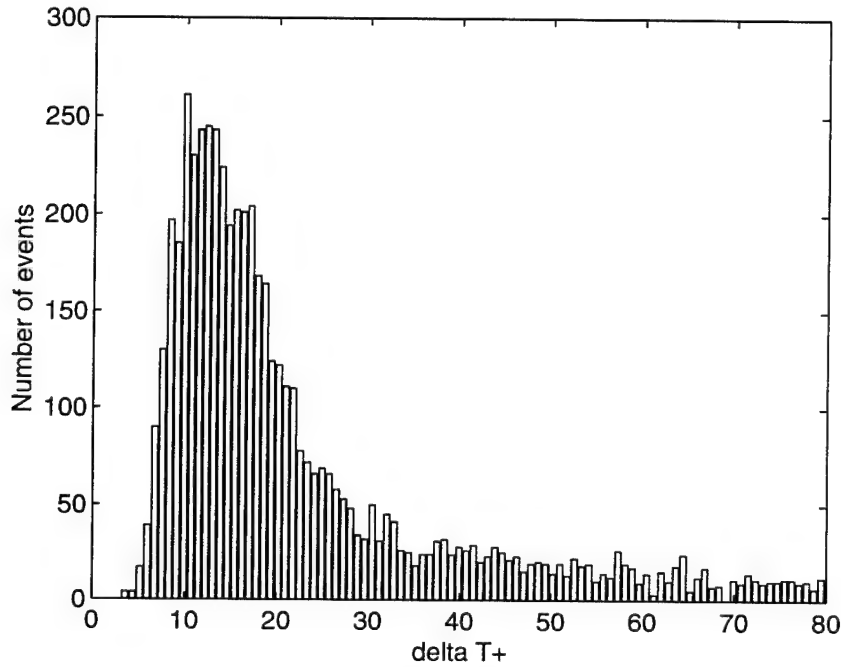
Figure 4.10: Effects of F2 wavelet filtering on disturbed flow  $u$ ,  $v$ , and  $p_1$  at  $y/\delta = 0.02$ .

Recall that though the wall-pressure event statistics collapsed before F2 filtering, the distributions of the time between events were of different character (Figures 3.23 and 3.24). This has been reversed with F2 filtering, as shown in Figures 4.11 and 4.12. The disturbed flow case now shows a log-normal distribution, similar to the equilibrium case, in place of the more uniform distribution prior to F2 filtering.

The event statistics for the F2-filtered turbulence-producing quadrant events across the boundary layers are presented in Table 4.4. Most of the observations concerning the wall-pressure events also apply to the quadrant events. The frequency of detected events has increased, while the average event durations and time fractions have decreased, again implying that large-scale structures have been filtered out. The quadrant-event frequencies across the boundary layers are shown in Figures 4.13 and 4.14. Comparing with Figures 3.29 and 3.30, the equilibrium case is relatively unchanged by the filtering; Q2 events still dominate everywhere followed by Q4 events. For the disturbed case, Q1 and Q4 events still dominate in the inner layer, and the changeover to Q2 dominance still occurs at  $y/\delta \approx 0.2$ . However, the filtering has increased the frequency of Q2 events relative to the other quadrants for  $y/\delta < 0.2$ .

Table 4.3: Wall pressure peak-event statistics for transducer  $p_1$  after F2 wavelet filtering.

$\kappa$	Time fraction	Power fraction	$\Delta t^+$	$\Delta T^+$	Number of events	Frequency per $1000t^+$
Equilibrium						
+1	<b>0.161</b>	<b>0.453</b>	<b>5.5</b>	<b>34.3</b>	<b>6111</b>	<b>29.2</b>
-1	0.161	0.463	5.5	33.8	6191	29.5
+2	<b>0.067</b>	<b>0.348</b>	<b>6.2</b>	<b>92.7</b>	<b>2261</b>	<b>10.8</b>
-2	0.068	0.359	6.1	89.9	2330	11.1
+3	<b>0.026</b>	<b>0.223</b>	<b>6.3</b>	<b>243.1</b>	<b>862</b>	<b>4.1</b>
-3	0.026	0.235	6.0	232.9	900	4.3
Disturbed						
+1	<b>0.106</b>	<b>0.475</b>	<b>3.1</b>	<b>29.1</b>	<b>3586</b>	<b>34.3</b>
-1	0.108	0.468	3.1	28.8	3623	34.7
+2	<b>0.059</b>	<b>0.423</b>	<b>3.5</b>	<b>59.5</b>	<b>1755</b>	<b>16.8</b>
-2	0.059	0.415	3.6	60.5	1724	16.5
+3	<b>0.031</b>	<b>0.336</b>	<b>3.6</b>	<b>116.6</b>	<b>895</b>	<b>8.6</b>
-3	0.030	0.324	3.7	122.1	855	8.2

Figure 4.11: Distribution of the time between equilibrium flow  $p_{wf}$  peak events,  $\kappa = 1$ .

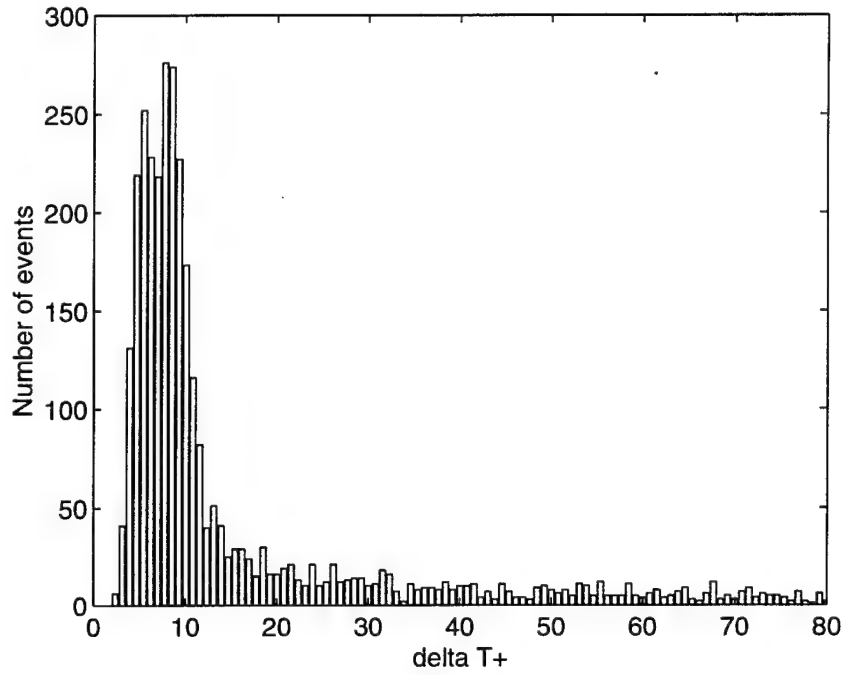


Figure 4.12: Distribution of the time between disturbed flow  $p_{wf}$  peak events,  $\kappa = 1$ .

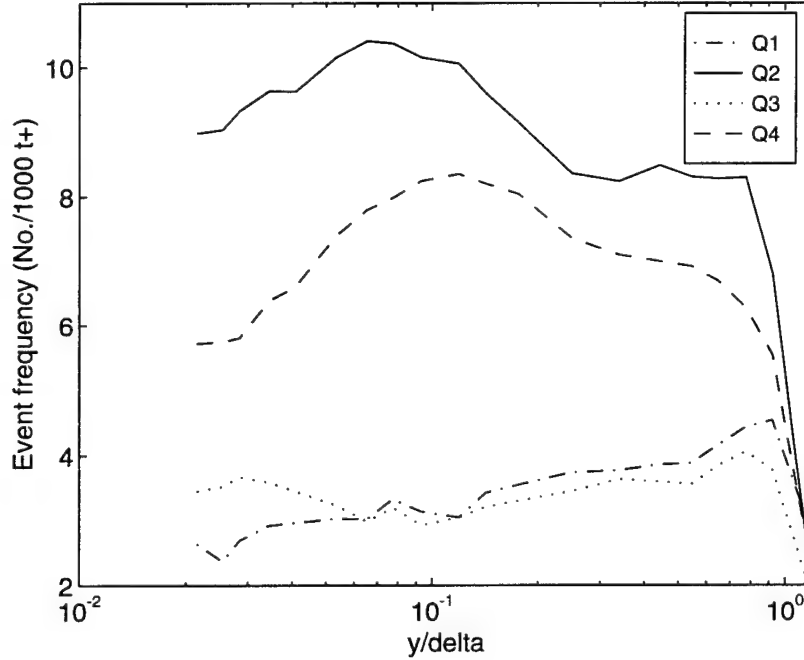


Figure 4.13: Equilibrium flow quadrant-event frequency after F2 wavelet filtering,  $\kappa = 2$ .

Table 4.4: Reynolds stress quadrant-event detection statistics after F2 wavelet filtering,  $\kappa = -2$ .

$y^+ (y/\delta)$	Time fraction	Power fraction	$\Delta t^+$	$\Delta T^+$	Number of events	Frequency per $1000t^+$
Equilibrium, quadrant 2						
25.9 (0.022)	0.073	0.435	8.14	111.24	1885	9.0
93.1 (0.077)	0.075	0.414	7.22	96.37	2175	10.4
300.0 (0.250)	0.068	0.327	8.08	119.34	1754	8.4
781.1 (0.650)	0.067	0.390	8.06	120.59	1737	8.3
Equilibrium, quadrant 4						
25.9 (0.022)	0.054	0.182	9.38	174.75	1199	5.7
93.1 (0.077)	0.063	0.215	7.90	125.23	1674	8.0
300.0 (0.250)	0.062	0.252	8.44	135.54	1543	7.4
781.1 (0.650)	0.060	0.236	9.01	149.18	1403	6.7
Disturbed, quadrant 2						
24.9 (0.020)	0.037	0.167	3.98	108.35	965	9.2
97.2 (0.077)	0.049	0.214	4.27	86.91	1200	11.5
320.2 (0.255)	0.063	0.309	3.99	63.72	1639	15.7
833.6 (0.664)	0.064	0.431	3.85	60.60	1724	16.5
Disturbed, quadrant 4						
24.9 (0.020)	0.037	0.197	3.64	99.11	1054	10.1
97.2 (0.077)	0.051	0.249	3.87	75.71	1381	13.2
320.2 (0.255)	0.060	0.247	4.24	71.07	1467	14.0
833.6 (0.664)	0.055	0.222	4.53	83.13	1258	12.0

#### 4.5.2 Conditional sampling

To assess the characteristic features of intermittent flow events, and their correlation with wall-pressure events, all flowfield variables can be ensemble-averaged over a time window based on a detection criteria for the occurrence of that event. This is known as conditional sampling. Yuan and Mokhtarzadeh-Dehghan [4.15] have recently reviewed and compared many of the methods found in the literature. In this study, conditional sampling was performed based on the detection of peak wall-pressure events and based on the detection of quadrant events. The data will be presented at the location  $y/\delta = 0.02$ . Ensemble averages, designated by  $\langle \rangle$ , were computed for  $p$ ,  $u$ ,  $v$ , and the quadrant functions  $uv_2$  and  $uv_4$ , given by

$$uv_2(t) = \begin{cases} u(t)v(t), & \text{if } u < 0 \text{ and } v > 0 \\ 0, & \text{otherwise} \end{cases} \quad (4.13)$$

$$uv_4(t) = \begin{cases} u(t)v(t), & \text{if } u > 0 \text{ and } v < 0 \\ 0, & \text{otherwise} \end{cases} \quad (4.14)$$

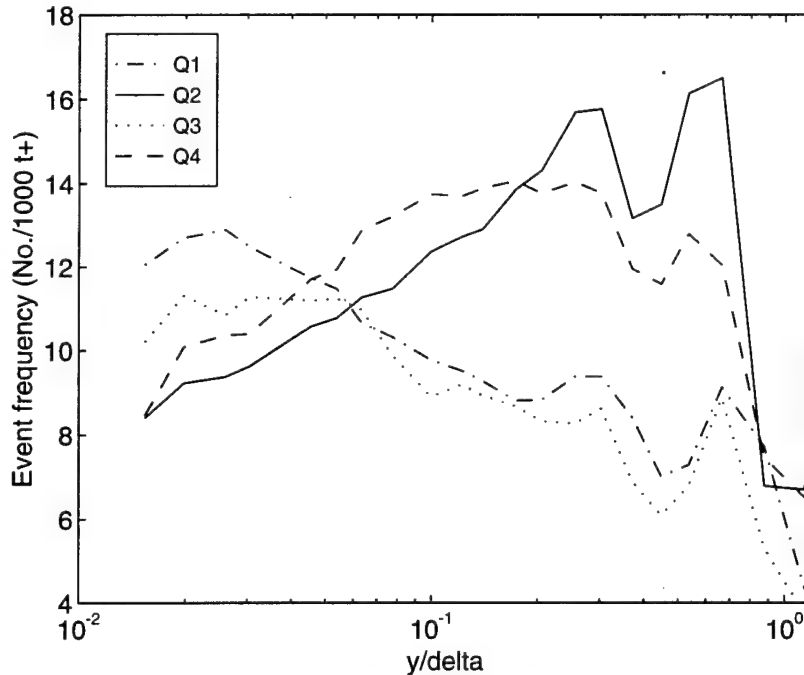


Figure 4.14: Disturbed flow quadrant-event frequency after F2 wavelet filtering,  $\kappa = 2$ .

The averages were centered about the points of peak magnitude in the detection variable. In the results to follow, the detection variable is plotted using a thicker solid line.

### Conditional sampling on $p$

Averages conditioned on the detection of peak wall-pressure events are considered first. The *equilibrium flow* results are presented in Figures 4.15 and 4.16 for the unfiltered and F2-filtered cases, respectively. The wall-pressure traces have been shifted upwards for clarity. The most notable difference is the shape of the wall-pressure event. The filtering has exaggerated the pre- and post-event dips. This effect is responsible for the shorter average-event durations. In both cases, significant correlation is seen in the flowfield variables. The  $u$  velocity increases while the  $v$  velocity decreases, moving from Q2 to Q4. The trends are somewhat intensified after filtering.

The *disturbed flow* results are shown in Figures 4.17 and 4.18. In the unfiltered case, the  $v$  velocity remains flat over the first half of the pressure event, with a sharp decrease after the pressure peak. Relative to the equilibrium results, this produces no correlation with Q2 events and exaggerated correlation with Q4 motions. However, the F2 filter recovers the  $v$  and  $uv_2$  correlations seen in the filtered equilibrium flow

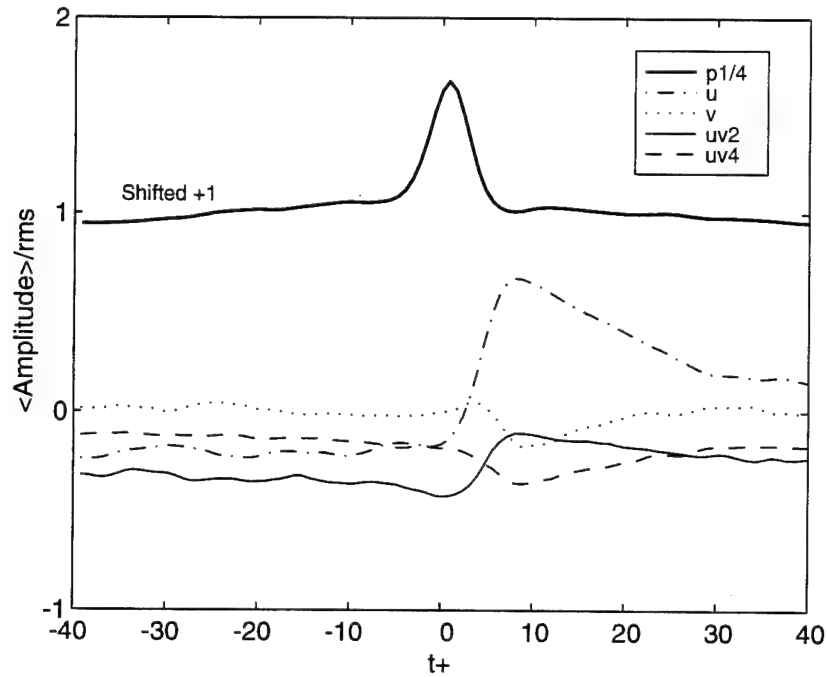


Figure 4.15: Ensemble averages conditioned on peak wall-pressure events with  $\kappa = 2$ . Equilibrium flow at  $y/\delta = 0.02$  before filtering.

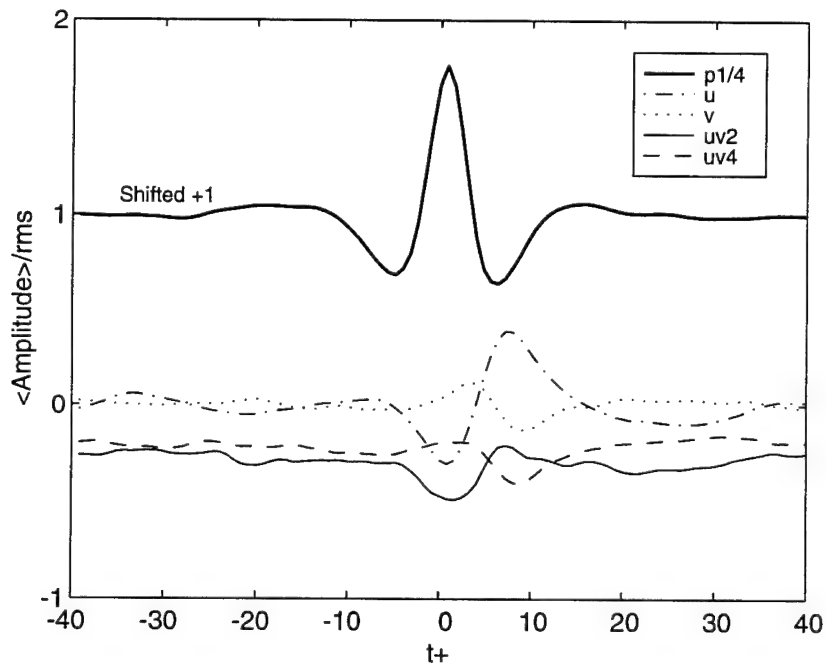


Figure 4.16: Ensemble averages conditioned on peak wall-pressure events with  $\kappa = 2$ . Equilibrium flow at  $y/\delta = 0.02$  after F2 filtering.

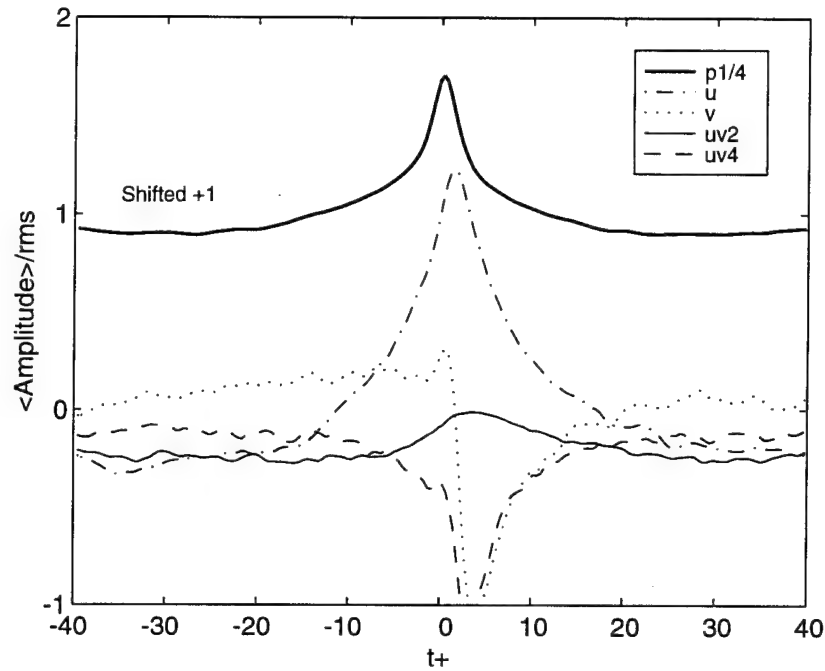


Figure 4.17: Ensemble averages conditioned on peak wall-pressure events with  $\kappa = 2$ . Disturbed flow at  $y/\delta = 0.02$  before filtering.

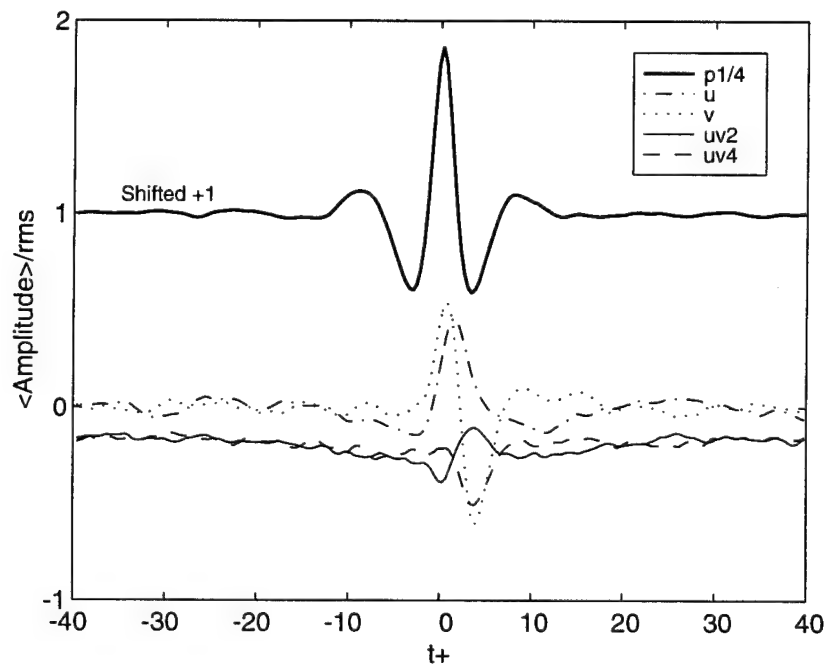


Figure 4.18: Ensemble averages conditioned on peak wall-pressure events with  $\kappa = 2$ . Disturbed flow at  $y/\delta = 0.02$  after F2 filtering.

data. The structures are narrower when normalized by viscous time units, for the reasons noted previously. The filtering appears to capture the generic features of the near-wall structure.

### Conditional sampling on $uv_2$

Conditional sampling results based on the Q2 Reynolds stress events are shown in Figures 4.19 and 4.20 for the equilibrium flow and Figures 4.21 and 4.22 for the disturbed flow. The *equilibrium flow* results confirm the  $p-uv_2$  correlation shown in the results based on peak wall pressure. That is, Q2 motions, where the flow slows and moves away from the wall, coincide with local increases in the wall pressure. Like the peak wall-pressure results, F2 filtering enhances this correlation; the wall-pressure signature is stronger than for the unfiltered data. Also similar to the peak wall-pressure results, F2 filtering produces pre- and post-peak oscillations in the detection variables  $u$  and  $v$ .

Looking at the quadrant detection results for the *disturbed flow* in Figures 4.21 and 4.22, it can be seen that before filtering, the wall-pressure signature appears primarily as a decrease prior to the Q2 event, with an increase back to a zero level at the time of peak Reynolds stress. The F2 filter, however, recovers the behavior seen in the equilibrium results. Again, the ensemble averaged structures are made narrower by filtering.



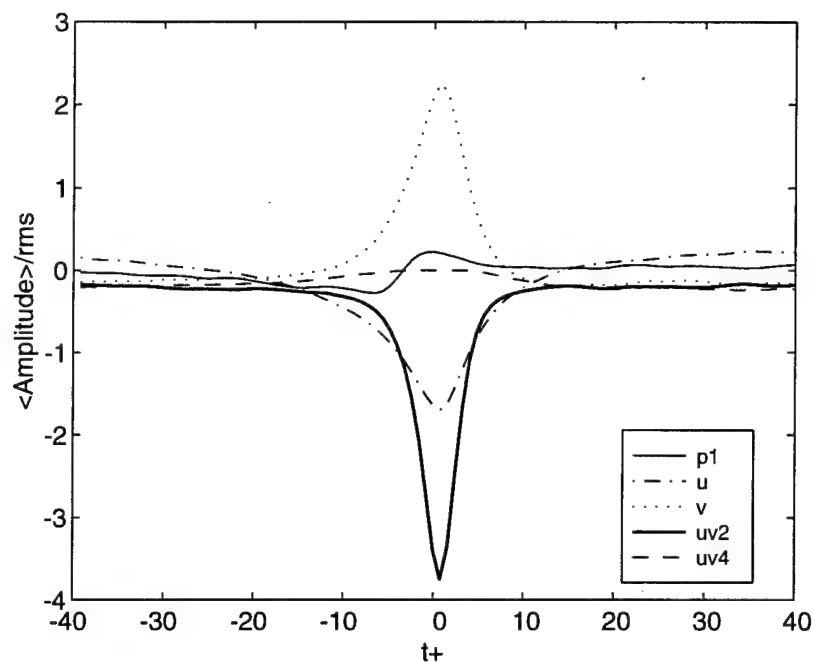


Figure 4.19: Ensemble averages conditioned on peak Q2 events with  $\kappa = 2$ . Equilibrium flow at  $y/\delta = 0.02$  before F2 filtering.

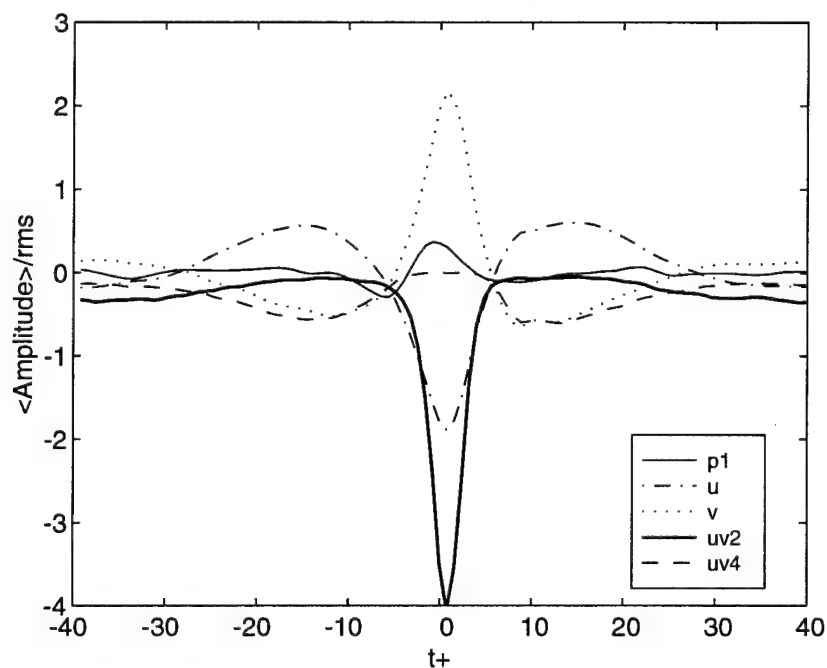


Figure 4.20: Ensemble averages conditioned on peak Q2 events with  $\kappa = 2$ . Equilibrium flow at  $y/\delta = 0.02$  after F2 filtering.

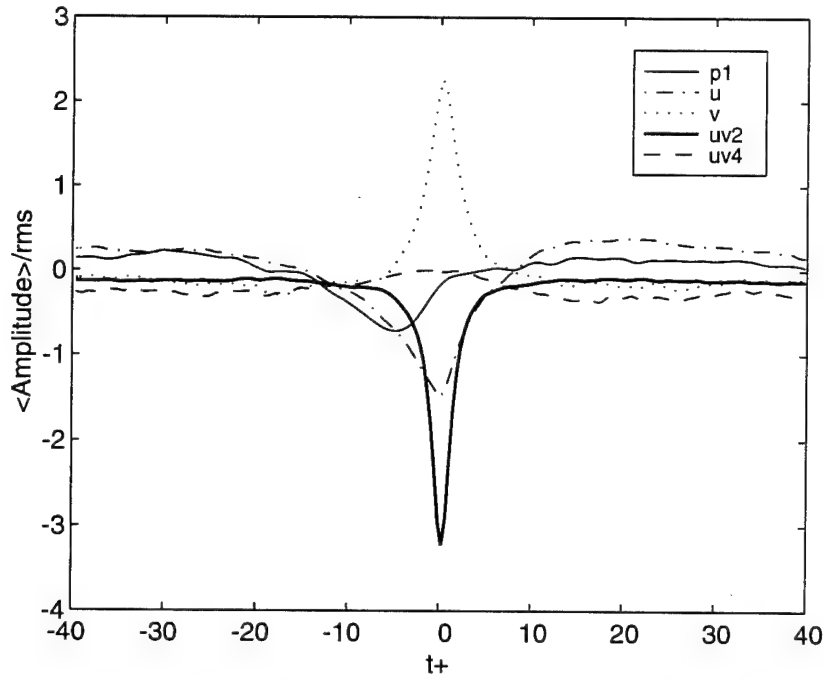


Figure 4.21: Ensemble averages conditioned on peak Q2 events with  $\kappa = 2$ . Disturbed flow at  $y/\delta = 0.02$  before F2 filtering.

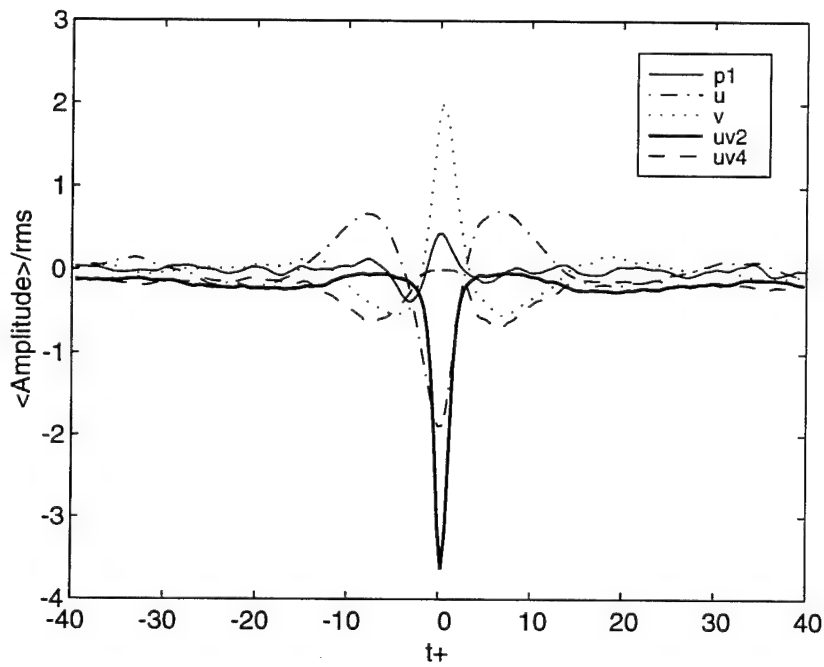


Figure 4.22: Ensemble averages conditioned on peak Q2 events with  $\kappa = 2$ . Disturbed flow at  $y/\delta = 0.02$  after F2 filtering.

## 4.6 Summary

The F2 wavelet filter preserves a range of physical scales. The scales retained are analogous to the selection of cutoff frequencies in a Fourier bandpass filter. For the present application, the scales were chosen to be representative of near-wall structures in equilibrium turbulent boundary layers.

Four sets of databases were examined: unfiltered equilibrium, unfiltered disturbed, filtered equilibrium, and filtered disturbed. Two issues warrant consideration. First, for the equilibrium flow data, what are the effects, if any, of wavelet filtering? Second, for the disturbed flow data, have the generic features of the near-wall flow structures been captured by the filtering strategy? The latter question is based on the hypothesis that the near-wall turbulent structure is weakly affected by the outer-layer disturbances, as evident in the data presented in Chapter 3.

The following observations answer these questions with regard to the performance of the F2 wavelet filter:

- *F2 filtering retained the essential features of the near-wall motions in the equilibrium flow and recovered these features to a limited extent in the disturbed flow results.* By reducing overall energy levels and retaining only certain scales, F2 filtering increases the number and decreases the duration of detected events. However, the log-normal distribution of the time between peak wall-pressure events was preserved for the equilibrium flow and recovered for the disturbed flow. In the same way, the relative contributions of the four quadrants to the Reynolds stress was preserved for the equilibrium flow, while the disturbed flow results were improved over the unfiltered data.
- *F2 filtering recovered the bidirectional relationship between wall pressure and Q2 uv events in the disturbed flow.* The correlation between wall pressure and Q2 flow events, clearly seen in the equilibrium boundary layer, is not evident in the original disturbed flow data. F2 filtering recovers this link. This is an important finding, which will be expanded upon in the next chapter. The fact that the recovered structures correspond to the scales retained in the wavelet expansion does not account for the alignment of these structures in time. This alignment is indicative of the physical processes occurring within the turbulent boundary layer.

In light of these findings, the F2 filter will be employed for the remainder of the investigation, and results can be assumed to have been obtained from F2-filtered data unless specified otherwise.

## References

- [4.1] H. Eckelmann. A review of knowledge on pressure fluctuations. In Kline and Afgan, editors, *Near-Wall Turbulence: Proceedings of the 1988 Zoran Zaric Memorial Conference*, pages 328–347. Hemisphere, 1990.
- [4.2] Y. Kobashi and M. Ichijo. Wall pressure and its relation to turbulent structure of a boundary layer. *Experiments in Fluids*, 4:49–55, 1986.
- [4.3] A. M. Naguib and C. E. Wark. An investigation of wall-layer dynamics using a combined temporal filtering and correlation technique. *J. Fluid Mech.*, 243:541–560, 1992.
- [4.4] H. Tennekes and J. L. Lumley. *A First Course in Turbulence*. The MIT Press, 1972.
- [4.5] L. M. Zubair. *Studies in Turbulence Using Wavelet Transforms for Data Compression and Scale Separation*. PhD thesis, Yale University, 1993.
- [4.6] I. Daubechies. *Ten Lectures on Wavelets*. Society for Industrial and Applied Mathematics, 1992.
- [4.7] M. Farge. Wavelet transforms and their applications to turbulence. *Annu. Rev. Fluid Mech.*, 24:395–457, 1992.
- [4.8] W. H. Press, S. A. Teukolsky, W. T. Vetterling, and B. P. Flannery. *Numerical Recipes in C*. Cambridge University Press, 1992.
- [4.9] W. H. Press, S. A. Teukolsky, W. T. Vetterling, and B. P. Flannery. *Numerical Recipes in FORTRAN*. Cambridge University Press, 1992.
- [4.10] P. B. Penafiel, M. J. Casarella, and M. E. Kammeyer. Application of wavelet-filtering techniques to intermittent turbulent and wall pressure events, part I — exploratory results. Technical report, Dept. of Mech. Engineering, The Catholic University of America, Washington, D.C. 20064, 1994.
- [4.11] P. B. Penafiel, M. J. Casarella, and M. E. Kammeyer. Application of wavelet-filtering techniques to intermittent turbulent and wall pressure events, part II — detection of cluster patterns. Technical report, Dept. of Mech. Engineering, The Catholic University of America, Washington, D.C. 20064, 1995.
- [4.12] V. Wilczynski. *Organized Turbulent Structures and Their Induced Wall Pressure Fluctuations*. PhD thesis, The Catholic University of America, 1992.
- [4.13] J. H. Haritonidis, L. S. Gresko, and K. S. Breuer. Wall pressure peaks and waves. In Kline and Afgan, editors, *Near-Wall Turbulence: Proceedings of the 1988 Zoran Zaric Memorial Conference*, pages 397–417. Hemisphere, 1990.

- [4.14] A. V. Johansson, J. Her, and J. H. Haritonidis. On the generation of high-amplitude wall pressure peaks in turbulent boundary layers and spots. *J. Fluid Mech.*, 175:119–142, 1987.
- [4.15] Y. Yuan and M. Mokhtarzadeh-Dehghan. A comparison study of conditional-sampling methods used to detect coherent structures in turbulent boundary layers. *Phys. Fluids*, 6(6):2038–2057, 1984.

## Chapter 5

### Detection of event cluster patterns

#### 5.1 Introduction

The conditional sampling results of the previous chapter showed a correlation between wall-pressure events and flowfield structure in the form of accelerating  $u$ -velocity or second-quadrant  $uv$  events. A more careful examination of the results conditioned on peak wall pressure in Figures 4.15–4.18 reveals that the streamwise velocity is accelerating from negative to positive values while the wall-normal velocity is decelerating from positive to negative. In other words, a motion from the second to the fourth  $u$ - $v$  quadrant, or a Q2-Q4 event pair. Looking at the filtered results conditioned on Q2 events in Figures 4.20 and 4.22, Q4 motions are evident on either side of the primary Q2 event; i.e., a Q4-Q2-Q4 event triple. These observations suggest that detection of flowfield structure based on event groupings, or *clusters*, may provide a clearer picture than detection based on single events. Therefore, an algorithm is required to identify clusters of events.

Another issue merits attention, namely event magnitude. Event-detection methods identify those portions of a signal that satisfy the detection criteria, which usually includes comparing some signal property against a threshold value. For example, the peak and quadrant event-detection methods require that the signal amplitude exceed a certain level. Another common technique, the VITA method, requires that the local variance of the signal exceed a given threshold. The threshold therefore discriminates events based on magnitude or strength. Selection of the threshold value is, however, somewhat arbitrary, being based primarily on experience. Also, these algorithms ignore the fact that the strength of an event is not solely dependent on the amplitude of the phenomena causing it, but also on the relative spatial locations.

The above considerations demonstrate the need for a detection algorithm that can capture cluster patterns of events without prescribing an amplitude threshold level. The idea of event clusters is not entirely new. Wilczynski [5.1], also using peak-event detection, observed Q2-Q4 event pairs in an equilibrium TBL, while Guezennec [5.2] showed that the VITA technique, with appropriate alignment, detected the shear layer between Q2-Q4 flow patterns. However, the development of

detection algorithms based on the cluster concept is apparently without precedent. This chapter will examine two methods to identify the groupings:

1. Localized Variance Technique.
2. Localized Windowed Peak Detection Technique.

## 5.2 Detection techniques

### 5.2.1 Localized variance technique

As a first attempt at identifying event clusters, a variation of the VITA method mentioned above was explored. The VITA method [5.3, 5.4] computes the local variance of a signal, which for an arbitrary function  $f(t)$  is defined as

$$\mathcal{V}\{f\} = \mathcal{V}_f(t, T_v) = \frac{1}{T_v} \int_{t-\frac{T_v}{2}}^{t+\frac{T_v}{2}} f^2(\tau) d\tau - \left\{ \frac{1}{T_v} \int_{t-\frac{T_v}{2}}^{t+\frac{T_v}{2}} f(\tau) d\tau \right\}^2 \quad (5.1)$$

where  $T_v$  is an adjustable short integration time that can be interpreted as the typical duration of the event. An event is detected when

$$\mathcal{V}_f(t, T_v) \geq \kappa f_{rms}^2 \quad (5.2)$$

The VITA method is almost always applied to the streamwise velocity. Since burst events characterized by large Q2 and Q4 events are of primary interest, the VITA approach was applied to the  $uv(t) = u(t)v(t)$  time record. Since it is also desired to retain the pattern of these burst events and to correlate them with the wall-pressure events, contiguous  $\mathcal{V}$  time records for  $uv(t)$  and  $p(t)$  were computed. Thus, the local variance records  $\mathcal{V}_p(t)$  and  $\mathcal{V}_{uv}(t)$  were generated from the original time records. The application of the VITA approach to  $uv$  and  $p$  in this way is referred to as the localized variance (LVAR) technique.

The VITA method locates regions of large time derivative whose durations are approximately equal to the short-time averaging period  $T_v$  [5.4]. In this sense, VITA is reminiscent of a wavelet filter with fixed scale. For this study, the value  $T_v = 12$  samples was chosen to reflect the scales retained in the F2 wavelet filter (cf. Tables 4.1 and 4.2). In nondimensional terms, this equates to  $T_v^+ = 9.6$  for the equilibrium flow, which is in the range of values used by other researchers [5.5–5.7]. For the disturbed flow,  $T_v^+ = 4.8$ .

The correspondence of the local variance with  $T_v = 12$  samples with the F2 wavelet filter is illustrated in Figures 5.1 and 5.2. These figures show segments of original and F2-filtered wall-pressure signals and their corresponding  $\mathcal{V}$  functions for the equilibrium and disturbed boundary layers, respectively. The event clusters identified by the LVAR time window in the unfiltered data correspond to the flow structures retained in the F2-filtered data.

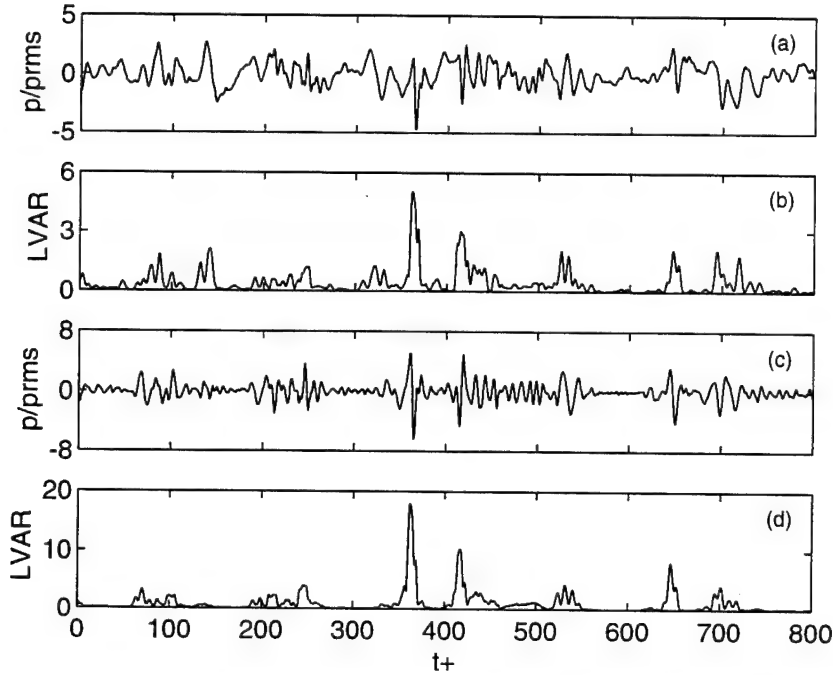


Figure 5.1: Equilibrium wall pressure and localized variance with  $T_v^+ = 9.6$ . (a), (b) Prior to F2 filtering. (c), (d) After F2 filtering.

Similar results were obtained for the  $uv$  time records. Thus, the LVAR technique appears to be a simple alternative to the wavelet filter. However, locating the individual clusters would require querying the  $\mathcal{V}$  function, thus introducing a threshold level similar to the VITA method. Therefore,  $\mathcal{V}$  functions offer no advantage over other threshold techniques for conditional sampling. Also, since the LVAR function is positive-definite, discrimination of positive and negative events must be done by returning to the original time records. However, this property means that correlation computations will be enhanced if conducted on  $\mathcal{V}$  functions instead of the signals themselves. The use of  $\mathcal{V}$  functions in correlations will be discussed in Section 5.3.

### 5.2.2 Localized windowed peak-detection technique

A new algorithm, called Localized Windowed Peak Detection (LWPD), was developed that captures the cluster patterns of peak events while being independent of a magnitude threshold. The method is based on the conjecture that the events of interest are the largest peaks in the event clusters.

The algorithm is described as follows for a sequence  $s = \{s_1 \dots s_N\}$  sampled at discrete times  $t = \{t_1 \dots t_N\}$ :

1. Find the local maxima,  $P$ , of  $s$  at times  $t_n = \{t_{n_1} \dots t_{n_P}\}$ . Define the event start/end as the local minima immediately preceding/following each peak.



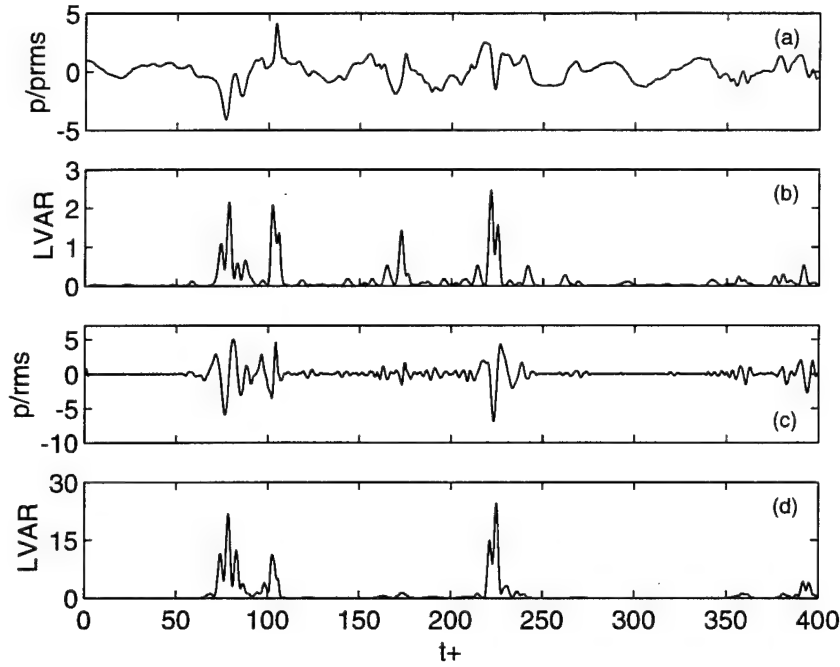


Figure 5.2: Disturbed wall pressure and localized variance with  $T_v^+ = 4.8$ . (a), (b) Prior to F2 filtering. (c), (d) After F2 filtering.

2. Sequentially compare each  $P_n$  with its neighbors and compute the times between peaks  $\Delta t_+ = t_{n_{i+1}} - t_{n_i}$  and  $\Delta t_- = t_{n_i} - t_{n_{i-1}}$ . Retain peaks from  $P$  to form a new subset of peaks,  $P'$ , if one of the following conditions is met:
  - (a) *A peak is itself a local maximum of  $P$ .* Let the start point be equal to the end point of the preceeding (now eliminated) peak and let the end point be equal to the start point of the following (now eliminated) peak.
  - (b) *A peak is isolated on only one side such that  $\Delta t_+ \geq T_w$  or  $\Delta t_- \geq T_w$ , and it is a local maximum within the window  $T_w$ .* If it is isolated from the next peak ( $\Delta t_+ \geq T_w$ ), let the start point be equal to the end point of the preceeding (now eliminated) peak. If it is isolated from the preceeding peak ( $\Delta t_- \geq T_w$ ), let the end point be equal to the start point of the following (now eliminated) peak.
  - (c) *A peak is isolated on both sides such that  $\Delta t_+ \geq T_w$  and  $\Delta t_- \geq T_w$ .* The start/end points remain unchanged.
3. If  $P' = P$ , i.e. if no peaks have been eliminated, stop. Otherwise, let  $P = P'$  and iterate from step 2.

A complete listing of the LWPD code is contained in appendix C. The final output contains the location of the largest peak within each cluster and the duration of

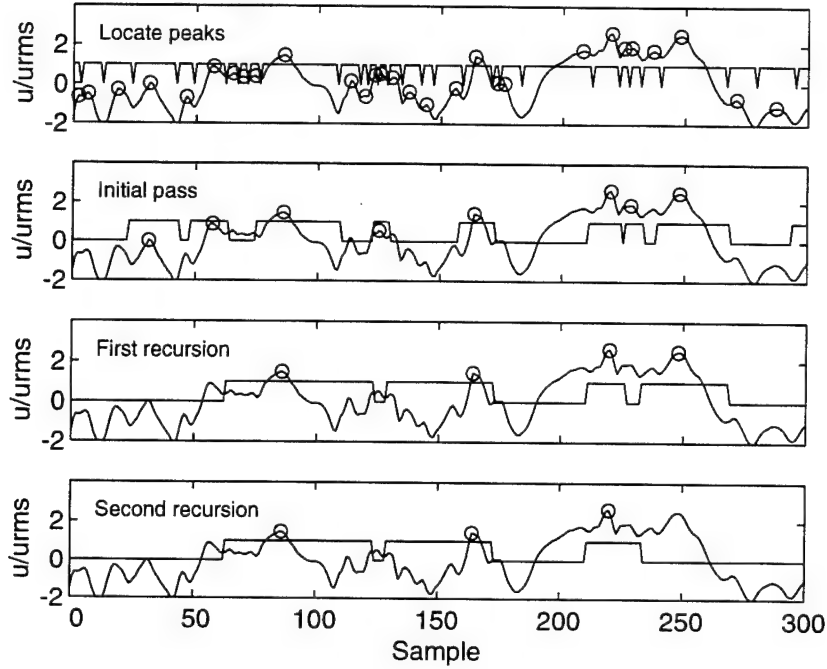


Figure 5.3: Localized windowed peak detection with  $T_w = 50$  samples.

each individual cluster. The time window,  $T_w$ , is the only adjustable parameter of the algorithm. It specifies the minimum time between successive peaks in a sequence. Without this parameter, the “peak of the peaks” operation, step 2a, would eventually eliminate all points except the maximum peak in  $s$ . This algorithm is more computationally intense than the traditional peak level detection algorithm, but surprisingly robust for a wide range of random-like time records.

The LWPD process is illustrated in Figure 5.3 for a segment of  $u$ -velocity from the equilibrium TBL at  $y/\delta = 0.02$ . A time window equal to 50 samples or  $40t^+$  was used. Circles mark the peaks retained after each step. The step functions show the evolution of the cluster indicator functions based on the cluster beginning and end points. The initial pass retains only “peaks of the peaks,” with the window criteria coming into play in the subsequent passes. Three event clusters are indicated in the segment shown.

The final cluster indicator functions merit further attention. The durations of the first two clusters appear to be roughly correct, if not in optimum alignment. The indicator function for the third event, while centered on the peak, appears too short. It is concluded from this limited sampling of the data that the definition of event start/end points needs further testing and possibly some refinements. Therefore, event duration results from the LWPD algorithm should be viewed with some caution.

These results can be contrasted with traditional peak-event detection with a

Table 5.1: LWPD statistics for positive wall pressure peaks with  $T_w = 75$  samples.

Case	$T_w^+$	$\Delta t^+$	$\Delta T^+$	Number of clusters	Frequency per s	Frequency per $1000t^+$
ETBL	60	47.3	112.0	2334	234.1	8.9
ETBL, F2	60	47.7	112.4	1866	233.3	8.9
DTBL	30	22.5	56.0	2327	233.4	17.9
DTBL, F2	30	24.2	57.1	1831	228.9	17.5

magnitude threshold  $\kappa = 2$ . The traditional method would rigidly exclude the peaks at points 86 and 164, which have magnitudes of approximately  $1.5u_{rms}$ . Instead, it would identify only the peak at sample 220. In addition, if there were a zero crossing between the peaks at samples 220 and 248, both would be identified by traditional peak-event detection. Ensemble averaging over a time interval greater than about 20 samples would then include these peaks twice in different relative temporal locations. By aligning ensemble averages on the largest peak in each event cluster, this type of duplication can be minimized.

The single parameter  $T_w$  determines statistical properties such as number of events, average duration, and average time between cluster patterns. It is important to note that the number of cluster patterns detected by the LWPD technique is mainly governed by  $T_w$ , with weak dependence on the distinct features of the time record. This can be understood if one considers a signal that has large amplitude clusters separated by periods of relatively low amplitude activity. If  $T_w$  is less than the time between large amplitude clusters, the LWPD algorithm will still locate the largest peak in this interval. It is just that such a cluster will have a smaller impact on correlations or ensemble averages based on the detected clusters. This characteristic of the LWPD technique was exploited by defining the same time window value  $T_w$  for both  $uv$  and  $p$  time records. This insured conformity in the number of events for both records. The particular choice of  $T_w$  was based on maximizing the correlation between concurrent events, which is discussed in Section 5.3. The bounds for this number, established from extensive computations on the equilibrium time records, are  $40 \leq T_w^+ \leq 120$  ( $50 \leq T_w \leq 150$  data samples).

The value of  $T_w = 75$  samples, was chosen for the equilibrium data ( $T_w^+ = 60$ ) based on numerous test cases and applied also to the disturbed flow data ( $T_w^+ = 30$ ). The resulting cluster statistics for the positive wall pressure peaks are displayed in Table 5.1. Using the same physical value for  $T_w$  for both flows results in equivalent statistics in physical terms, as evidenced by the number and frequency of physical clusters detected. Recall that the F2-filtered time records are 8-s long compared with 10 s for the unfiltered data. In nondimensional terms, the statistics directly reflect the factor of two difference in viscous time scales. Comparing with Table 3.4, the equilibrium LWPD statistics are equivalent to peak-event detection results for a threshold between 1 and 2, while the disturbed flow statistics are equivalent to

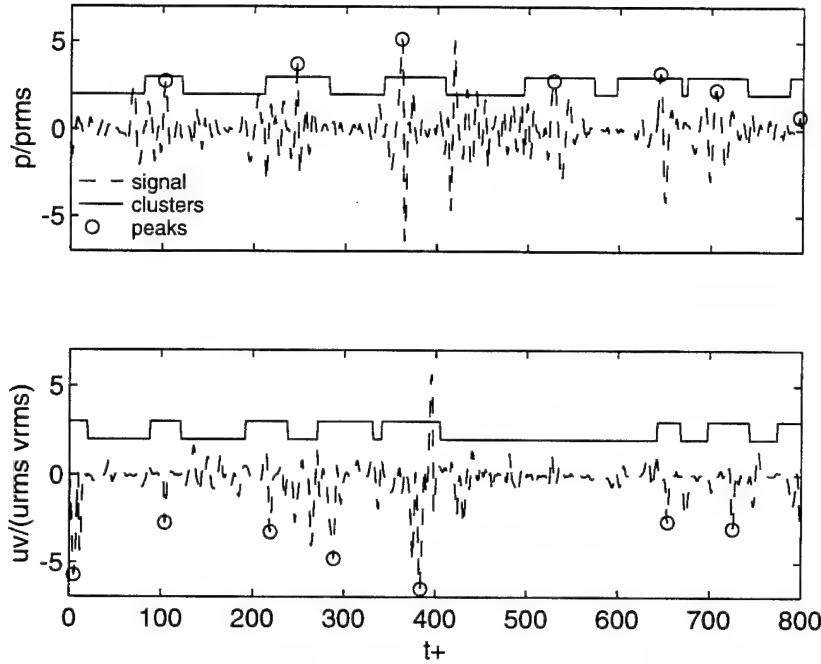


Figure 5.4: LWPDP cluster detection on equilibrium  $p_{F2}$  and  $uv_{F2}$  with  $T_w^+ = 60$ .

a threshold equal to 1. In both cases, the LWPDP durations are longer, reflecting clusters rather than individual events.

Using this window size, results for F2-filtered equilibrium and disturbed wall pressure and Reynolds stress are shown in Figures 5.4 and 5.5, respectively. The indicator functions marking the cluster beginning and end points are shown shifted upwards for clarity. The clusters were obtained by applying the LWPDP algorithm to the positive peaks for the pressure and to the negative peaks for the Reynolds stress. The time segments are the same as those in Figures 5.1 and 5.2 illustrating the LVAR technique. Comparing with these figures, one sees that there is good correspondence between LWPDP clusters and increased local variance. Cluster time records will be denoted by a subscript  $cl$ , and are defined as the (F2-filtered) time records multiplied by the LWPDP indicator function:

$$f_{cl}(t) = f_{F2}(t) \cdot I_{LWPDP}(t) \quad (5.3)$$

where

$$I_{LWPDP}(t) = \begin{cases} 1, & \text{if cluster start} < t < \text{cluster end} \\ 0, & \text{otherwise} \end{cases} \quad (5.4)$$

### 5.3 Correlation of clusters

Correlations were performed on three time records: original data,  $\mathcal{V}$  functions, and LWPDP clusters [5.8]. These correlations were computed between the two spatially

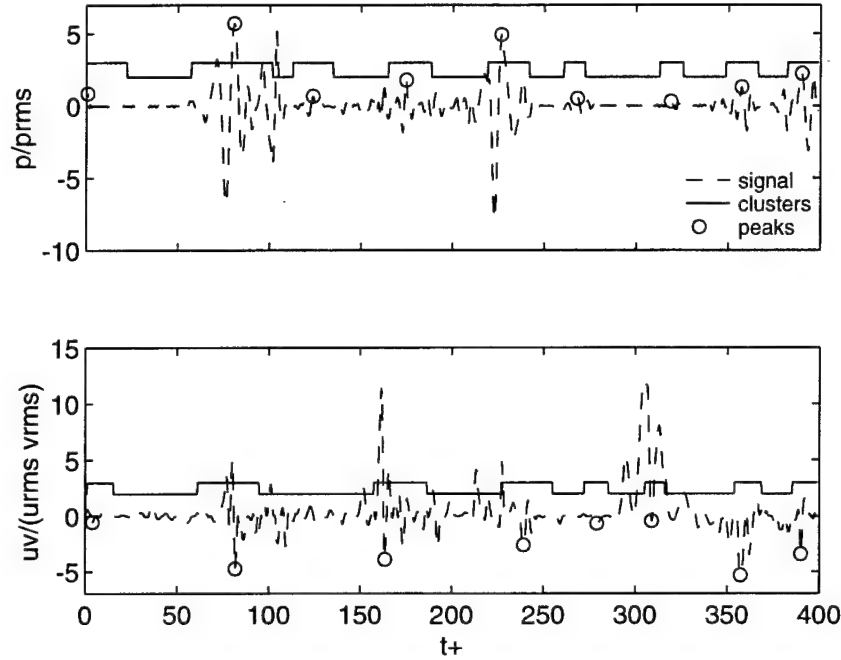


Figure 5.5: LWPDP cluster detection on disturbed  $p_{F2}$  and  $uv_{F2}$  with  $T_w^+ = 30$ .

separated wall transducers,  $p_1$  and  $p_2$ , between the Reynolds stress and the wall pressure at the same streamwise location  $uv$  and  $p_1$ , and between the Reynolds stress and the upstream wall pressure  $uv$  and  $p_2$ . The  $uv$ - $p$  correlations were computed for all  $y$ -locations.

### 5.3.1 Estimation of convection velocity

The experimental arrangement included two wall-pressure transducers separated by a streamwise distance  $\Delta x = 1.27$  cm. This allowed the convection velocity of the organized motions to be computed from

$$U_c = \Delta x / \tau|_{\max R} \quad (5.5)$$

where  $\tau|_{\max R}$  is the time delay, which maximizes the cross correlation function between  $p_1$  and  $p_2$ ,  $R_{p_1, p_2}(\tau)$ . The correlation was formed by dividing the total time records into windows of equal size, performing the correlation between pairs of windows, and then ensemble averaging. A window size of 2048 points (62.5 ms) was used. Similar calculations were made using the localized variance records  $\mathcal{V}_{p_1}(t)$  and  $\mathcal{V}_{p_2}(t)$  and the LWPDP cluster records  $p_{1cl}(t)$  and  $p_{2cl}(t)$ . For completeness, both the unfiltered and F2-filtered cases were examined.

Special attention must be given to computing correlations between the localized variance records, since these functions are positive-definite. Such functions, even

Table 5.2: Convection velocity of organized structures for equilibrium data.

time record	$U_c^+$		$U_c/U_e$	
	Unfiltered	Filtered	Unfiltered	Filtered
Original	17.4 (37)	16.5 (39)	0.70	0.66
LVAR (clusters)	16.5 (39)	16.9 (38)	0.66	0.68
LWPD (clusters)	16.5 (39)	16.9 (38)	0.66	0.68

( ) time delay in sampled points.

$$U_c^+ = 16.9 \pm 0.5$$

$$U_c/U_e = 0.68 \pm 0.02$$

Table 5.3: Convection velocity of organized structures for disturbed data.

time record	$U_c^+$		$U_c/U_e$	
	Unfiltered	Filtered	Unfiltered	Filtered
Original	18.5 (50)	19.8 (47)	0.52	0.55
LVAR (clusters)	20.2 (46)	24.4 (38)	0.56	0.68
LWPD (clusters)	20.6 (39)	22.1 (42)	0.58	0.62

( ) time delay in sampled points.

$$U_c^+ = 22.1 \pm 2.0$$

$$U_c/U_e = 0.62 \pm 0.06$$

uncorrelated random noise, will produce correlation functions with a characteristic sawtooth shape, the peak of which is at zero time delay. Therefore, when performing correlations on localized variance records, the results are reported in dB referenced to the base sawtooth shape. This will be referred to as a *normalized correlation*,  $NC$ .

The results for the convection velocity computed for the equilibrium and disturbed flows are shown in Tables 5.2 and 5.3, respectively. The equilibrium calculations obtained from the three distinct time records are surprisingly consistent. The nominal result  $U_c/U_e = 0.68$  compares with a value of 0.67 obtained by Thomas and Bull from similar measurements in an equilibrium TBL [5.9]. For the disturbed flow, the results cover a wider range, particularly between the unfiltered and filtered cases. However, the filtered LVAR and LWPD time records provided results that were most consistent with the equilibrium results, indicating the validity of these detection schemes.

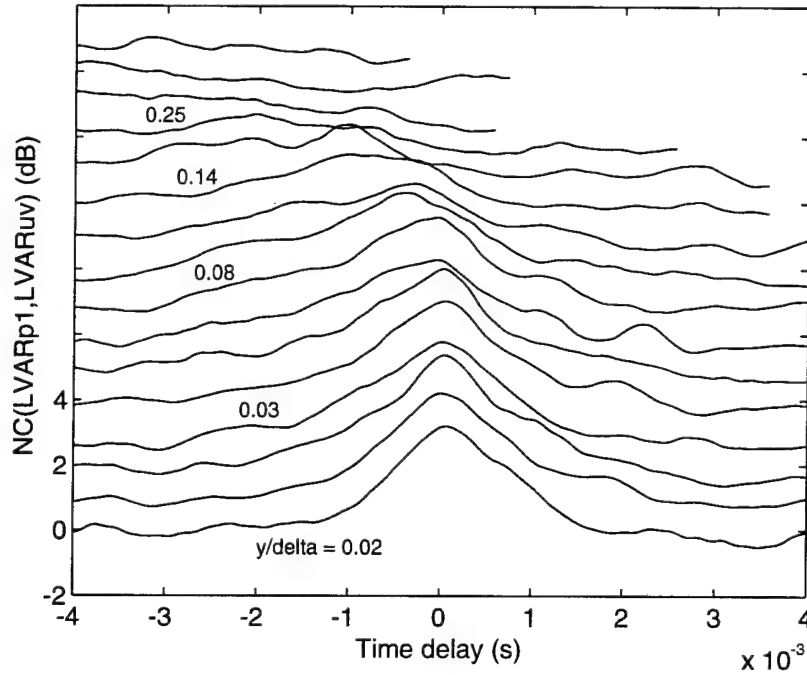


Figure 5.6: Normalized correlation between  $\mathcal{V}_{p_1}$  and  $\mathcal{V}_{uv}$  across the equilibrium TBL. The different  $y$ -locations are shifted upwards for clarity.

### 5.3.2 Correlations between turbulence and wall pressure

To illuminate the shape and extent of the coherent motions, correlations were computed between the wall pressure and the Reynolds stress across the boundary layers. These calculations were performed using the original,  $\mathcal{V}$ , and LWPD cluster time records. Only the results on  $\mathcal{V}$  functions are presented. Similar results were obtained for the original and LWPD time records.

The normalized correlations between the wall pressure and the Reynolds stress were made at each  $y$ -location across the boundary layers. The results are shown in Figure 5.6 for the equilibrium flow and Figure 5.7 for the disturbed flow. These results are for transducer  $p_1$  at the same streamwise location as the X-wire. For clarity, each  $y$ -location is shown shifted upwards by 1 dB relative to the previous station. The wall pressure and Reynolds stress are correlated out to a distance  $y/\delta \approx 0.2$ . Beyond this point, significant peaks in the correlations cannot be unequivocally defined. Notice that, for both flows, the time delay for maximum correlation is zero near the wall, shifting to increasingly negative values across the TBL. A quantitative comparison of the correlations between the equilibrium and disturbed flows can be made from Figure 5.8, which plots results at two specific locations. For both flows, the negative time delay for maximum correlation at  $y/\delta = 0.14$  indicates that the organized motion burst mechanism extends to the log-law region and has a forward angle of inclination.

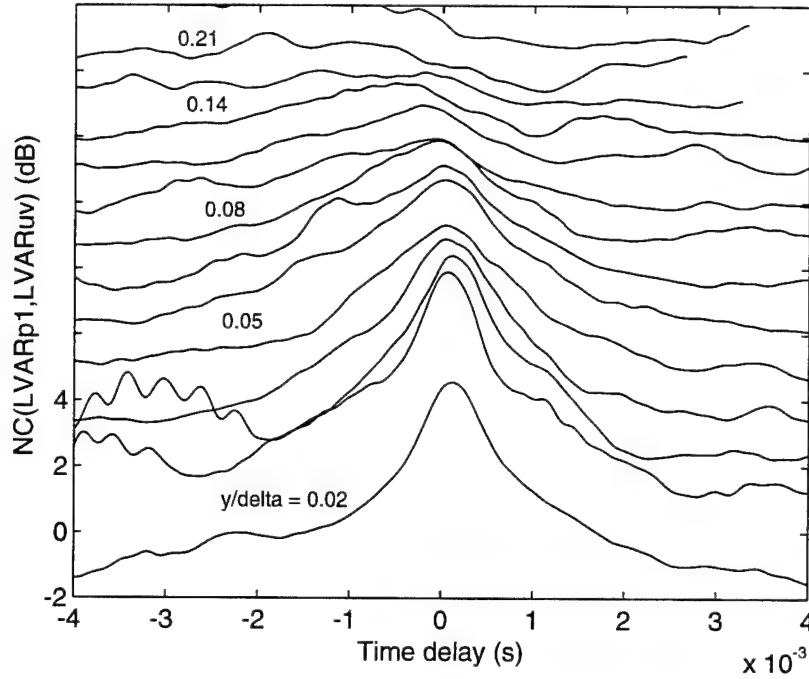


Figure 5.7: Normalized correlation between  $\mathcal{V}_{p_1}$  and  $\mathcal{V}_{uv}$  across the disturbed TBL. The different  $y$ -locations are shifted upwards for clarity.

The time delays for maximum correlation versus position in the boundary layer are presented in Figure 5.9. Results are also included for the correlations of Reynolds stress with the upstream pressure transducer  $p_2$ . These data are more scattered than for  $p_1$  because of the larger distance between transducer  $p_2$  and the X-wire probe. Some points from both plots have been omitted due to the previously mentioned difficulties in identifying a dominant peak outside of  $y/\delta = 0.2$ . Even so, the trends are well-defined, and indicate roughly the same shape for both flows. A representative inclination angle can be inferred from the data in Figure 5.9(b) by noting the  $y$ -location where the time delay is zero. For the equilibrium flow, this point occurs for a  $y/\delta$  between 0.12 and 0.14, which equates to an angle between 15.5 and 18.3 deg. This is consistent with the results of Snarski [5.10] and Thomas and Bull [5.9], who found the dominant structures to be inclined at 18 deg. For the disturbed flow, the point of zero time delay is at  $y/\delta \approx 0.17$ , which roughly equates to an inclination angle of 30.4 deg.

## 5.4 Conditional sampling on event clusters

The features of the cluster patterns were examined from conditional sampling based on the locations obtained from the LWPD algorithm. The ensemble averages were centered around the maximum peak in each detected cluster, using the original (F2-



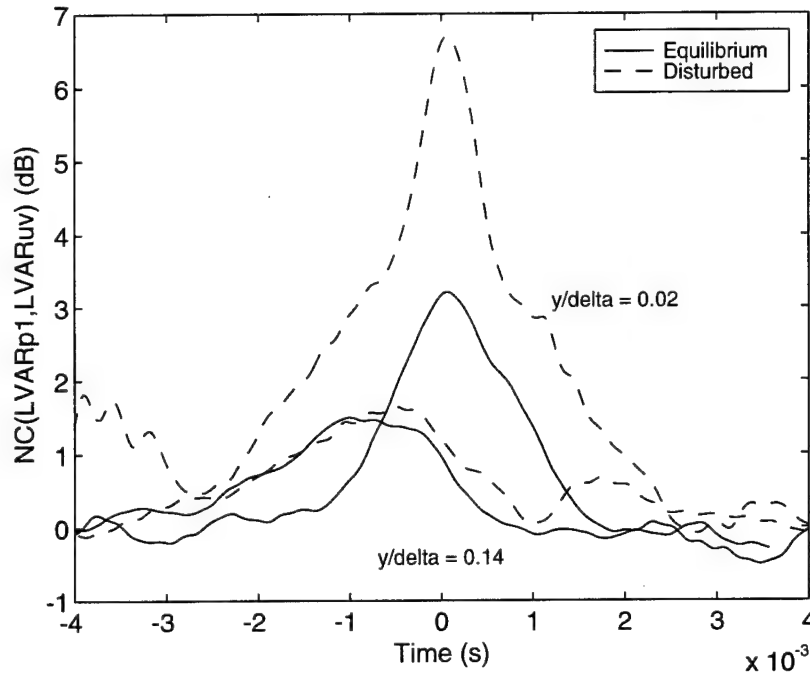


Figure 5.8: Normalized correlation between  $\mathcal{V}_{p1}$  and  $\mathcal{V}_{uv}$  at  $y/\delta = 0.02$  and  $0.14$  in the equilibrium and disturbed flows.

filtered) time records. As in Section 4.5.2, the detection variable is plotted using a thicker solid line. In the present section, results at one  $y$ -location will be compared to those obtained in Chapter 4 using the traditional event-detection methods based on an amplitude threshold level. Results spanning the boundary layers will be discussed in Chapter 6.

#### 5.4.1 Quadrant cluster detection

The LWPD algorithm was applied to the negative of the Q2 Reynolds stress time records,  $uv_2(t)$ , to determine the cluster locations based on negative  $uv_2(t)$  peaks. Figures 5.10 and 5.11 display the conditional sampling results based on these locations for the equilibrium and disturbed flows, respectively. The results for both flows are almost identical with averages based on peak quadrant event-detection, shown previously in Figures 4.20 and 4.22. The primary difference is that the present results are of a reduced magnitude. The LWPD algorithm is able to identify significant flow structure without specifying a magnitude threshold. However, the Q4-Q2-Q4 event pattern was not enhanced by conditioning on clusters.

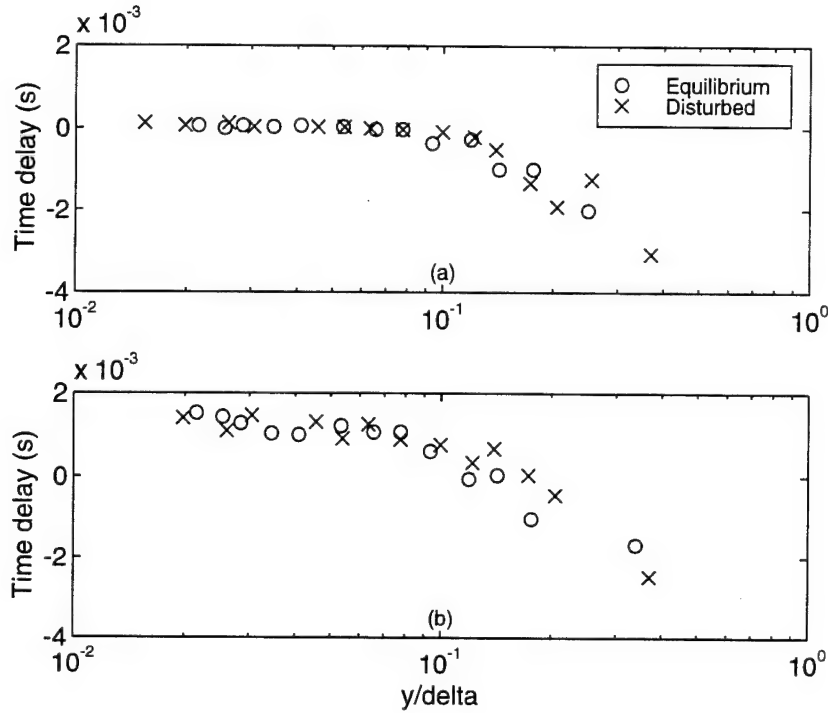


Figure 5.9: Time delays for maximum correlation between wall pressure and Reynolds stress from Figures 5.6–5.8. (a)  $p_1$  vs.  $uv$ . (b)  $p_2$  vs.  $uv$ .

#### 5.4.2 Peak wall-pressure cluster detection

Since one objective of the research is to confirm a bidirectional relationship between wall-pressure and turbulent structures, conditional sampling was performed triggered on positive wall pressure clusters. The results are displayed in Figures 5.12 and 5.13 for the equilibrium and disturbed flows, respectively. Again, the results are almost identical to the conditional sampling based on traditional peak-pressure event detection shown in Figures 4.16 and 4.18. Unlike the conditional sampling based on Q2 clusters, triggering on LWPDP wall pressure clusters has not sacrificed the strengths of the correlations. The most important result is that conditional sampling on pressure indicates that the Q2 events are aligned with the positive pressure peaks. This is most evident in the equilibrium case. The  $uv_2$  peak in the disturbed case is less pronounced. The degradation is probably due to an increase, over the equilibrium case, in the variation of convection velocities, or phase, between individual realizations. This effect is known as phase jitter [5.11]. Even so, the following  $uv_4$  excursion is equally significant in both flows. One difference between the equilibrium and disturbed flows is the relative strengths of the  $u$  and  $v$  motions. The equilibrium flow shows a strong positive  $u$  acceleration with a relatively weaker  $v$  deceleration. In contrast, the  $v$  motion is much stronger in the disturbed flow case, consistent with the increased vertical motions presented in Chapter 3. By comparing the results in

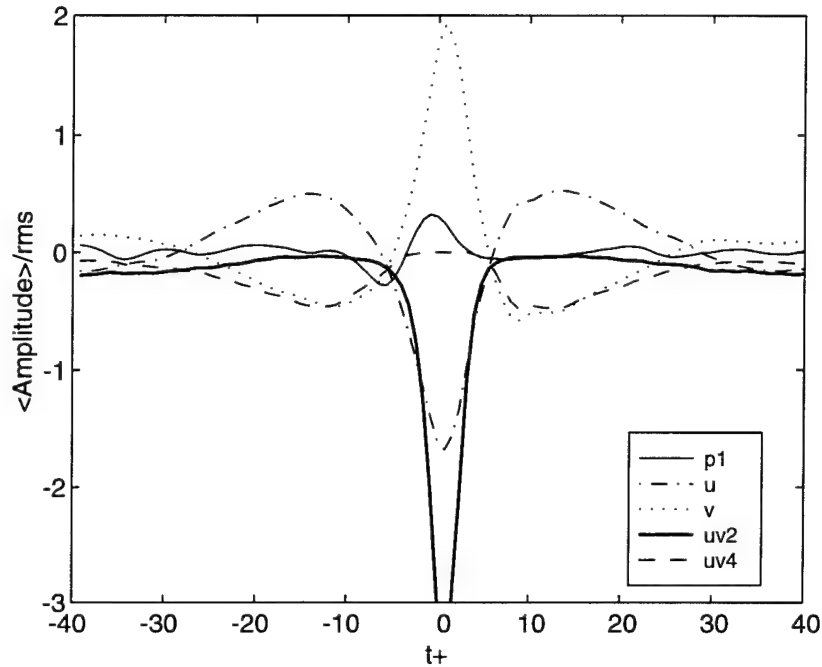


Figure 5.10: Ensemble averages conditioned on equilibrium flow Q2 LWPDP clusters at  $y/\delta = 0.02$ .

Figures 5.10 through 5.13, it appears that a bidirectional relationship exists between positive pressure peaks and Q2 events for both equilibrium and disturbed flows.

## 5.5 Summary

Two new methods have been developed to identify and study clusters of events: LVAR and LWPDP. The positive-definite nature of the localized variance function makes it ideal for correlation applications, while the LWPDP algorithm, with its precise locations of clusters in time, is more suited to conditional sampling. These methods differ from traditional event-detection methods in that they do not rely on the selection of an amplitude threshold level. Instead, both methods require the specification of a time parameter. For the LVAR technique, this parameter corresponds to a characteristic time scale, similar to a wavelet filter at fixed scale. For LWPDP detection, this parameter specifies the minimum time between successive clusters. The algorithm insures that the most significant clusters are identified.

Correlations using  $\mathcal{V}$  functions were successful in deducing the convection velocity of the wall-pressure signature of the organized motions and the spatial extent of the organized motions. The results were consistent with the findings obtained by other researchers.

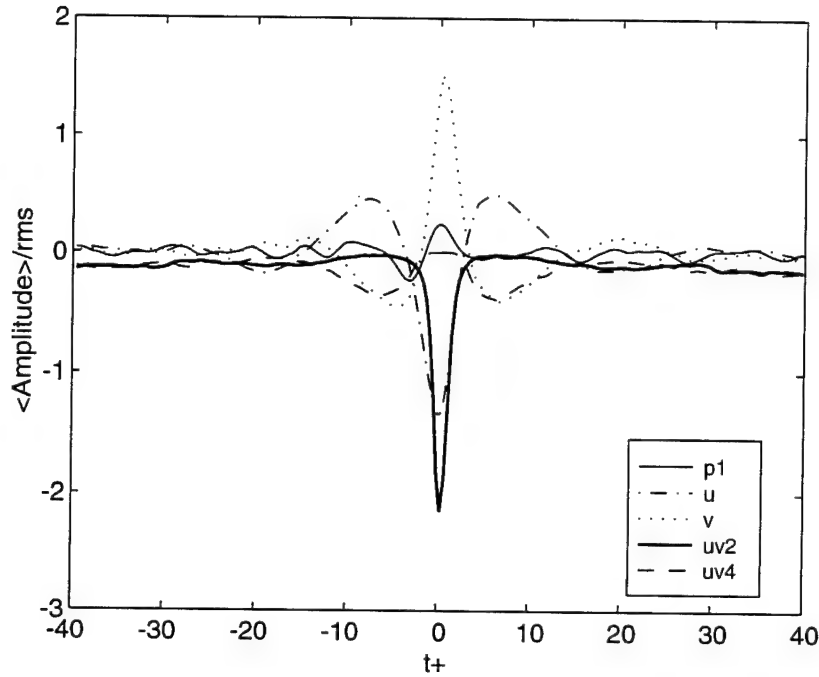


Figure 5.11: Ensemble averages conditioned on disturbed flow Q2 LWPDP clusters at  $y/\delta = 0.02$ .

Conditional sampling based on wall pressure and Q2 LWPDP clusters reproduced the results based on traditional peak and quadrant event-detection techniques presented in Chapter 4. The results conditioned on Q2 clusters showed an alignment of the positive pressure peak with the Q2 event, with Q4 events on either side. The results conditioned on positive wall pressure clusters showed a correlation with Q2-Q4 event pairs. The bidirectional relationship between positive wall-pressure peaks and accelerating  $u$ -velocity or second-quadrant  $uv$  motions was confirmed. While the results may not be a significant improvement over traditional methods, in the sense of increased correlation, the fact that LWPDP detection produced equivalent results suggests that the idea of event clusters is valid. The problem of phase jitter between the conditionally sampled events remains to be addressed.

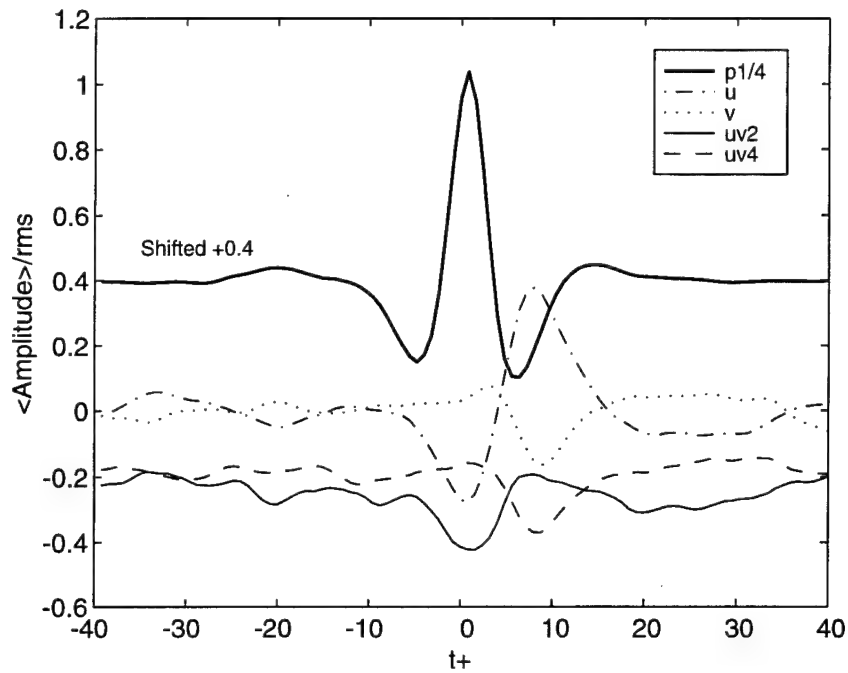


Figure 5.12: Ensemble averages conditioned on equilibrium flow wall pressure LWP clusters at  $y/\delta = 0.02$ .

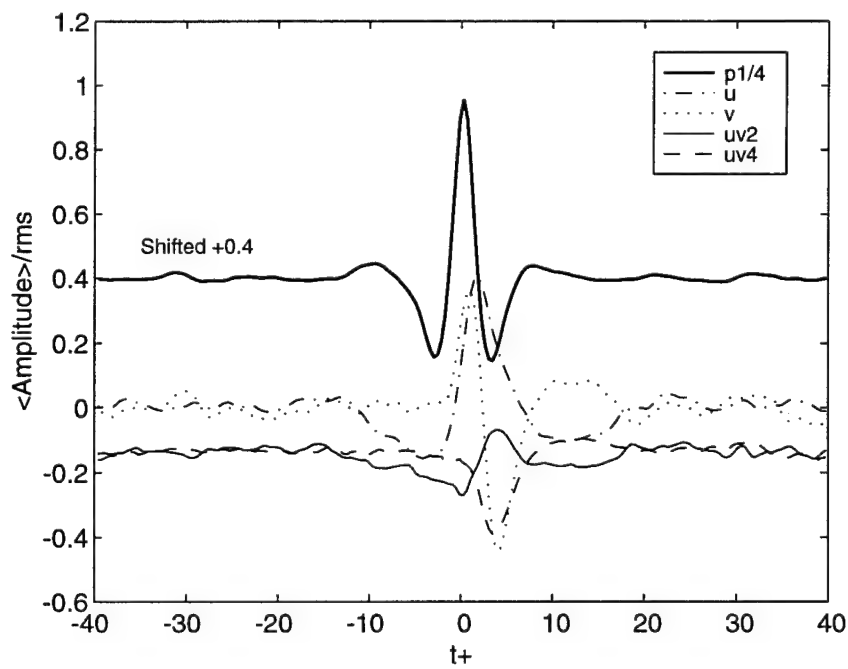


Figure 5.13: Ensemble averages conditioned on disturbed flow wall pressure LWP clusters at  $y/\delta = 0.02$ .

## References

- [5.1] V. Wilczynski. *Organized Turbulent Structures and Their Induced Wall Pressure Fluctuations*. PhD thesis, The Catholic University of America, 1992.
- [5.2] Y. G. Guezennec. *Documentation of Large Coherent Structures Associated with Wall Events in Turbulent Boundary Layers*. PhD thesis, Illinois Institute of Technology, 1985.
- [5.3] Y. Yuan and M. Mokhtarzadeh-Dehghan. A comparison study of conditional-sampling methods used to detect coherent structures in turbulent boundary layers. *Phys. Fluids*, 6(6):2038–2057, 1984.
- [5.4] J. Morrison, H. Tsai, and P. Bradshaw. Conditional-sampling schemes for turbulent flow, based on the variable-interval time averaging (VITA) algorithm. *Experiments in Fluids*, 7:173–189, 1989.
- [5.5] R. F. Blackwelder and J. H. Haritonidis. Scaling of the bursting frequency in turbulent boundary layers. *J. Fluid Mech.*, 132:87–103, 1983.
- [5.6] J. H. Haritonidis, L. S. Gresko, and K. S. Breuer. Wall pressure peaks and waves. In Kline and Afgan, editors, *Near-Wall Turbulence: Proceedings of the 1988 Zoran Zaric Memorial Conference*, pages 397–417. Hemisphere, 1990.
- [5.7] S. R. Snarski and R. M. Lueptow. Wall pressure and coherent structures in a turbulent boundary layer on a cylinder in axial flow. *J. Fluid Mech.*, 286:137–171, 1995.
- [5.8] P. B. Penafiel, M. J. Casarella, and M. E. Kammeyer. Application of wavelet-filtering techniques to intermittent turbulent and wall pressure events, part II — detection of cluster patterns. Technical report, Dept. of Mech. Engineering, The Catholic University of America, Washington, D.C. 20064, 1995.
- [5.9] A. S. W. Thomas and M. K. Bull. On the role of wall-pressure fluctuations in deterministic motions in the turbulent boundary layer. *J. Fluid Mech.*, 128:283–322, 1983.
- [5.10] S. R. Snarski. Relation between the fluctuating wall pressure and the turbulent structure of a boundary layer on a cylinder in axial flow. Technical Report NUWC-NPT 10,223, Naval Undersea Warfare Center, New London, Connecticut 06320, 1993.
- [5.11] R. Blackwelder. On the role of phase information in conditional sampling. *Phys. Fluids*, 20(10):S232–S242, 1977.

## Chapter 6

### Interpretations and conclusions

The results shown in Chapters 4 and 5 confirm that wall-pressure peak events are footprints of near-wall motions for both equilibrium and disturbed flows. Specifically, conditional sampling results near the wall revealed a Q2-Q4, or ejection-sweep sequence bracketing the positive pressure peak. From correlation results across the boundary layers, it was inferred that the structures are inclined downstream. This establishes the framework to address the two central questions of the research:

1. What are the physical features of these near-wall flow structures?
2. Are these near-wall structures coupled to and affected by the outer-layer dynamics?

The first question will be addressed by examining the ensemble-averaged flow field conditioned on wall-pressure cluster events for the equilibrium TBL. The second question will be discussed by comparing the equilibrium and disturbed flows for common near-wall structures. Implicit to both questions is the issue of filtering, which was necessary for the extraction of the near-wall motions.

#### 6.1 Physical features of near-wall flow structures

To explore the spatial extent of the observed organized motions, the ensemble average of  $u$  and  $v$ , conditioned on positive wall-pressure LWPD clusters, was constructed at each  $y$  measurement station. If one assumes that the structures remain intact over a short distance and that they convect with the local mean streamwise velocity, then the time domain can be mapped into space:

$$x_{u,v} = -U(y) \cdot t \quad (6.1)$$

Likewise, the wall-pressure distribution can be inferred from the ensemble-averaged time history using the convection velocities deduced in Section 5.3.1:

$$x_p = -U_c \cdot t \quad (6.2)$$

These assumptions allow the construction of a composite picture of the near-wall flowfield structure associated with positive wall-pressure peaks. This approach was validated by Kim [6.1], who computed ensemble averages based on the VITA technique using data obtained from a large-eddy simulation of turbulent channel flow. The results are presented in Figures 6.1 and 6.2 for the *equilibrium flow* before and after F2 filtering, respectively.

In these figures, the wall-pressure distributions associated with each  $y$  location are plotted to emphasize the consistency of the trigger condition. The flow field displays organized motions that extend out to a distance  $y/\delta = 0.2$ , beyond which correlated structure is not evident. For clarity, the second and fourth  $y$  measurement stations have been omitted, and the magnitude of the velocity vectors has been arbitrarily scaled. The scaling factor for the post-filtered case (Figure 6.2) was twice that of the pre-filter case, reflecting the lower energy content.

The most important feature, visible in both the unfiltered and the filtered data, is that the positive pressure peaks are aligned with ejections followed by strong sweeps from upstream. This finding was shown earlier in Chapter 5 in Figure 5.12. Moreover, conditional sampling based on Q2 clusters confirmed the bidirectionality of this result (cf. Figure 5.10).

First, consider the case before wavelet filtering (Figure 6.1). The Q2-Q4 interface displayed in the composite picture forms a shear layer that is inclined downstream with an inclination of approximately 45 deg. Overall, the flow field is consistent with the schematic diagram of the near-wall motion proposed by Astolfi and Forestier (Figure 1.3). The extent of the wall-pressure footprint, approximately  $160\nu/u_\tau$  or  $0.14\delta$ , also agrees with their finding of 110 to  $130\nu/u_\tau$ . Note that the pressure minima on either side of the peak do not appear in the unfiltered data but do appear after filtering.

Next, consider the effects of filtering (Figure 6.2). Application of the F2 filter changes the flowfield picture in two ways. First, the ejection/sweep motions are steepened, and the dividing shear front is sharpened. Second, significant ancillary structures are revealed in the form of three vortical motions of alternating rotation.

These structures bracket the shear front and merit discussion. Proceeding downstream, the first structure appears as ejection motions that arch around downstream to be entrained in a sweep motion. This vortex motion is not confined to one particular vertical location, but spans the region  $y/\delta \leq 0.2$ . The second structure consists of a vortex core located above the upstream pressure minimum at  $y/\delta = 0.15$ . This is the strongest of the ancillary structures and appears to be driving the main sweep motion. The third structure is a vortex core just downstream of the pressure peak at  $y/\delta = 0.10$ . This vortex appears to be inducing the ejections near the wall.

The flow field pictured in Figure 6.2 is consistent with the models of turbulent boundary-layer structure discussed in Chapter 1. Specifically, it is suggested that the two structures with negative vorticity are the heads of inclined horseshoe vortices. However, the strong vortex in between is puzzling, since its sign is opposite to that



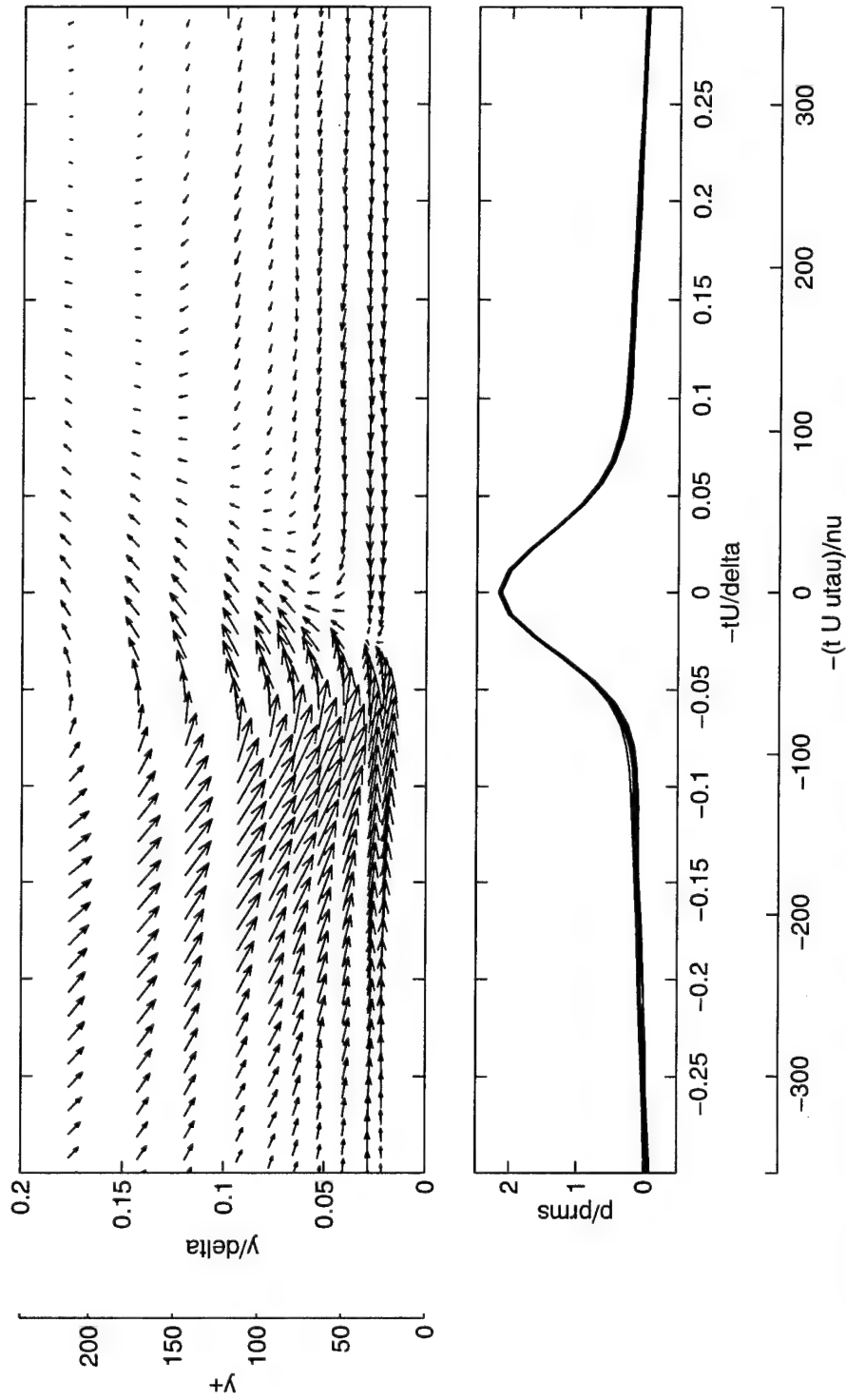


Figure 6.1: Ensemble-averaged equilibrium perturbation flow field conditioned on wall-pressure LWPD clusters prior to F2 filtering and in a reference frame moving with the mean streamwise velocity.

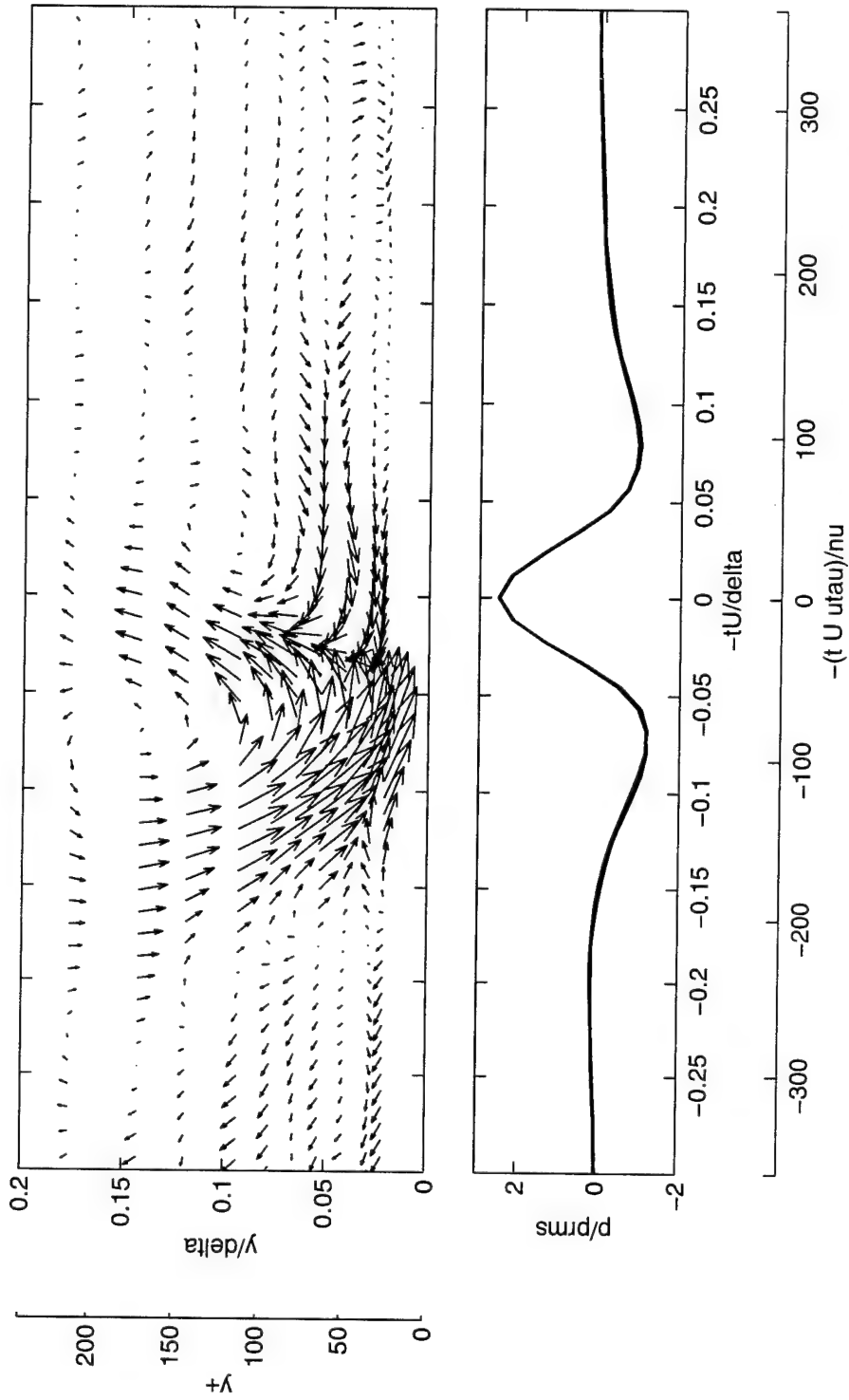


Figure 6.2: Ensemble-averaged equilibrium perturbation flow field conditioned on wall pressure LWPD clusters after F2 filtering and in a reference frame moving with the mean streamwise velocity.

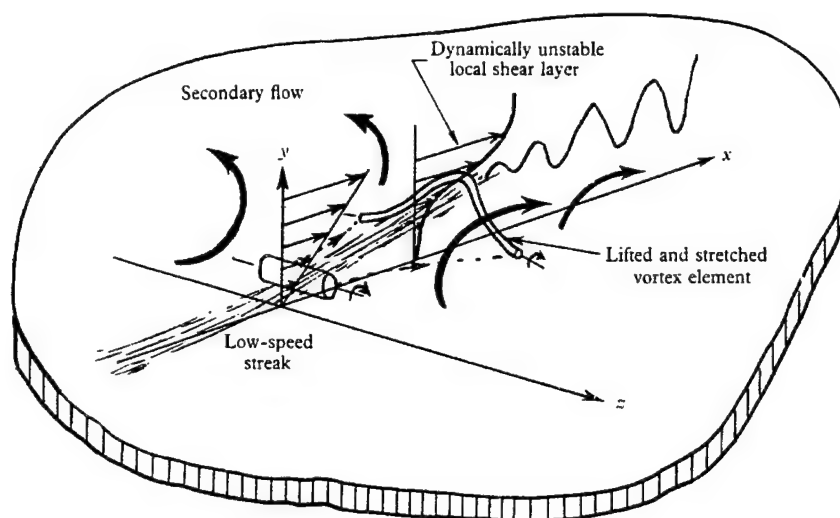


Figure 6.3: The mechanics of streak breakup after Kline, et al. 1967 [6.2].

of a head or neck. More likely, the sweep and inclined shear layer appear so strong and highly correlated precisely because of their relative alignment with the ensemble trigger event, namely, the positive pressure peak. In other words, the fundamental flow structure consists of two horseshoe vortices of negative vorticity, one ahead and above the other, that induce the ejection/sweep pattern and a concomitant wall-pressure peak. This situation was proposed by Kline et al., who put forth the model of streak breakup shown in Figure 6.3. The two vortex shapes and their induced flowfield agree with Figure 6.2. However, the breakup of the structure because of a secondary instability has been superseded (cf. Section 1.2.1).

## 6.2 Effects of outer-layer disturbances

To assess the universality of the near-wall motions and their wall-pressure signatures observed for the equilibrium flow, a disturbed TBL was studied. The data presented in Chapter 3 showed that the disturbed TBL differed from the equilibrium TBL by the addition of large-scale, low-frequency disturbances in the outer regions. The inner layer appeared to have been established quickly downstream after reattachment while the outer layer decayed more slowly. The hypothesis was made that the inner- and outer-layer portions of turbulent boundary layers are uncoupled.

The composite flow pictures for the disturbed flow case are shown in Figures 6.4 and 6.5 for the unfiltered and filtered data, respectively. Because of the different time scales of the flows, twice as many data points are available for the disturbed flow. For clarity of comparison, only every other data point has been plotted. The scaling factors for the vector magnitudes are identical to those used in Figures 6.1

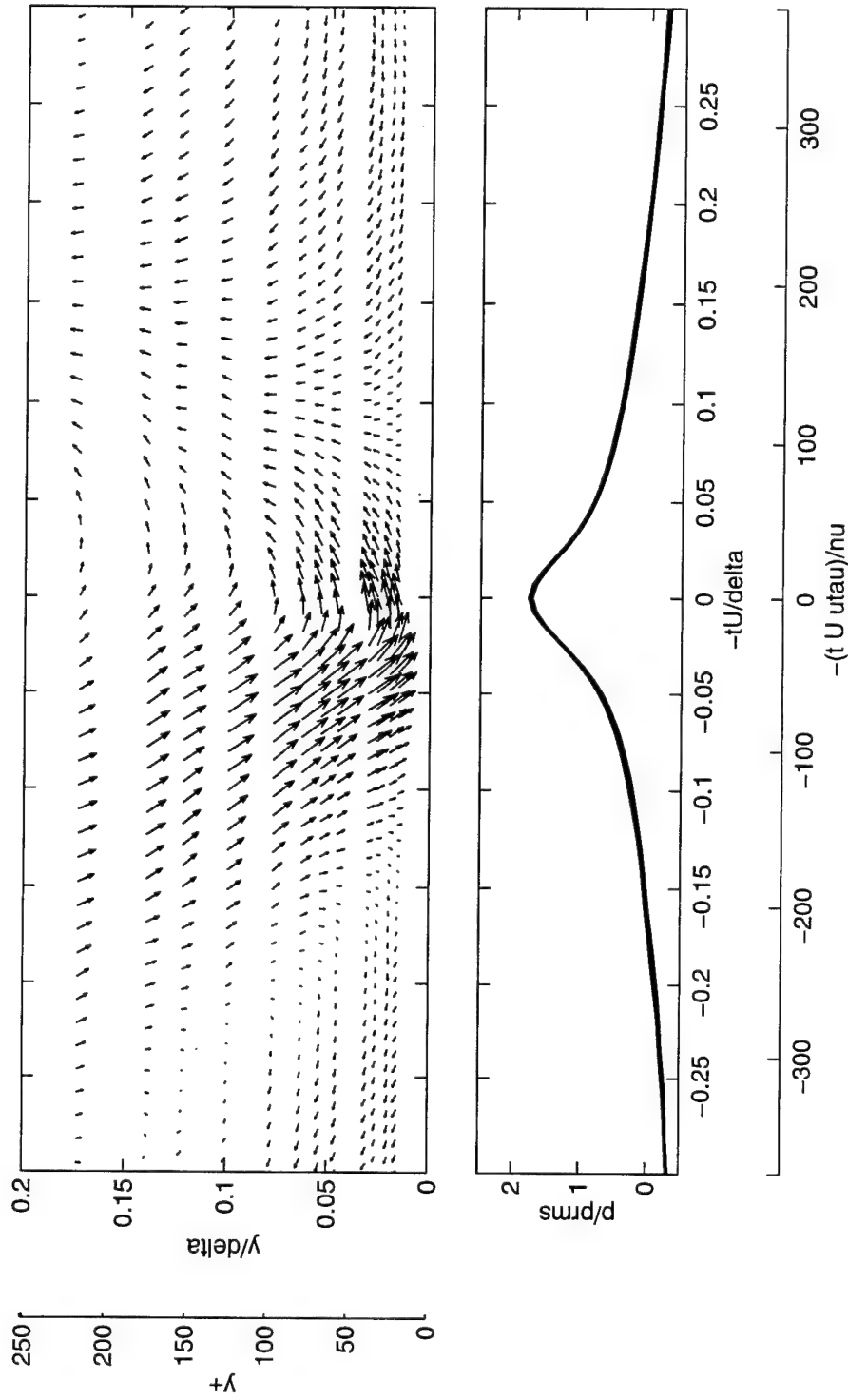


Figure 6.4: Ensemble-averaged disturbed perturbation flow field conditioned on wall-pressure LWPDP clusters prior to F2 filtering and in a reference frame moving with the mean streamwise velocity.

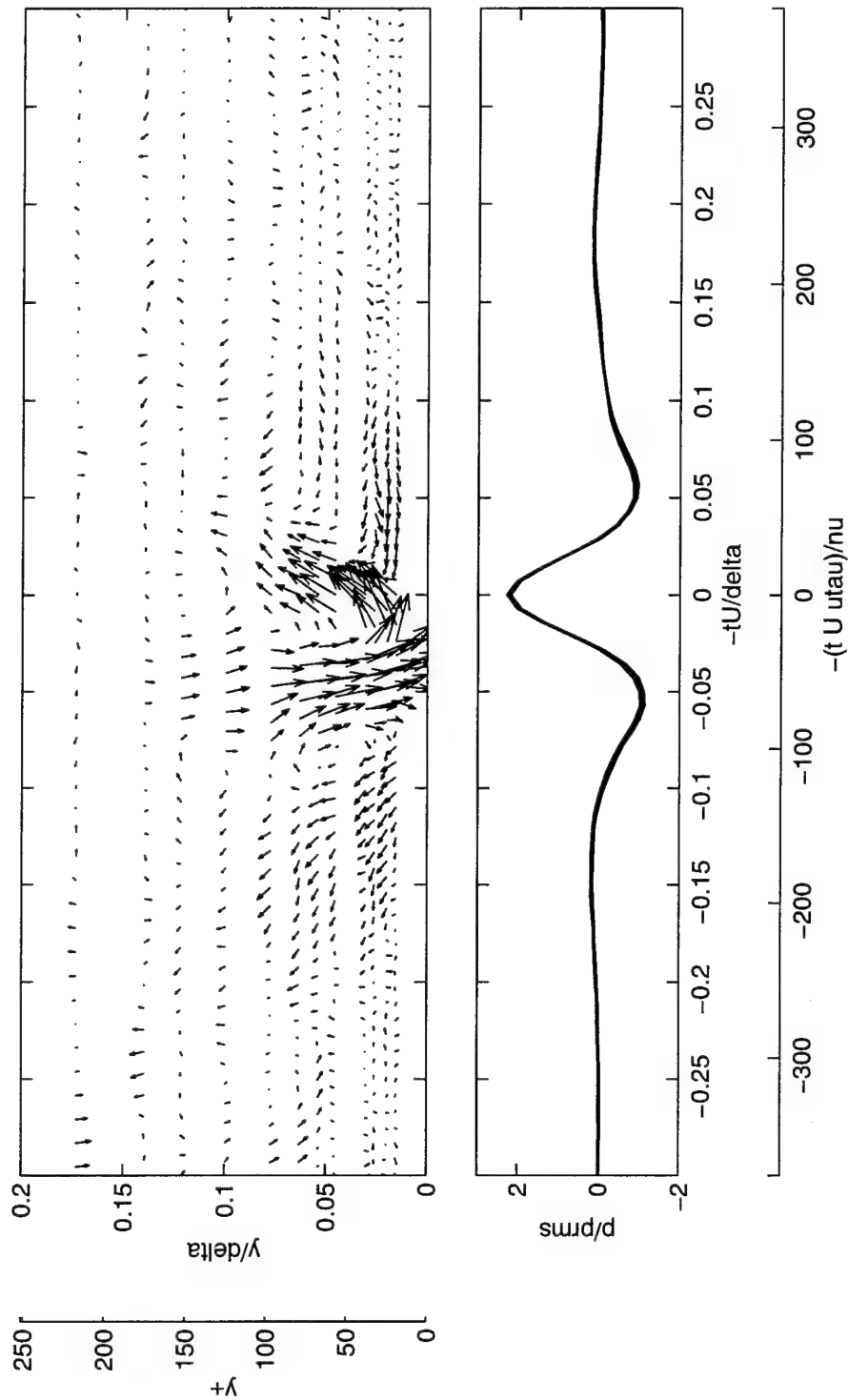


Figure 6.5: Ensemble-averaged disturbed perturbation flow field conditioned on wall pressure LWPD clusters after F2 filtering and in a reference frame moving with the mean streamwise velocity.

and 6.2, respectively. This allows a direct comparison of the structures between the equilibrium and disturbed flows.

As in the previous section, consider first the case before wavelet filtering. Figure 6.4 shows significant differences from the equilibrium case (Figure 6.1). The most significant difference is that a shear front is not apparent. A large-scale, gradual turning of the flow dominates even near the wall. The outward motion is spread out downstream of the wall-pressure peak. At the wall, the pressure signature is also extended with a less pronounced peak. The near-wall motions are clearly contaminated by the outer-layer disturbances.

Application of the wavelet filter in Figure 6.5 shows a more complex picture than for the equilibrium flow, but significant structure is again revealed. The ejection/sweep interface is sharpened and is aligned with the pressure peak. Furthermore, the same sequence of vortical motions revealed in the equilibrium flow has become evident. Arching ejection motions span the vertical range and feed into the primary sweep motion. However, in this case, the motions near the wall form a closed vortex over the upstream pressure minimum at  $y/\delta \approx 0.03$ . A vortex of positive vorticity is again seen above the primary sweep motion, but the negative vortex downstream of the shear front is not as highly correlated as in the equilibrium case. Overall, the ejection/sweep motion is more compact than for the equilibrium flow, spanning approximately  $0.1\delta$ , but the angle of inclination is the same.

The observations made for the filtered data support the hypothesis that the near-wall motions associated with wall-pressure peak events are largely unaffected by the outer-layer disturbances.

## 6.3 Accomplishments

A summary is presented of the major achievements of the research investigation.

- High-resolution, high-quality turbulence data for two flow configurations have been obtained. These archived databases are available to the research community for validation of computational and analytical modeling of turbulent flows.
- Extensive software was developed for both wavelet filtering and signal processing of the raw data. The documented software was written in modular form (MATLAB and C) and has been made available to the naval laboratories and scientific community.
- The research questions were addressed by performing analyses of the raw data for both the equilibrium and disturbed flows. The following deductions were made on the causal relationship between near-wall organized motions and wall-pressure events:

- The results strongly confirm that patterns of large-amplitude wall-pressure events are footprints of the active (turbulence-producing) motions. These pressure signatures contain both positive and negative peak events.
- Wavelet filtering techniques appear to be successful in extracting the wall-pressure signatures of the near-wall motions. This was most apparent in the case of the disturbed flow.
- Clusters of burst events and wall-pressure events are highly correlated. Distinct patterns of burst events (pairing of Q2 and Q4 events) are observed from conditional sampling based on locations of clusters of wall-pressure events. The results show two vortical structures, one ahead and above the other, that induce the ejection/sweep pattern. These motions are detected by the alignment of Q2 events with positive peak wall-pressure events.
- The near-wall motions appear to be weakly coupled to the outer-layer dynamics. This was tested by comparing the results between equilibrium and disturbed flows. The same generic features of the wall structures were observed for both flows.
- The organized motions observed by wall-pressure detection are inclined downstream and extend to the log-law region.
- The physical features of the near-wall motions displayed in flowfield mappings are consistent with the models proposed by several investigators.

## 6.4 Future work

Many of the findings reported in this investigation require further validation. In addition, improvements in both the equipment and spatial extent of the measurements are suggested. Therefore, recommendations for future work are made in three areas: testing, measurements, and signal processing.

### Testing

Wall-pressure data indicate that the traverse system for the hot wire causes some contamination in the midfrequency range due to vortex shedding from the mounting struts. Filtering techniques were used to minimize this noise, but it is suggested that a new traverse system be installed to eliminate this problem.

### Measurements

It is strongly recommended that hot-wire measurements be made at several stream-wise and spanwise locations across the boundary layer. Correlation and conditional

sampling applied to these data will provide a more detailed composite picture of the flowfield and validate the proposed physical models. In addition, it is proposed that an array of pressure transducers be mounted along the surface. This will allow detailed information on the time scales, decay rates, and convection properties of the organized motions. This type of information is required in the design of adaptive techniques for turbulent control.

## Signal processing

A major problem in the analysis of turbulence data by conditional sampling methods is the problem of phase jitter between the bursts and wall-pressure events that are being correlated. When the data are ensemble averaged, significant distortion of the true correlation can appear. Most investigators incorporated a phase-shift correction to each event based on the localized correlation. Since the present data had high resolution, this correction was not needed. However, the improvements in the quality of the conditionally sampled results presented in Chapters 4 and 5 will be apparent. An algorithm should be developed that implements phase-jitter corrections.

## References

- [6.1] J. Kim. On the structure of wall-bounded turbulent flows. *Phys. Fluids*, 26(8):2088-2097, 1983.
- [6.2] S. J. Kline, W. C. Reynolds, F. A. Schraub, and P. W. Runstadler. The structure of turbulent boundary layers. *J. Fluid Mech.*, 30:741-773, 1967.



## Appendix A

### Hot-wire and wall-pressure surveys

This appendix documents the laboratory conditions and the primary anemometer measurements in engineering units. Tabulations are given for the four surveys from which results have been presented, namely, one single- and one X-wire survey for the equilibrium and disturbed TBL flows. Also, results are presented for a series of wall-pressure measurements at various locations downstream of the disturbed flow ramp. This was done to ascertain the location of the point of flow reattachment. Figure A.1 shows the wall-pressure power spectra for these measurements. The maximum low-frequency pressure levels occur at a location  $x/h = 5.4$ , while the maximum high-frequency levels occur at  $x/h = 7.8$ . Integrating these spectra from 50 Hz to the noise floor at 12500 Hz gives the rms distribution shown in Figure A.2. The maximum rms levels are seen to be at  $x/h \approx 7$ . From these observations, it is seen that the primary measurement location of transducer  $p_1$  at  $x/h = 8.6$  is at least one step height downstream of reattachment.

## Equilibrium TBL single-wire survey

Test date: 06-Aug-94  
 Reduction date: 13-Aug-94  
 Probe: TSI 1261A-T1.5, #914074  
 Atmospheric pressure: 101.6 KPa (30.01 inHg)  
 Static temperature: 295.7 K (532.2 R)  
 Freestream velocity,  $U_e$ : 14.79 m/s ( 48.52 ft/s)  
 Shear velocity,  $u_\tau$ : 0.60 m/s ( 1.95 ft/s)  
 Boundary-layer thickness,  $\delta$ : 2.72 cm ( 1.072 in)

Survey station	$y$ (cm)	$y/\delta$	$y^+$	$U$ (m/s)	$U/U_e$	$U^+$	$u_{rms}$ (m/s)	$u_{rms}/u_\tau$
01	0.01	0.003	3.5	2.33	0.158	3.92	0.70	1.169
02	0.01	0.004	4.5	3.36	0.227	5.63	1.02	1.720
03	0.01	0.005	5.5	3.77	0.255	6.33	1.13	1.900
04	0.02	0.007	7.9	4.48	0.303	7.53	1.27	2.132
05	0.02	0.009	9.4	5.01	0.339	8.41	1.35	2.272
06	0.03	0.011	11.4	5.32	0.360	8.93	1.38	2.317
07	0.04	0.014	15.4	6.12	0.414	10.28	1.43	2.402
08	0.05	0.018	18.9	6.58	0.445	11.05	1.44	2.417
09	0.06	0.022	23.3	7.12	0.481	11.95	1.42	2.391
10	0.08	0.029	30.8	7.69	0.520	12.90	1.38	2.325
11	0.11	0.039	41.2	8.26	0.559	13.87	1.31	2.203
12	0.12	0.045	48.2	8.55	0.578	14.36	1.28	2.144
13	0.19	0.069	73.5	9.16	0.619	15.38	1.18	1.979
14	0.22	0.083	87.9	9.43	0.638	15.84	1.15	1.938
15	0.26	0.097	102.8	9.64	0.652	16.19	1.13	1.903
16	0.33	0.120	127.6	10.10	0.683	16.95	1.11	1.857
17	0.42	0.152	162.4	10.49	0.709	17.61	1.08	1.819
18	0.52	0.190	202.1	10.98	0.742	18.43	1.06	1.774
19	0.74	0.271	288.5	11.64	0.787	19.53	1.01	1.694
20	1.00	0.367	390.8	12.23	0.827	20.54	0.95	1.589
21	1.30	0.476	506.5	12.85	0.869	21.57	0.86	1.440
22	1.59	0.583	620.8	13.35	0.903	22.41	0.76	1.281
23	1.92	0.704	749.4	13.88	0.939	23.31	0.64	1.073
24	2.30	0.843	897.9	14.33	0.969	24.06	0.49	0.823
25	2.84	1.042	1109.4	14.72	0.996	24.72	0.25	0.412
26	3.82	1.402	1493.3	14.79	1.000	24.83	0.11	0.183

## Equilibrium TBL X-wire survey

Test date: 13-Aug-94, run 1  
 Reduction date: 05-Sep-94  
 Probe: TSI 1249A-10, #51100  
 Atmospheric pressure: 101.6 KPa (29.99 inHg)  
 Static temperature: 300.3 K (540.5 R)  
 Freestream velocity,  $U_e$ : 16.13 m/s ( 52.93 ft/s)  
 Shear velocity,  $u_\tau$ : 0.64 m/s ( 2.11 ft/s)  
 Boundary-layer thickness,  $\delta$ : 2.95 cm ( 1.161 in)

Survey station	$y$ (cm)	$y/\delta$	$y^+$	$U$ (m/s)	$u_{rms}$ (m/s)	$u_{rms}/u_\tau$	$v_{rms}$ (m/s)	$v_{rms}/u_\tau$
01	0.06	0.022	26.2	8.31	1.45	2.258	0.85	1.318
02	0.07	0.025	30.9	8.57	1.44	2.235	0.83	1.284
03	0.08	0.028	34.6	8.76	1.41	2.197	0.80	1.237
04	0.10	0.034	41.9	9.12	1.37	2.131	0.74	1.158
05	0.12	0.041	49.7	9.36	1.33	2.074	0.71	1.104
06	0.16	0.053	64.9	9.75	1.28	1.984	0.67	1.043
07	0.19	0.065	79.6	10.05	1.25	1.935	0.66	1.023
08	0.23	0.077	94.2	10.28	1.22	1.893	0.65	1.004
09	0.28	0.093	113.6	10.54	1.20	1.862	0.64	1.000
10	0.35	0.119	145.0	10.91	1.17	1.820	0.64	0.996
11	0.42	0.142	173.3	11.34	1.14	1.778	0.64	0.990
12	0.52	0.177	214.7	11.77	1.13	1.750	0.64	0.996
13	0.74	0.250	303.7	12.57	1.06	1.643	0.64	0.989
14	1.00	0.340	413.6	13.22	0.99	1.532	0.61	0.949
15	1.31	0.444	540.3	13.93	0.89	1.382	0.56	0.877
16	1.61	0.545	663.4	14.52	0.79	1.224	0.51	0.798
17	1.92	0.650	790.6	15.02	0.67	1.037	0.45	0.692
18	2.30	0.779	947.6	15.55	0.50	0.774	0.35	0.543
19	2.73	0.926	1125.7	15.91	0.30	0.460	0.24	0.380
20	3.42	1.158	1408.4	16.09	0.13	0.198	0.12	0.186
21	4.51	1.530	1860.2	16.12	0.10	0.157	0.07	0.115
22	6.42	2.175	2645.0	16.14	0.09	0.146	0.07	0.101

**Disturbed TBL single-wire survey**

Test date: 24-Oct-94  
 Reduction date: 27-Oct-94  
 Probe: TSI 1261A-T1.5, #914074  
 Atmospheric pressure: 101.1 KPa (29.86 inHg)  
 Static temperature: 299.0 K (538.2 R)  
 Freestream velocity,  $U_e$ : 13.74 m/s ( 45.08 ft/s)  
 Shear velocity,  $u_\tau$ : 0.32 m/s ( 1.05 ft/s)  
 Boundary-layer thickness,  $\delta$ : 4.05 cm ( 1.593 in)

Survey station	$y$ (cm)	$y/\delta$	$y^+$	$U$ (m/s)	$U/U_e$	$U^+$	$u_{rms}$ (m/s)	$u_{rms}/u_\tau$
01	0.02	0.004	3.1	1.97	0.143	6.16	1.02	3.174
02	0.02	0.005	4.4	2.52	0.183	7.87	1.19	3.724
03	0.03	0.007	5.5	2.75	0.200	8.58	1.25	3.919
04	0.04	0.009	7.5	3.00	0.218	9.38	1.31	4.103
05	0.05	0.011	9.3	3.21	0.234	10.04	1.36	4.240
06	0.05	0.013	11.2	3.40	0.248	10.63	1.39	4.337
07	0.07	0.016	13.5	3.58	0.260	11.18	1.41	4.418
08	0.09	0.021	17.4	3.80	0.276	11.87	1.43	4.484
09	0.11	0.028	22.8	4.02	0.292	12.55	1.46	4.548
10	0.13	0.032	26.7	4.15	0.302	12.96	1.46	4.578
11	0.20	0.049	40.2	4.44	0.323	13.89	1.50	4.688
12	0.23	0.057	47.3	4.57	0.332	14.27	1.53	4.768
13	0.27	0.067	55.6	4.69	0.341	14.66	1.55	4.839
14	0.33	0.082	68.0	4.87	0.355	15.24	1.58	4.954
15	0.47	0.116	96.3	5.50	0.400	17.18	1.76	5.492
16	0.71	0.176	145.9	6.63	0.482	20.71	1.95	6.097
17	0.90	0.223	184.9	7.58	0.552	23.69	2.00	6.263
18	1.30	0.322	266.1	9.55	0.695	29.84	1.73	5.398
19	1.59	0.394	325.9	10.74	0.781	33.56	1.32	4.141
20	1.94	0.480	397.5	11.69	0.851	36.53	0.92	2.865
21	2.30	0.569	471.0	12.35	0.899	38.59	0.72	2.240
22	2.88	0.711	587.9	13.04	0.949	40.76	0.47	1.482
23	3.83	0.945	782.1	13.58	0.988	42.45	0.14	0.424
24	5.10	1.259	1041.7	13.71	0.997	42.84	0.08	0.237
25	6.17	1.526	1262.4	13.74	1.000	42.95	0.07	0.214

## Disturbed TBL X-wire survey

Test date: 08-Oct-94, run 2  
 Reduction date: 27-Oct-94  
 Probe: TSI 1249A-10, #51100  
 Atmospheric pressure: 101.6 KPa (30.00 inHg)  
 Static temperature: 296.1 K (533.0 R)  
 Freestream velocity,  $U_e$ : 16.18 m/s ( 53.09 ft/s)  
 Shear velocity,  $u_\tau$ : 0.45 m/s ( 1.47 ft/s)  
 Boundary-layer thickness,  $\delta$ : 4.30 cm ( 1.691 in)

Survey station	$y$ (cm)	$y/\delta$	$y^+$	$U$ (m/s)	$u_{rms}$ (m/s)	$u_{rms}/u_\tau$	$v_{rms}$ (m/s)	$v_{rms}/u_\tau$
01	0.07	0.015	19.3	5.53	1.61	3.599	0.78	1.782
02	0.09	0.020	24.9	5.71	1.63	3.654	0.83	1.854
03	0.11	0.026	32.6	5.87	1.67	3.738	0.88	1.970
04	0.13	0.030	38.2	5.94	1.69	3.773	0.91	2.043
05	0.20	0.046	57.1	6.18	1.72	3.856	1.04	2.319
06	0.23	0.054	67.5	6.30	1.75	3.924	1.10	2.453
07	0.27	0.063	79.4	6.45	1.79	3.993	1.16	2.600
08	0.33	0.077	97.2	6.66	1.83	4.103	1.25	2.806
09	0.43	0.100	125.0	7.11	1.96	4.382	1.38	3.081
10	0.52	0.122	152.9	7.55	2.04	4.567	1.45	3.245
11	0.60	0.140	175.1	7.91	2.09	4.669	1.47	3.293
12	0.74	0.173	217.4	8.67	2.17	4.845	1.49	3.322
13	0.88	0.205	257.5	9.46	2.17	4.845	1.46	3.262
14	1.10	0.255	320.2	10.71	2.04	4.552	1.35	3.007
15	1.30	0.303	380.3	11.75	1.80	4.022	1.19	2.650
16	1.59	0.371	465.6	13.02	1.32	2.960	0.94	2.104
17	1.92	0.448	561.7	13.92	0.94	2.100	0.70	1.570
18	2.30	0.536	672.3	14.64	0.71	1.588	0.53	1.178
19	2.85	0.664	833.6	15.39	0.49	1.090	0.36	0.812
20	3.77	0.877	1100.0	15.96	0.17	0.377	0.17	0.372
21	4.90	1.141	1432.1	16.09	0.11	0.246	0.09	0.192
22	5.93	1.380	1731.5	16.18	0.10	0.230	0.07	0.165
23	7.44	1.732	2174.1	16.26	0.10	0.221	0.07	0.147

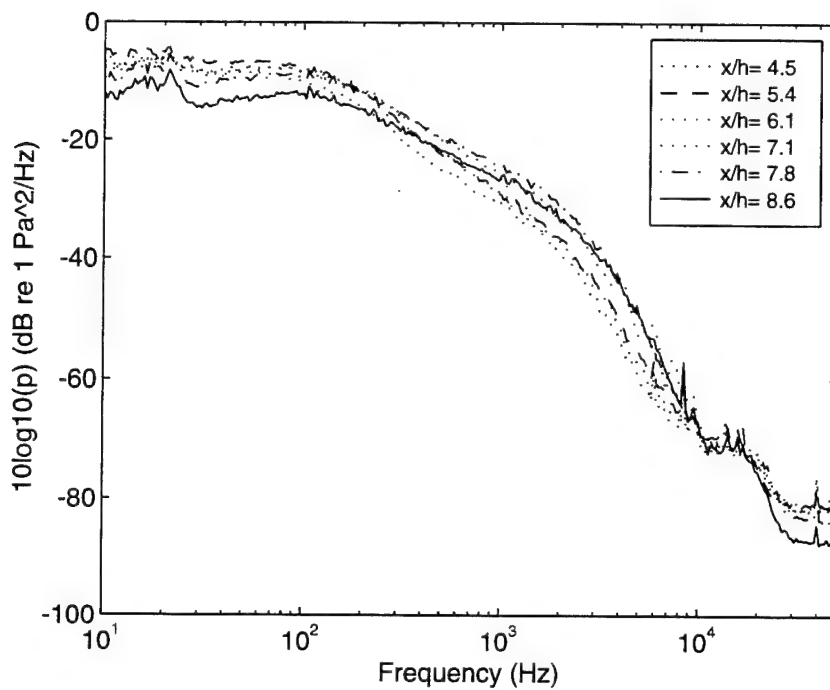


Figure A.1: Wall-pressure spectra downstream of the disturbed flow ramp.

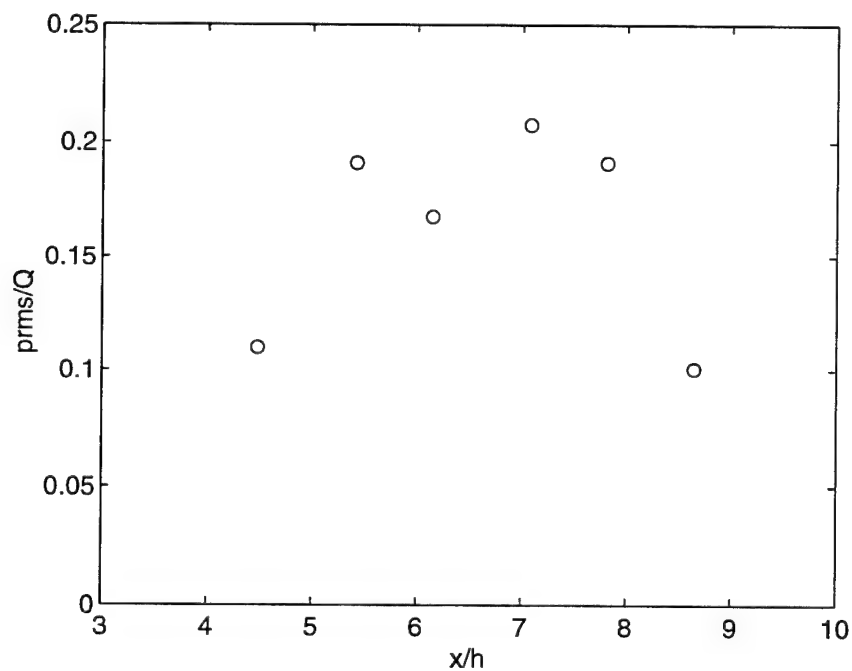


Figure A.2: Distribution of rms wall pressure downstream of the disturbed flow ramp.

## Appendix B

### Measurement uncertainty

Measurement uncertainties were estimated using the principles set forth in [B.1, B.2]. In general, the uncertainty in a measurement was composed of a combination of fixed error or bias,  $B$ , and random error or precision,  $P$ . The root-sum-square model was used to estimate the uncertainties at the 95 percent confidence level:

$$U_{rss} = \pm [B^2 + P^2]^{1/2} \quad (\text{B.1})$$

$$= \pm [B^2 + (t_{95}S)^2]^{1/2} \quad (\text{B.2})$$

where  $U_{rss}$  is the uncertainty,  $S$  is the sample standard deviation, and  $t_{95}$  is the 95th percentile point for the two-tailed Students "t" distribution (95 percent confidence interval). For sample sizes greater than 30,  $t_{95}$  is considered equal to 2. Bias and precision errors were propagated through to calculated results individually, then combined into overall uncertainties. Traceability of working standards to the National Institute of Standards and Technology (NIST) was established through the Navy Metrology and Calibration (METCAL) Program and through manufacturer-supplied calibrations.

The estimated uncertainties are presented in Table B.1. In general, two contributors to the bias were considered: the bias of the working standard against which the instrument was calibrated, and the bias of the calibration as determined through the actual measurement system. The total bias was then estimated as the root-sum-square of the two contributors. Correlated biases were handled as outlined in [B.2]. This procedure proved important for the velocity measurements, where the single thermocouple measuring the tunnel static temperature was also used to determine the calibration reference temperature. The correlated biases cancel, allowing an instrument with relatively large bias to be used. The precision was estimated from in-place readings using the entire measurement system as  $P = t_{95}S$ . The combination of uncertainty components by root-sum-square has the effect that any single component less than about 10 percent of the maximum contributor can be neglected. Negligible contributors are indicated by a dash in Table B.1.

Table B.1: Instrumentation specifications and estimated uncertainties.

Quantity (units)	Type	$B$	$P$	$U_{rss}$
Atmospheric pressure (mmHg)	Welch Scientific barometer	2.5e-3	—	2.5e-3
Pitot/static difference (mmHg)	Edwards High Vacuum 570D-10T-2C2-V1X	5.5e-3	4.0e-3	6.8e-3
Atmospheric temperature (deg C)	mercury-in-glass thermometer	1.0	—	1.0
Tunnel temperature, $T$ (deg C)	Omega DP11 type K thermocouple	2.2	0.2	2.2
Fluctuating wall pressure, $p$ (Pa)	Brüel & Kjær 4138	—	5.0e-3	5.0e-3
$u$ velocity (m/s)	DISA/TSI single wire	0.025	0.010	0.027
	DISA/TSI X-wire	0.030	0.004	0.030
$v$ velocity (m/s)	DISA/TSI X-wire	0.030	0.004	0.030
Probe location, $y$ (m)	telescope with Ono Sokki DG-357	2.8e-5	2.8e-5	4.0e-5
Power spectra (dB)	HP 3562A dynamic signal analyzer	0.2	0.03	0.2

## References

- [B.1] ANSI/ASME. *Measurement Uncertainty*, volume 19.1 of *Performance Test Codes*. American Society of Mechanical Engineers, 1985.
- [B.2] H. Coleman and G. Steele. *Experimentation and Uncertainty Analysis for Engineers*. John Wiley & Sons, 1989.



## Appendix C

### Localized windowed peak detection algorithm

This appendix contains the source code for the Localized Windowed Peak Detection (LWPD) algorithm. The code is written in MATLAB. A few notes are provided for those not familiar with the notation. Comments are preceeded by the % character. The first contiguous block of comment lines are displayed by the help facility. The notation  $a(m,n)$  denotes a matrix  $a$  with  $m$  rows and  $n$  columns. The : character is used to designate a range, as in  $ni=1:m$ .

```
function table=lwpd(data,tw)
%LWPD    Localized Windowed Peak Detection (LWPD) Algorithm.
%        table=lwpd(data,tw)
%
%Input Parameters:
% data --time record
% tw --window size in samples
%Output Parameters:
% table --Table for LWPD events.  It contains:
% column 1 --trigger index
% column 2 --start index
% column 3 --end index
% column 4 --peak index
%
% Note:  This function calls PEVENT at each recursion level.

% By P. Penafiel
% April, 1995
% Last revision: April,1995

[z0,flag]=pevent(data);
while flag
    [z0,flag]=pevent(z0,tw);
end
table=[z0(:,2),z0(:,3:4),z0(:,1)];
```

```

function [z,flag]=pevent(y,x0)
%PEVENT One pass in the recursion of the LWPD algorithm.
%
%Input Parameters:
% y          --      time record
% x0         --      window size in samples
%Output Parameters:
% z          --      Table for LWPD events at the present recursion
%                    level. It contains:
%                    column 1      --      trigger index
%                    column 2      --      start index
%                    column 3      --      end index
%                    column 4      --      peak index
% flag       --      0 if end of recursion,
%                    1 otherwise,

```

% By P. Penafiel

% Mar/1995

%% Comments beginning with %% added by M. Kammeyer, 18 Aug 95

```

[m,n]=size(y);
z=zeros(m,4);      %z(:,3) start; z(:,4) end
flag=0;
nj=0;

%% If first pass through LWPD, find the local peaks and write them
%% to the keeper matrix, z. Start and end of each peak event is one
%% point shy of the local minimum on either side of the peaks.
if nargin==1
    if n ~= 1
        error('input argument should be a column vector');
    end
    for ni=2:m-1                %% for time indices 2 thru m-1
        if (y(ni)>y(ni+1)) & (y(ni)>y(ni-1)) %% if y(ni) is a local peak
            nj=nj+1;
            z(nj,1)=ni;          %% write the time and value
            z(nj,2)=y(ni);       %% to the keeper matrix, z
            nk=ni;
            while(y(nk)>y(nk+1))
                nk=nk+1;
                if (nk==m) nk=nk+1; break; end
            end
            z(nj,4)=nk-1;
            nk=ni;
            while(y(nk)>y(nk-1))
                nk=nk-1;
                if (nk==1) nk=nk-1; break; end
            end
            z(nj,3)=nk+1;

```

```

    end
  end
  if nj
    flag=1;
  end

  %% If in the recursion loop of LWP
elseif nargin==2
  for ni=1:m          %% Loop over time indices
    if ni==1          %% If first peak
      if (y(ni+1,1)-y(ni,1))<x0    %% if first peak is not isolated
        if (y(ni,2)>y(ni+1,2))    %% but it is a local peak
          nj=nj+1;                %% then keep it
          z(nj,1:3)=y(ni,1:3);
          z(nj,4)=y(ni+1,3);
          flag=1;
        end
      else
        %% if first peak is isolated
        %% keep it
        nj=nj+1;
        z(nj,1:4)=y(ni,1:4);
      end

    elseif ni==m      %% If last peak
      if (y(ni,1)-y(ni-1,1))<x0    %% if last peak is not isolated
        if (y(ni,2)>y(ni-1,2))    %% but it is a local peak
          nj=nj+1;                %% then keep it
          z(nj,1:2)=y(ni,1:2);
          z(nj,3)=y(ni-1,4);
          z(nj,4)=y(ni,4);
          flag=1;
        end
      else
        %% if last peak is isolated
        %% keep it
        nj=nj+1;
        z(nj,1:4)=y(ni,1:4);
      end

    else              %% all interior peaks
      if (y(ni,1)-y(ni-1,1))<x0    %% if this peak is not isolated
        if (y(ni+1,1)-y(ni,1))<x0  %% on either side
          if (y(ni,2)>y(ni-1,2)) & (y(ni,2)>y(ni+1,2)) %% and it is a
            nj=nj+1;                %% local peak
            z(nj,1:2)=y(ni,1:2);    %% then keep it
            z(nj,3)=y(ni-1,4);
            z(nj,4)=y(ni+1,3);
            flag=1;
          end
        else
          %% if this peak is isolated
          %% from the NEXT ONLY,
          %% AND is greater
          %% than the previous peak, then
          if (y(ni,2)>y(ni-1,2))
            nj=nj+1;
            z(nj,1:2)=y(ni,1:2);
          end
        end
      end
    end
  end
end

```

```

        z(nj,3)=y(ni-1,4);      %% keep it
z(nj,4)=y(ni,4);
        flag=1;
        end
    end
else
    if (y(ni+1,1)-y(ni,1))<x0    %% if this peak is isolated
        %% from the PREVIOUS ONLY,
        if (y(ni,2)>y(ni+1,2))    %% AND is greater
            nj=nj+1;             %% than the next peak, then
            z(nj,1:3)=y(ni,1:3);  %% keep it
            z(nj,4)=y(ni+1,3);
            flag=1;
        end
    else
        %% if this peak is isolated
        %% on both sides, keep it
        nj=nj+1;
        z(nj,1:4)=y(ni,1:4);
    end
end
end

end

else
    error('Maximum 2 input arguments are accepted');
end

z=z(1:nj,:);

```

## DISTRIBUTION

	<u>Copies</u>		<u>Copies</u>
<b>DOD ACTIVITIES (CONUS)</b>		ATTN CODE 03TT (H M NICHOLSON)	1
		COMMANDER	
ATTN JOHNATHAN GERSHFELD	1	NAVAL SEA SYSTEMS COMMAND	
CODE 50 (THOMAS HUANG)	1	2531 JEFFERSON DAVIS HWY	
CODE 54 (WILLIAM MORGAN)	1	ARLINGTON VA 22242-5160	
CODE 54 (FRANK PETERSON)	1		
CODE 542 (THOMAS FU)	1	ATTN LCDR VINCE WILCZYNSKI	1
CODE 725 (STEVEN RUSSELL)	1	UNITED STATES COAST GUARD ACADEMY	
CODE 742 (THEODORE FARABEE)	1	15 MOHEGAN AVENUE	
CODE 80 (WILLIAM BLAKE)	1	NEW LONDON CT 06320	
COMMANDER			
CARDEROCK DIVISION		ATTN M/S 197 (DENNIS BUSHNELL)	1
NAVAL SURFACE WARFARE CENTER		NATIONAL AERONAUTICS AND SPACE	
BETHESDA MD 20084-5000		ADMINISTRATION	
		LANGLEY RESEARCH CENTER	
ATTN CODE 8233		HAMPTON VA 23681	
(PROMODE BRANDYOPADHYAY)	1		
CODE 102 (STUART DICKINSON)	1	<b>NON-DOD ACTIVITIES (CONUS)</b>	
COMMANDING OFFICER			
NAVAL UNDERSEA WARFARE CENTER		ATTN PROF RONALD ADRIAN	1
DETACHMENT		UNIVERSITY OF ILLINOIS	
1176 HOWELL STREET		16 TALBOT LABORATORY	
NEWPORT RI 02841-1708		104 SOUTH WRIGHT STREET	
		URBANA IL 61801	
ATTN CODE 2141 (WILLIAM KEITH)	2		
COMMANDING OFFICER		ATTN PROF PETER BERNARD	1
NAVAL UNDERSEA WARFARE CENTER		PROF UGO PIOMELLI	1
NEW LONDON CT 06320		UNIVERSITY OF MARYLAND	
		DEPT OF MECHANICAL ENGINEERING	
ATTN CODE ONR 333 (PATRICK PURTELL)	1	COLLEGE PARK MD 20742	
CODE ONR 333 (EDWIN ROOD)	1		
CODE ONR 333 (SPIRO LEKLOUDIS)	1	ATTN PROF PAUL DURBIN	1
OFFICE OF NAVAL RESEARCH		STANFORD UNIVERSITY	
800 NORTH QUINCY STREET		CENTER FOR TURBULENCE RESEARCH	
ARLINGTON VA 22217-5660		STANFORD CA 94305-3030	
ATTN JAMES M MICHAEL	1	ATTN PROF RONALD PANTON	1
AIR FORCE OFFICE OF SCIENTIFIC		UNIVERSITY OF TEXAS	
RESEARCH		DEPT OF MECHANICAL ENGINEERING	
BOLLING AFB DC 20332		AUSTIN TX 78712	

## DISTRIBUTION (CONTINUED)

	<u>Copies</u>		<u>Copies</u>
ATTN PROF MARIO CASARELLA	5	ATTN PROF HERMANN FASEL	1
DR PABLO PENAFIEL	1	PROF ISRAEL WYGNANSKI	1
PROF Y C WHANG	1	UNIVERSITY OF ARIZONA	
THE CATHOLIC UNIVERSITY OF AMERICA		DEPT OF AEROSPACE AND MECHANICAL	
DEPT OF MECHANICAL ENGINEERING		ENGINEERING	
WASHINGTON DC 20064		AERO BUILDING 16	
		TUCSON AZ 85721	
ATTN PROF RON BLACKWELDER	1		
PROF FREDERICK BROWAND	1	ATTN PROF HASSAN NAGIB	1
GEOFFREY SPEDDING	1	PROF CANDACE WARK	1
UNIVERSITY OF SOUTHERN CALIFORNIA		ILLINOIS INSTITUTE OF TECHNOLOGY	
DEPT OF AEROSPACE ENGINEERING		MECHANICAL AND AEROSPACE	
UNIVERSITY PARK		ENGINEERING DEPARTMENT	
LOS ANGELES CA 90089-1191		10 WEST 32ND STREET	
		CHICAGO IL 60616	
ATTN PROF MANHAR DHANAK	1		
FLORIDA ATLANTIC UNIVERSITY		ATTN PROF STEVEN ORSZAG	1
DEPT OF OCEAN ENGINEERING		PRINCETON UNIVERSITY	
777 GLADES RD		DEPT OF MECHANICAL AND AEROSPACE	
BOCA RATON FL 333431-0991		ENGINEERING	
		FORRESTAL CAMPUS	
ATTN PROF PETER BRADSHAW	1	PRINCETON NJ 08544	
PROF JOHN EATON	1		
PROF JOEL FERZIGER	1	ATTN PROF RICHARD LUEPTOW	1
PROF PARVIZ MOIN	1	NORTHWESTERN UNIVERSITY	
STANFORD UNIVERSITY		DEPT MECHANICAL ENGINEERING	
DEPT OF MECHANICAL ENGINEERING		2145 SHERIDAN ROAD	
STANFORD CA 94305-3030		EVANSTON IL 60208	
ATTN PROF FAZLE HUSSAIN	1	ATTN PROF J MORRISON	1
UNIVERSITY OF HOUSTON		IMPERIAL COLLEGE	
DEPT OF MECHANICAL ENGINEERING		DEPT OF AERONAUTICS	
HOUSTON TX 77004		PRINCE CONSORT RD	
		LONDON SW7 2BY UK	
ATTN PROF CHARLES MENEVEAU	1		
JOHNS HOPKINS UNIVERSITY		ATTN PROF R SREENIVASAN	1
DEPT OF MECHANICAL ENGINEERING		YALE UNIVERSITY	
CHARLES AND 34TH STREET		MASON LABORATORY	
BALTIMORE MD 21218		NEW HAVEN CT 06520	

## DISTRIBUTION (CONTINUED)

	<u>Copies</u>		<u>Copies</u>
ATTN PROF JOHN KIM UNIVERSITY OF CALIFORNIA AT LOS ANGELES MECHANICAL AEROSPACE AND NUCLEAR ENGINEERING 46-147 ENG IV 405 HILGARD AVENUE LOS ANGELES CA 90024-1597	1	ATTN PROF YANN GUEZENNEC OHIO STATE UNIVERSITY DEPT OF MECHANICAL ENGINEERING 206 W 18TH AVENUE COLUMBUS OH 43210	1
ATTN PROF ROGER SIMPSON VIRGINIA POLYTECHNIC INSTITUTE AND STATE UNIVERSITY DEPT OF AEROSPACE AND OCEAN ENGINEERING BLACKSBURG VA 24061-9632	1	ATTN PROF KARL BERGEY PROF GEORGE EMANUEL UNIVERSITY OF OKLAHOMA DEPT OF AEROSPACE AND MECHANICAL ENGINEERING NORMAN OK 73019	1 1
ATTN PROF CHARLES SPEZIALE BOSTON UNIVERSITY DEPT OF AEROSPACE AND MECHANICAL ENGINEERING 110 CUMMINGTON STREET BOXTON MA 02215	1	DEFENSE TECHNICAL INFORMATION CTR 8725 JOHN J KINGMAN RD SUITE 0944 FT BELVOIR VA 22060-6218	2
ATTN PRO CHARLES VAN ATTA UNIVERSITY OF CALIFORNIA SAN DIEGO AMES/CODE 0411 9500 GILMAN DRIVE LAJOLLA CA 92093-0075	1	ATTN E29L (TECHNICAL LIBRARY) COMMANDING OFFICER CSSDD NSWC 6703 W HIGHWAY 98 PANAMA CITY FL 32407-7001	1
ATTN PROF JOHN FOSS MICHIGAN STATE UNIVERSITY DEPT OF MECHANICAL ENGINEERING A-118 RESEARCH COMPLEX-ENGR EAST LANSING MI 48824	1	THE CNA CORPORATION P O BOX 16268 ALEXANDRIA VA 22302-0268	1
ATTN PROF JOHN SULLIVAN PURDUE UNIVERSITY SCHOOL OF AERONAUTICS AND ASTRONAUTICS 1282 GRISSOM HALL WEST LAFAYETTE IN 47907-5117	1	ATTN GIFT AND EXCHANGE DIVISION LIBRARY OF CONGRESS WASHINGTON DC 20540	4
		<b>INTERNAL DISTRIBUTION</b>	
		B44	1
		D	1
		E231	3
		E282 (SWANSBURG))	1
		K	1
		K24 (KAMMEYER)	10
		L	1